THE OHIO STATE UNIVERSITY

Bistatic Image Processing for a 32″ × 19″ Model Aircraft using Scattered Fields Obtained in the OSU-ESL Compact Range

T-H. Lee and W.D. Burnside

The Ohio State University

ElectroScience Laboratory

Department of Electrical Engineering
Columbus, Ohio 43212

Technical Report 722780-3
Grant No. NAG 2-542
February 1992

University Affairs Branch
National Aeronautics and Space Administration
Ames Research Center 241-25
Moffett Field, CA 94035

NOTICES

When Government drawings, specifications, or other data are used for any purpose other than in connection with a definitely related Government procurement operation, the United States Government thereby incurs no responsibility nor any obligation whatsoever, and the fact that the Government may have formulated, furnished, or in any way supplied the said drawings, specifications, or other data, is not to be regarded by implication or otherwise as in any manner licensing the holder or any other person or corporation, or conveying any rights or permission to manufacture, use, or sell any patented invention that may in any way be related thereto.

50272-101

REPORT DOCUMENTATION PAGE	1. REPORT NO.	2.	3. Recipient's Accession No.

4. Title and Subtitle
Bistatic Image Processing for a 32″ × 19″ Model Aircraft using Scattered Fields Obtained in the OSU-ESL Compact Range

5. Report Date
February 1992

6.

7. Author(s)
T-H. Lee and W.D. Burnside

8. Performing Org. Rept. No.
722780-3

9. Performing Organization Name and Address
The Ohio State University
ElectroScience Laboratory
1320 Kinnear Road
Columbus, OH 43212

10. Project/Task/Work Unit No.

11. Contract(C) or Grant(G) No.
(C)
(G) NAG 2-542

12. Sponsoring Organization Name and Address
University Affairs Branch
NASA Ames Research Ctr. 241-25
Moffett Field, CA 94035

13. Report Type/Period Covered
Technical Report

14.

15. Supplementary Notes

16. Abstract (Limit: 200 words)

Inverse Synthetic Aperture Radar (ISAR) images for a 32″ long and 19″ wide model aircraft are documented in this report. Both backscattered and bistatic scattered fields of this model aircraft were measured in the OSU-ESL compact range to obtain these images. The scattered fields of the target were measured for frequencies from 2 to 18 GHz with a 10 MHz increment and for full 360° azimuth rotation angles with a 0.2° step. For the bistatic scattering measurement, the compact range was used as the transmitting antenna; while, a broad band AEL double-ridge horn was used as the receiving antenna. Bistatic angles of 90° and 135° were measured. Due to the size of the chamber and target, the receiving antenna was in the near-field of the target; nevertheless, the image processing algorithm was valid for this case.

17. Document Analysis a. Descriptors
BISTATIC
IMAGING
MEASUREMENT
COMPACT RANGE

b. Identifiers/Open-Ended Terms

c. COSATI Field/Group

18. Availability Statement	19. Security Class (This Report)	21. No. of Pages
A. Approved for public release; Distribution is unlimited.	Unclassified	130
	20. Security Class (This Page) Unclassified	22. Price

(See ANSI-Z39.18) *See Instructions on Reverse* OPTIONAL FORM 272 (4-77)
Department of Commerce

Contents

List of Figures

Chapter 1

Introduction

This report documents the Inverse Synthetic Aperture Radar (ISAR) images of a 32″ long and 19″ wide model aircraft. The scattered fields of this target were measured in OSU-ESL compact range. Due to the multi-channel measurement capability of OSU-ESL compact range, both the backscattered and bistatic scattered fields of this target were measured in the same time. The scattered fields were collected for frequencies from 2 to 18 GHz with a 10 MHz increment and for full 360° azimuth rotation angles with a 0.2° step. Figure 1.1 shows the measurement setup.

For the backscattering measurement, the compact range was used as both the transmitting and receiving antennas. For the bistatic scattering measurement, the compact range was used as the transmitting antenna; while, a broad band AEL double-ridge horn was used as the receiving antenna. Bistatic angles of 90° and 135° were measured. Due to the size of the chamber and target, the receiving antenna was clearly in the near-field of the target.

There are several algorithms which can be used to process the measured scattered fields to obtain the ISAR images. Conventional image processing method uses efficient algorithms, such as Fast Fourier Transform, to determine the target image. This approach requires that the antenna be located a large distance from the target [1] and that the target be rotated only through small angles. This method will not be valid for the near field case or the bistatic scattering case.

In order to determine the image of the target from the collected scattered fields, a more general coherent image processing approach has to be implemented [1, 2, 3]. With the knowledge of phase history of the scattering centers associated with a given illumination, the calibrated scattered fields are multiplied by a phase factor which is the complex conjugate of the phase associated with the path length from the source to the potential target scattering center and then back to the receiver. For a given potential scattering center location, the various responses are summed over the frequency band and the region of angular rotation. As a result, the summed responses at a true scattering center will be more enhanced than those which are not true scattering centers. However, the major disadvantage of this approach is the large amount of computation time required for processing.

A more general and efficient algorithm for image processing is the use of time domain data in conjunction with the angular domain data [4, 5, 6]. Since the scattered fields are normally collected as a function of frequency for a given target rotation angle, one can transform the frequency domain data of the calibrated scattered fields to time domain data via a Fast Fourier Transform. The time domain data obtained represents the location of scattering centers relative to the reference target along the axis of incident and its subsequent scattered direction. A given point on the time axis indicates the time required for a wave to travel from the source to a point in the image plane and then to the receiver. For different angles of illumination, the scattering centers appear at different down range locations relative to the reference target. By summing these time domain responses for various angles of illumination, both the down range and cross range images of the scattering centers are determined. There are several advantages of this approach. First, the computation time is much more efficient than the focussed image processing approach. Secondly, neither the transmitting nor the receiving antenna has to be in the far field of the target. In addition, a real time imaging scheme can be implemented.

The ISAR images of the model aircraft documented in this report were obtained from the time domain-angular domain approach. For diagnostic applications, it is very important to investigate the characteristics of target scattering centers within a limited angular range. Consequently, the images presented in this report were generated for angular range of 20° which is represented by $\theta_m \pm 10°$ where θ_m is the mean angle. For example, $90° \pm 10°$ means time domain data from 80° to 100° were used to generate the image. Also noted is that a Kaiser-Bessel window was used in the transform from the frequency domain to time domain, and a cosine window was used in the angular domain data in generating the ISAR images.

The backscatter images of the model aircraft are summarized in Chapter 2. The bistatic images are summarized in Chapters 3 and 4 for bistatic angles (angle between the incident and the scattered directions) of 90° and 135°, respectively. At the end of each chapter, the image generated from complete 360° angular domain data is also presented for interested readers.

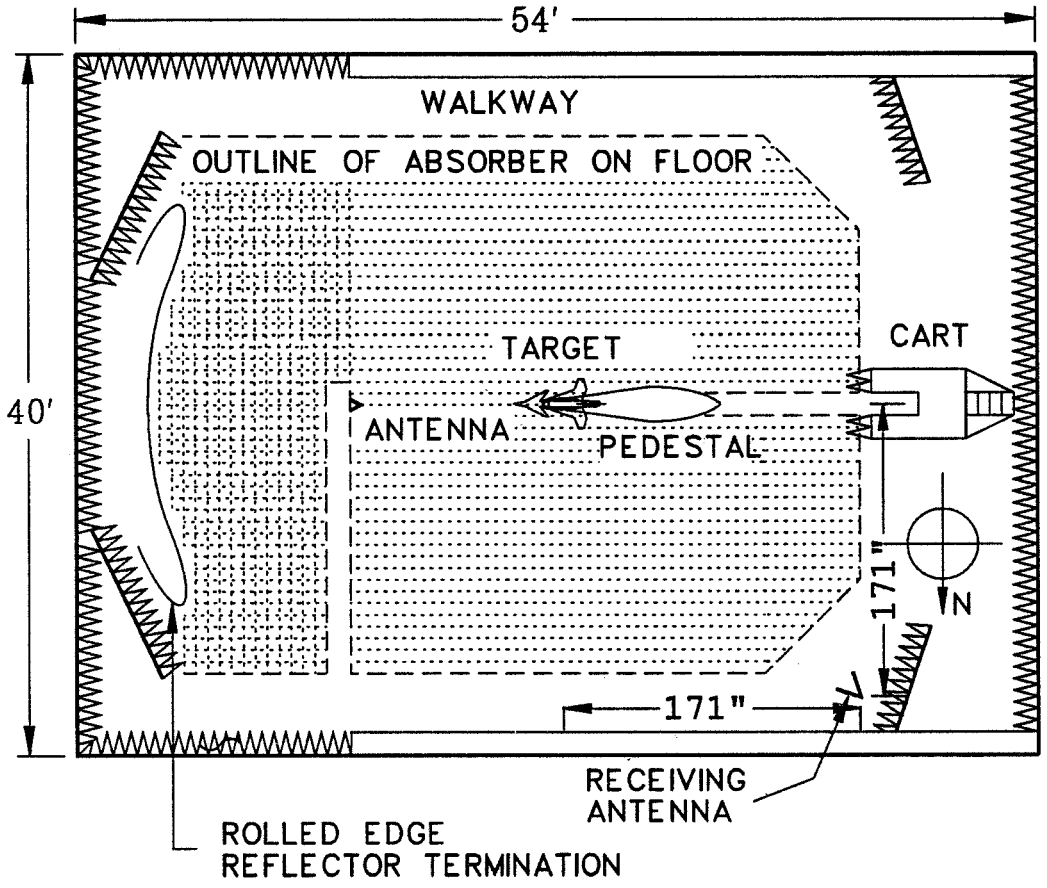

Figure 1.1: Backscattered and bistatic scattered field measurement setup in OSU-ESL compact range.

Chapter 2

Backscatter Images of the $32'' \times 19''$ Model Aircraft

This chapter summarizes the ISAR images of the model aircraft processed from the measured backscattered fields for horizontal polarization. The backscatter ISAR images for mean incident angles from 10° to 360° with a 10° step are shown in Figures 2.1 to 2.36. Note that the image for each mean incident angle was normalized with respect to its own maximum. In addition, the simplified outline of the model aircraft is also shown in these images so that one can identify the scattering centers. The complete 360° image is shown in Figure 2.37.

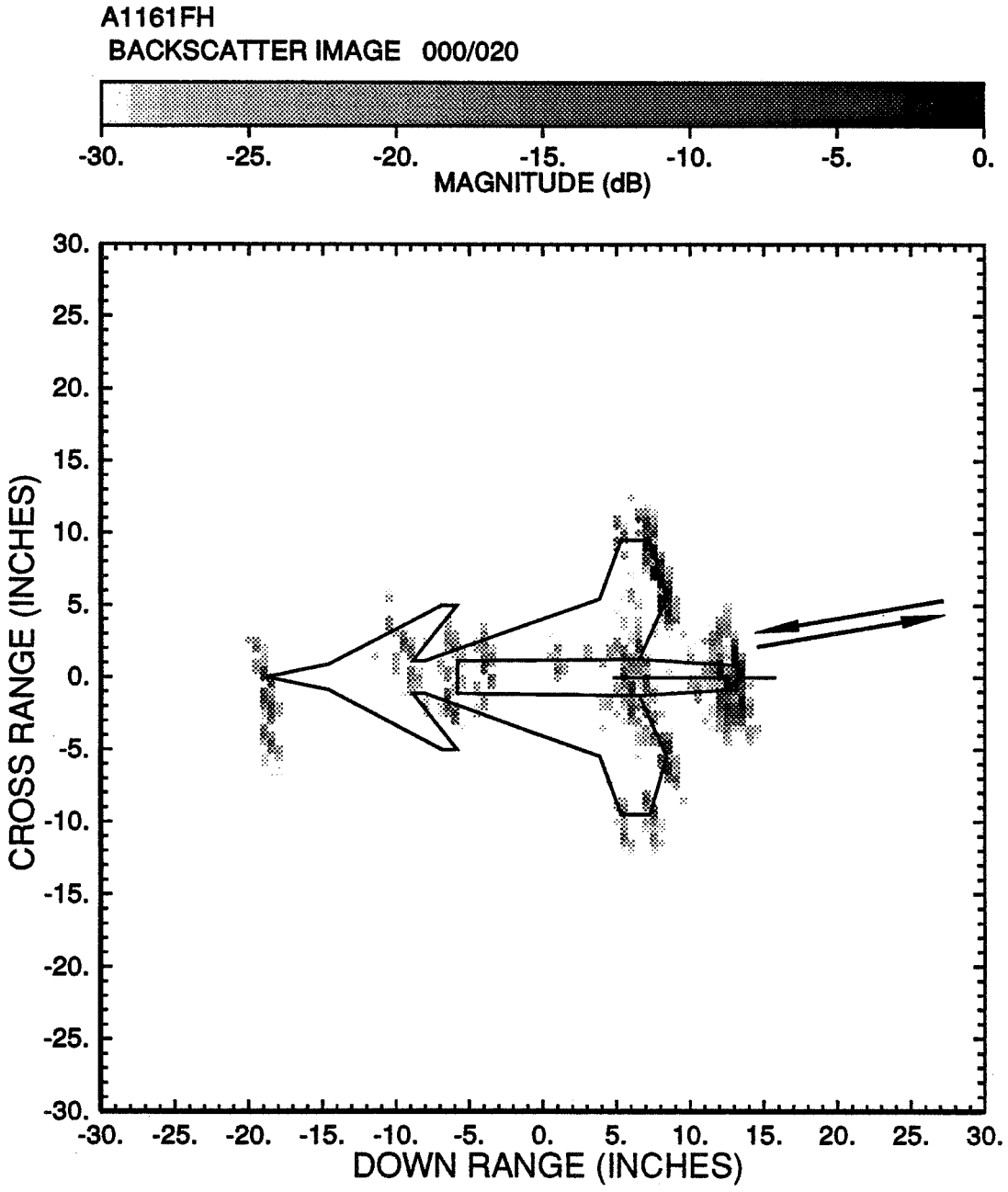

Figure 2.1: Backscatter ISAR image of the model aircraft. ($\theta = 10° \pm 10°$).

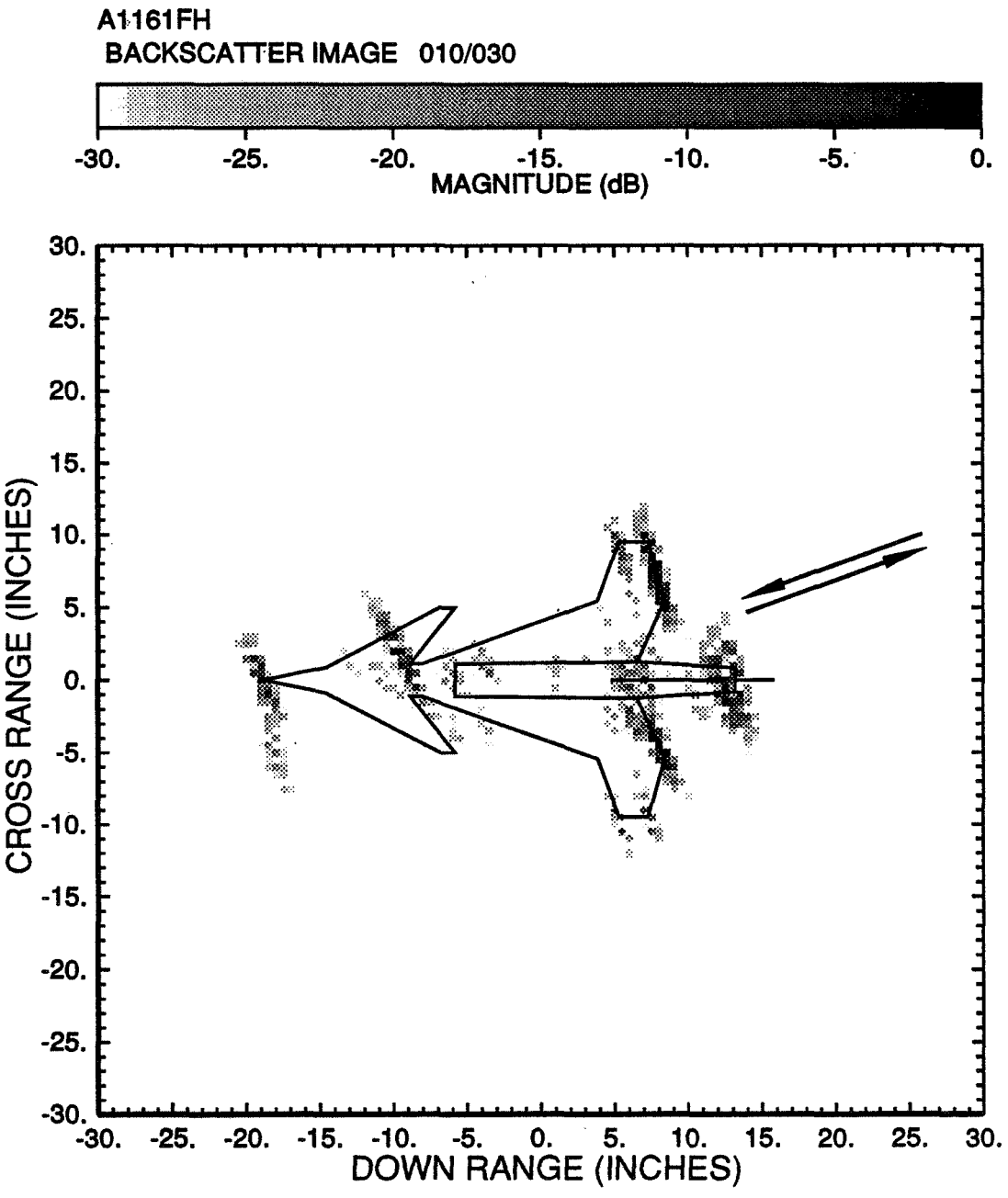

Figure 2.2: Backscatter ISAR image of the model aircraft. ($\theta = 20° \pm 10°$).

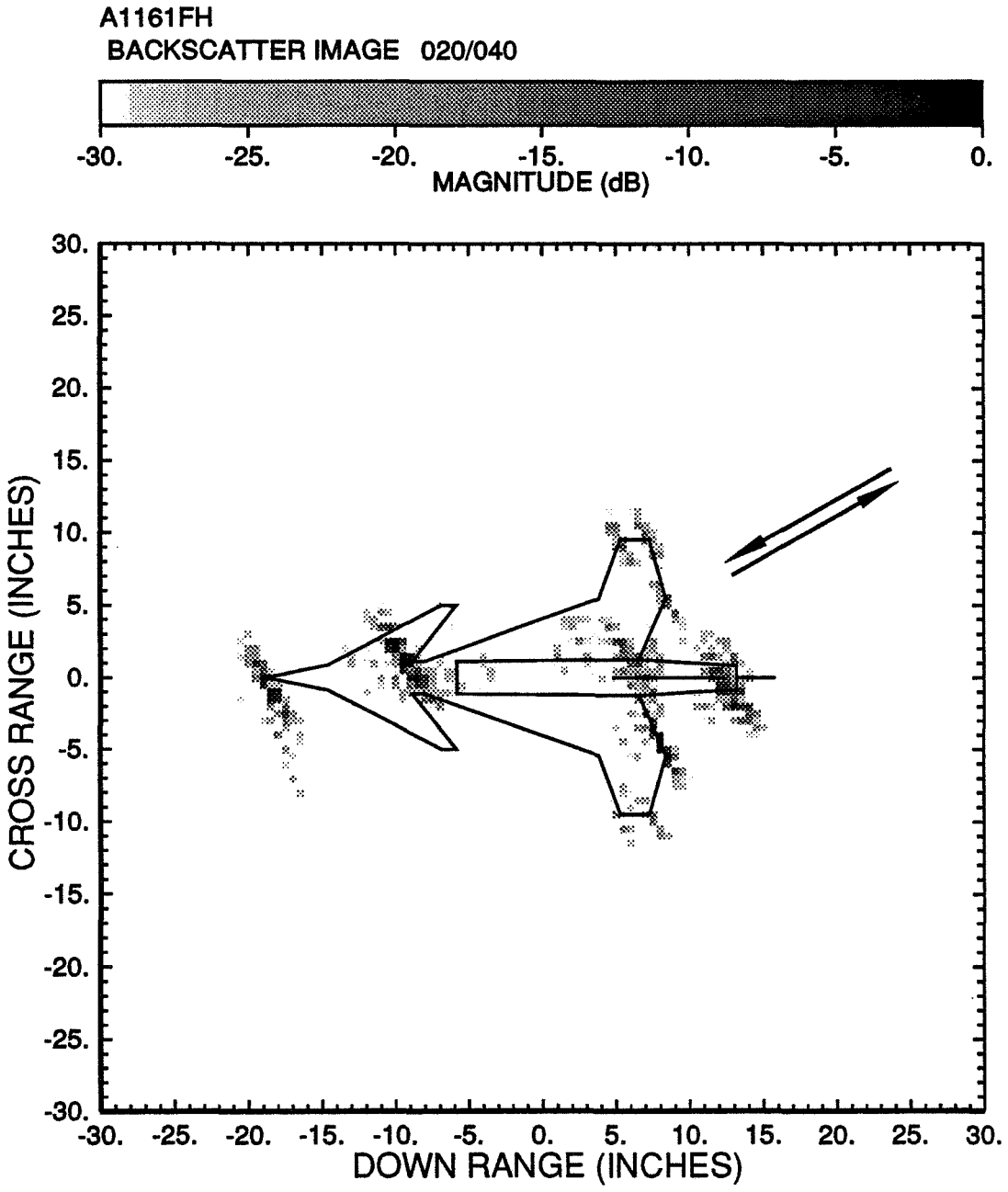

Figure 2.3: Backscatter ISAR image of the model aircraft. ($\theta = 30° \pm 10°$).

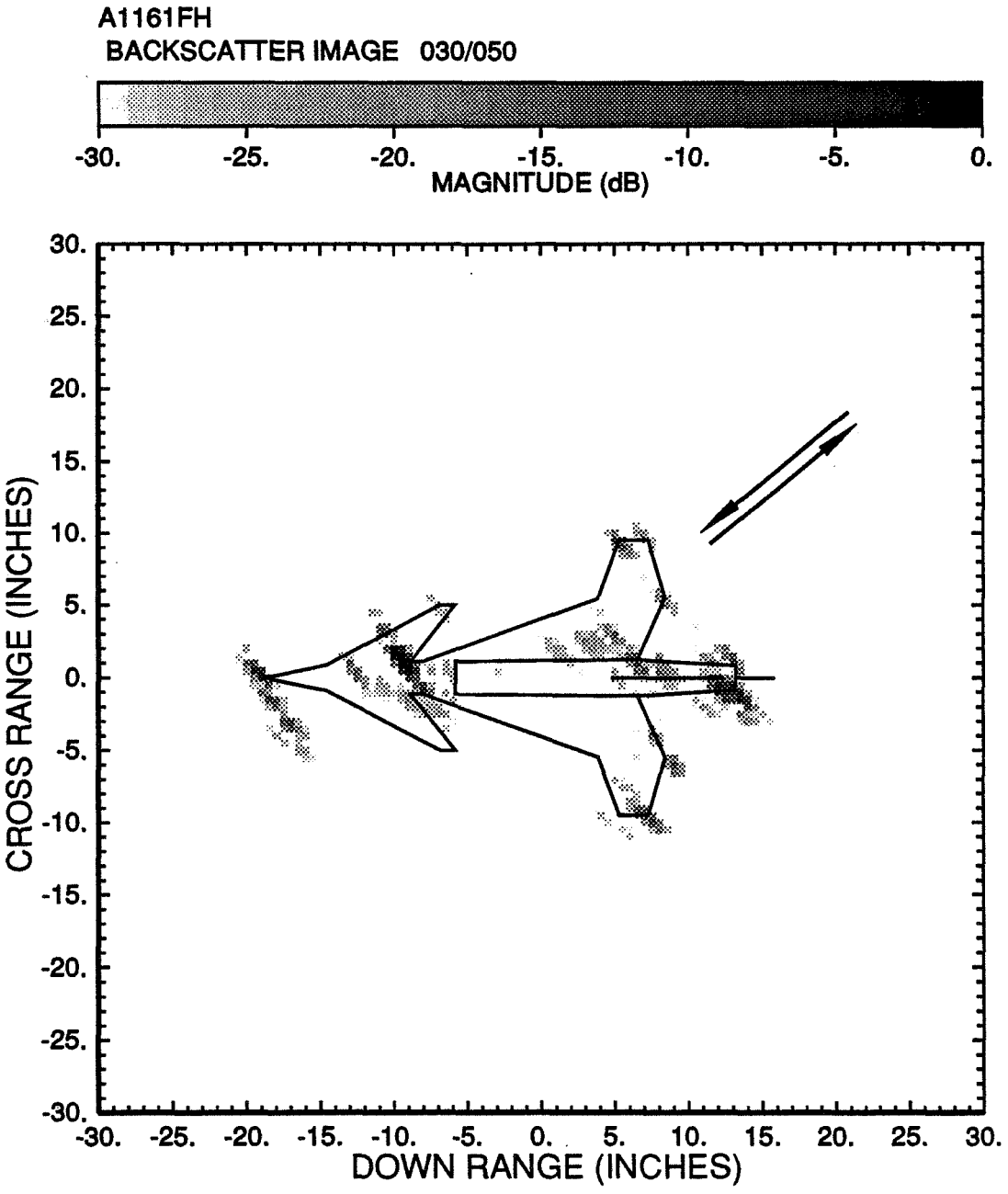

Figure 2.4: Backscatter ISAR image of the model aircraft. ($\theta = 40° \pm 10°$).

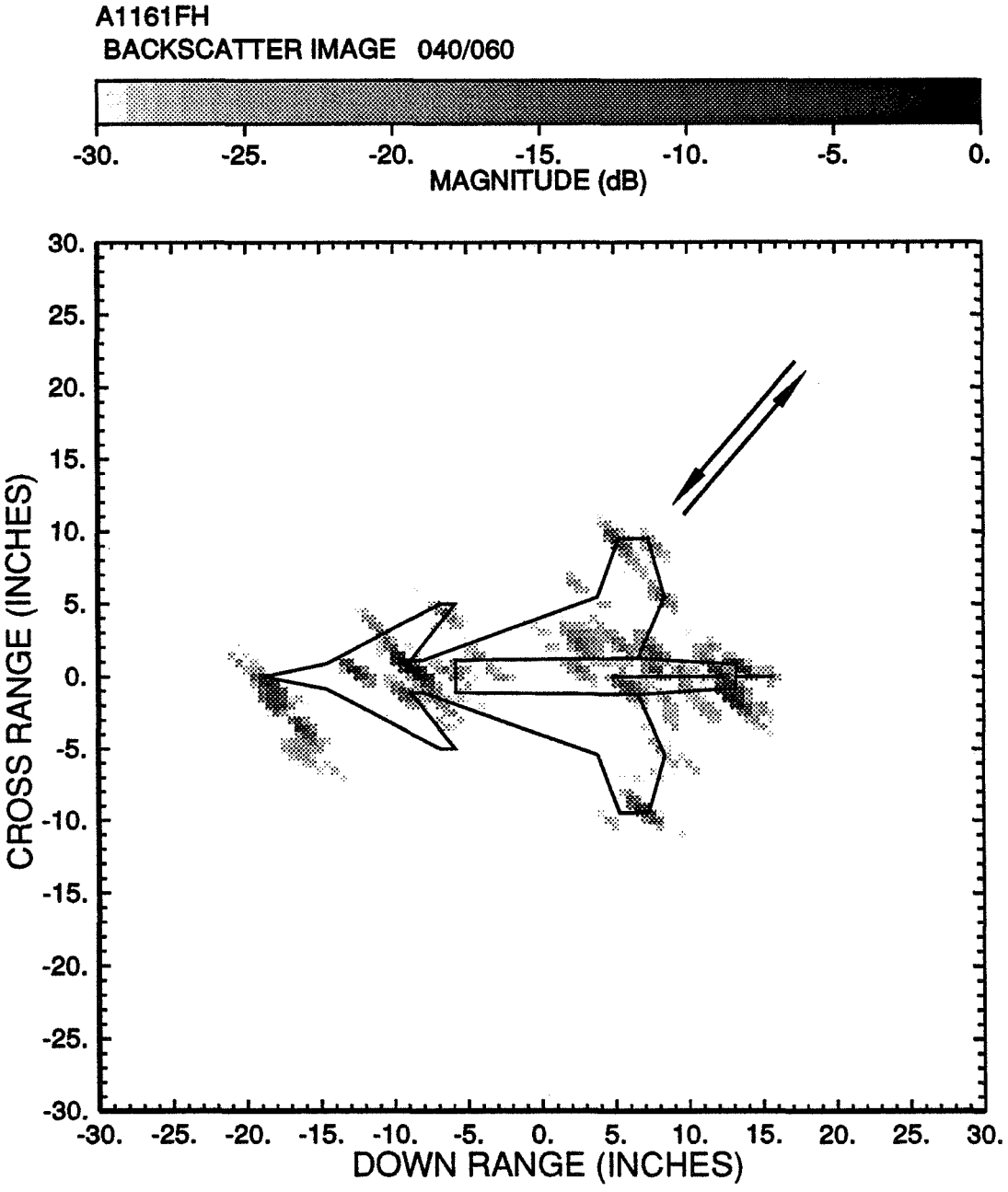

Figure 2.5: Backscatter ISAR image of the model aircraft. ($\theta = 50° \pm 10°$).

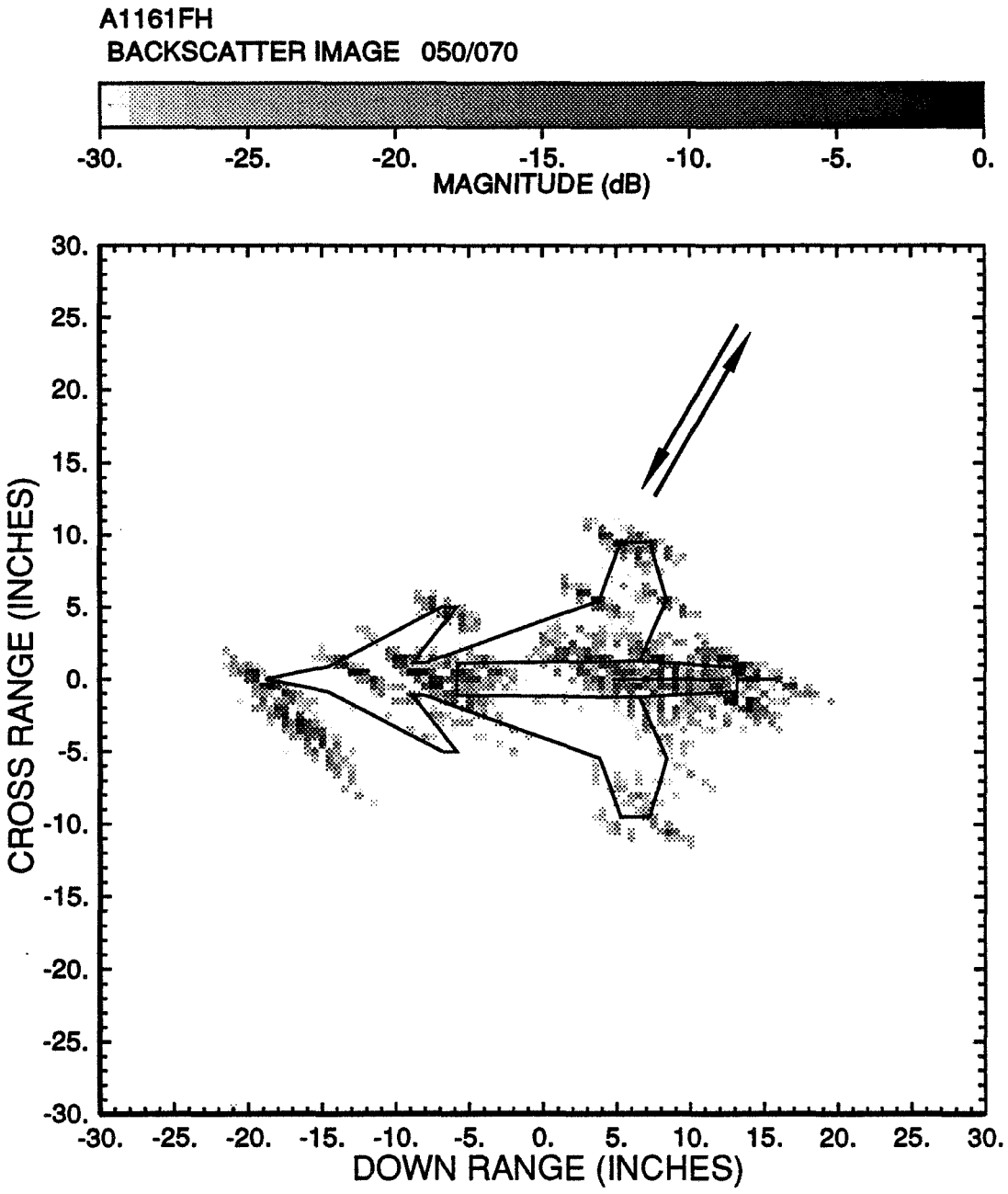

Figure 2.6: Backscatter ISAR image of the model aircraft. ($\theta = 60° \pm 10°$).

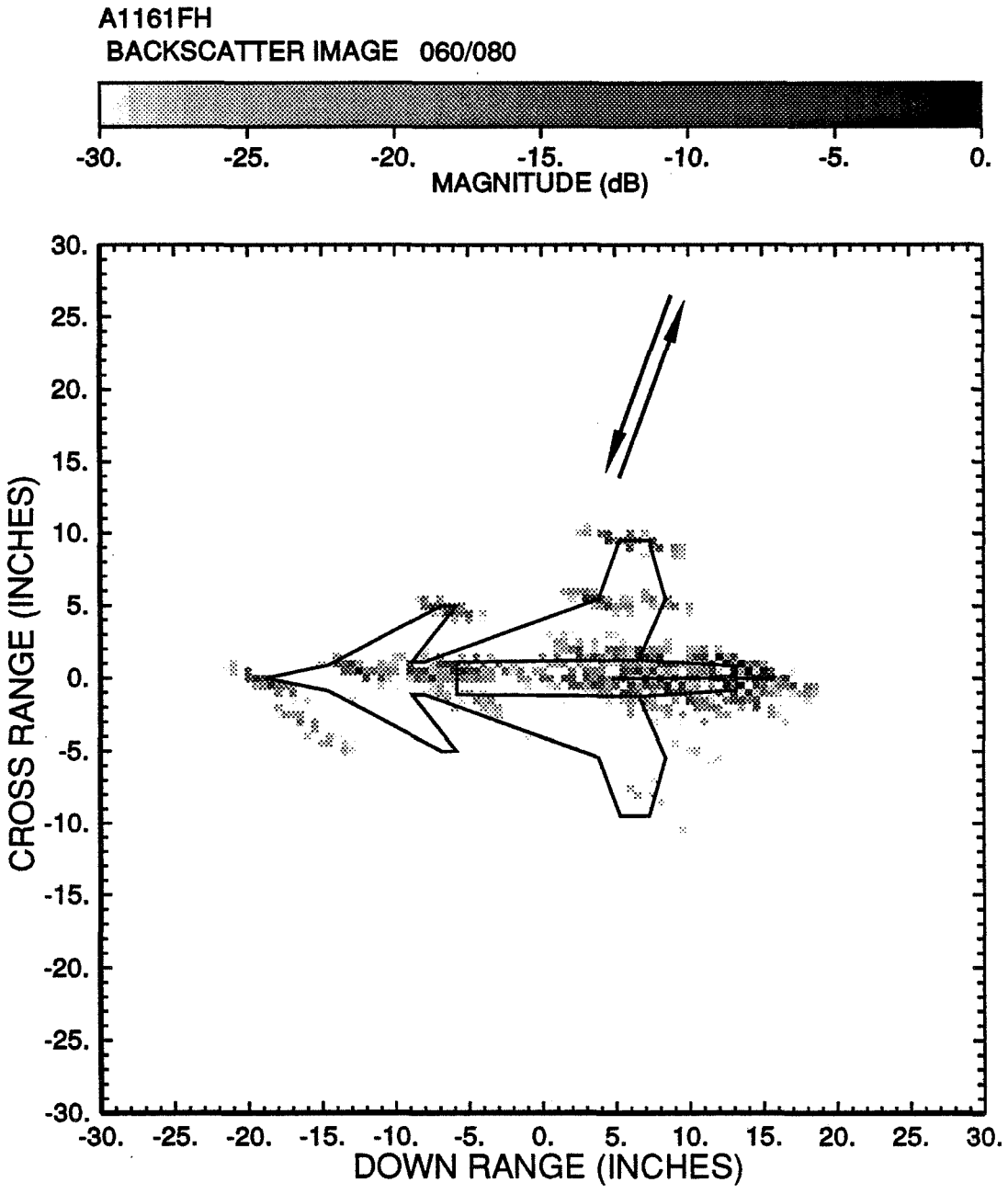

Figure 2.7: Backscatter ISAR image of the model aircraft. ($\theta = 70° \pm 10°$).

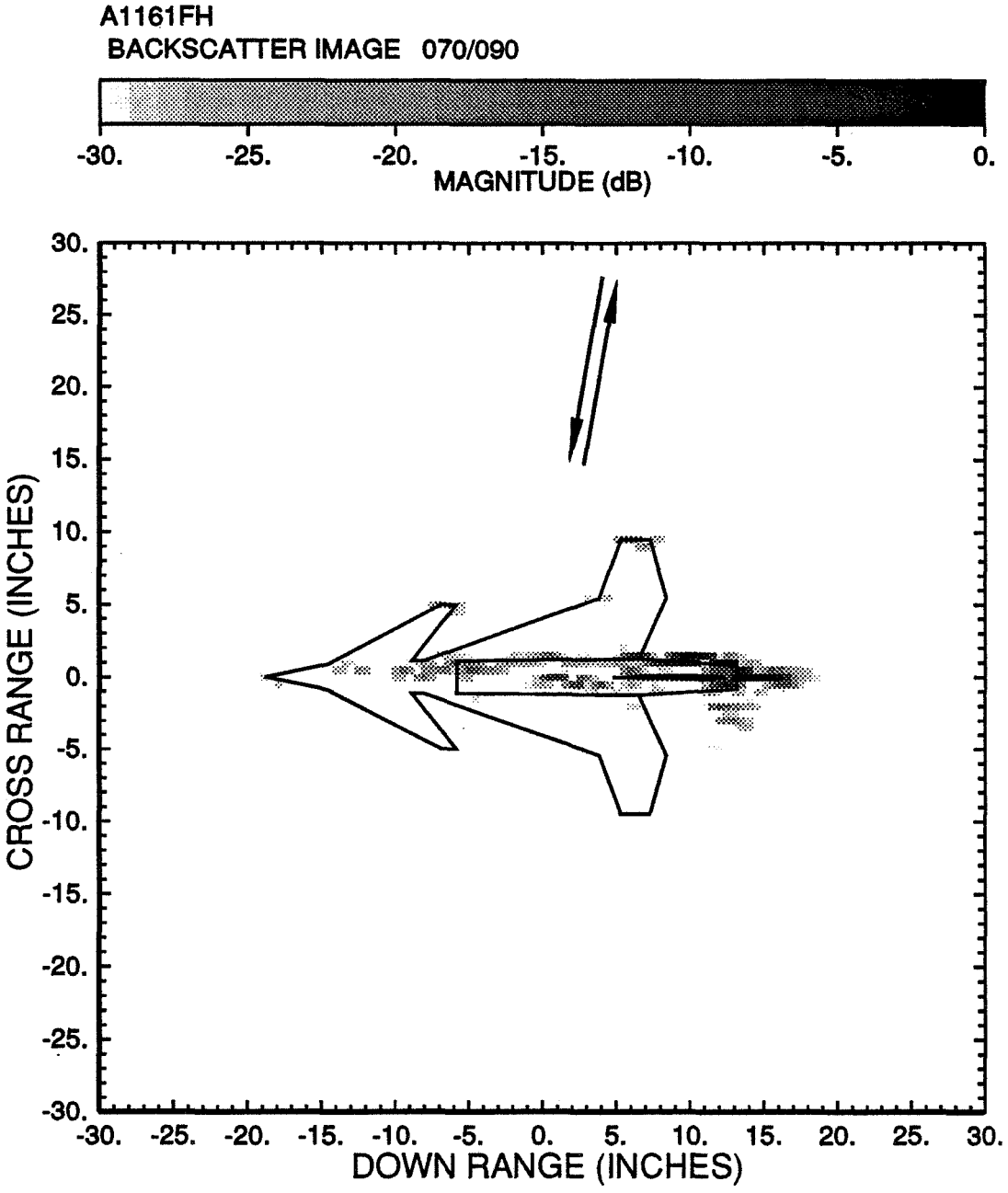

Figure 2.8: Backscatter ISAR image of the model aircraft. ($\theta = 80° \pm 10°$).

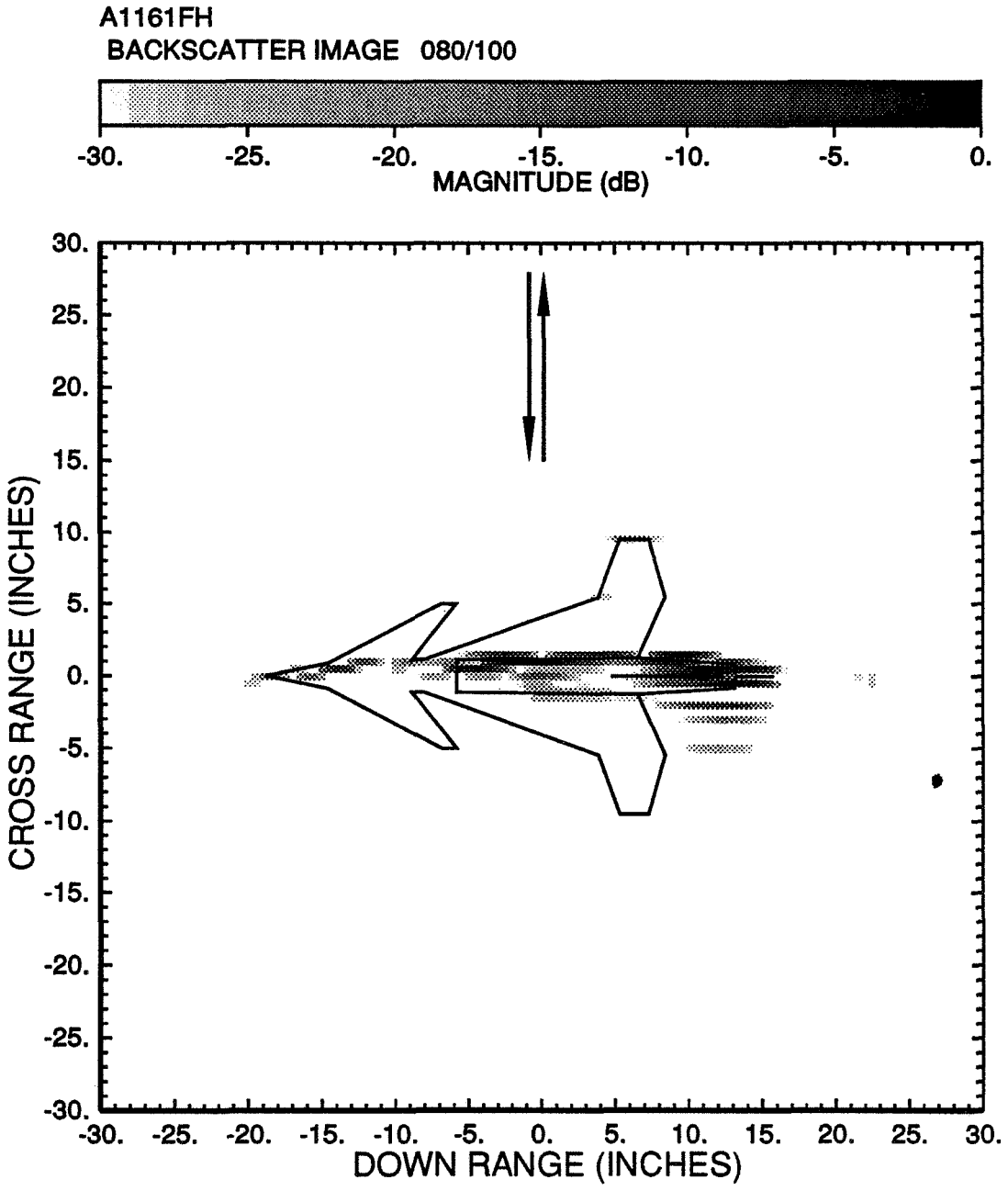

Figure 2.9: Backscatter ISAR image of the model aircraft. ($\theta = 90° \pm 10°$).

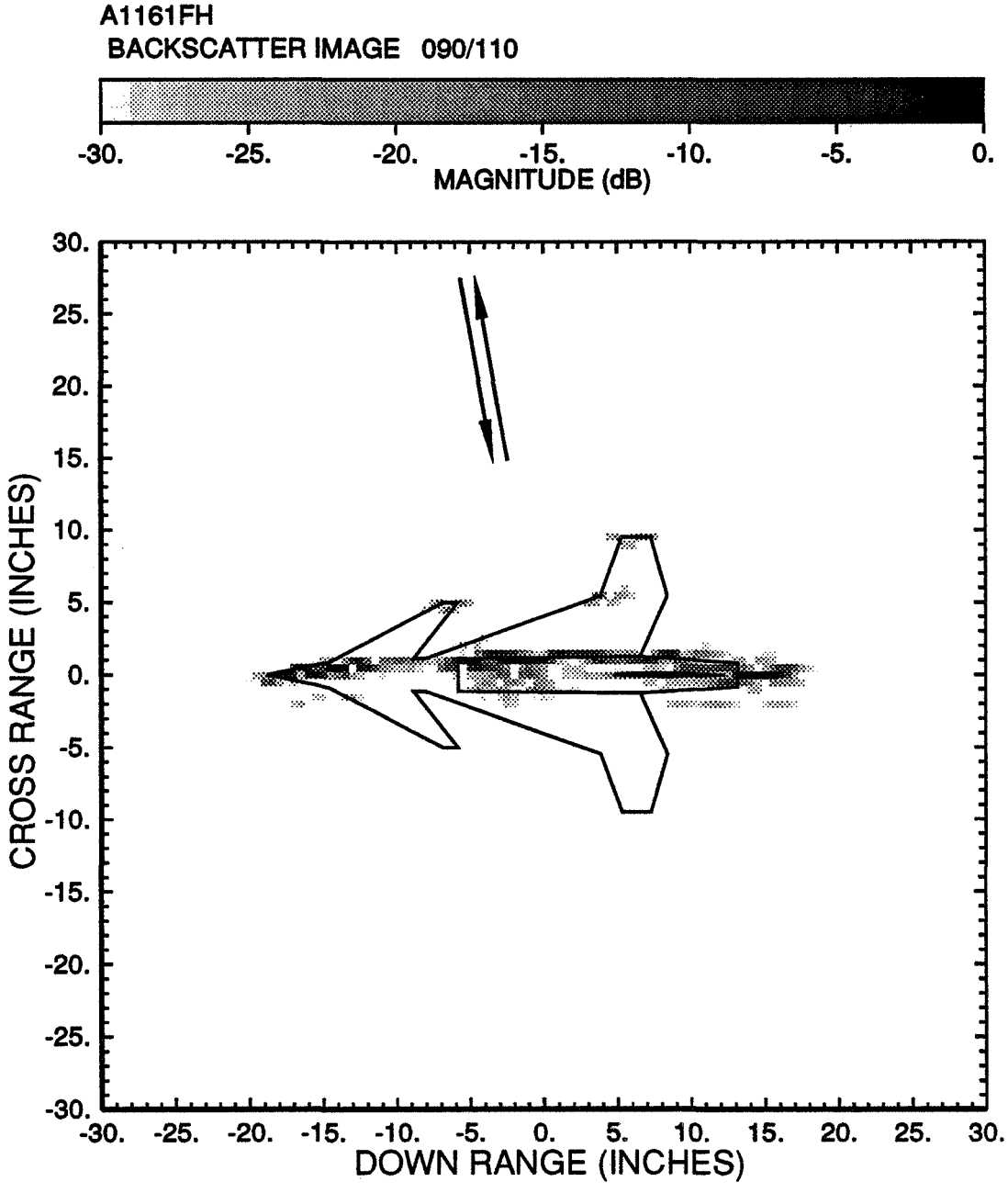

Figure 2.10: Backscatter ISAR image of the model aircraft. ($\theta = 100° \pm 10°$).

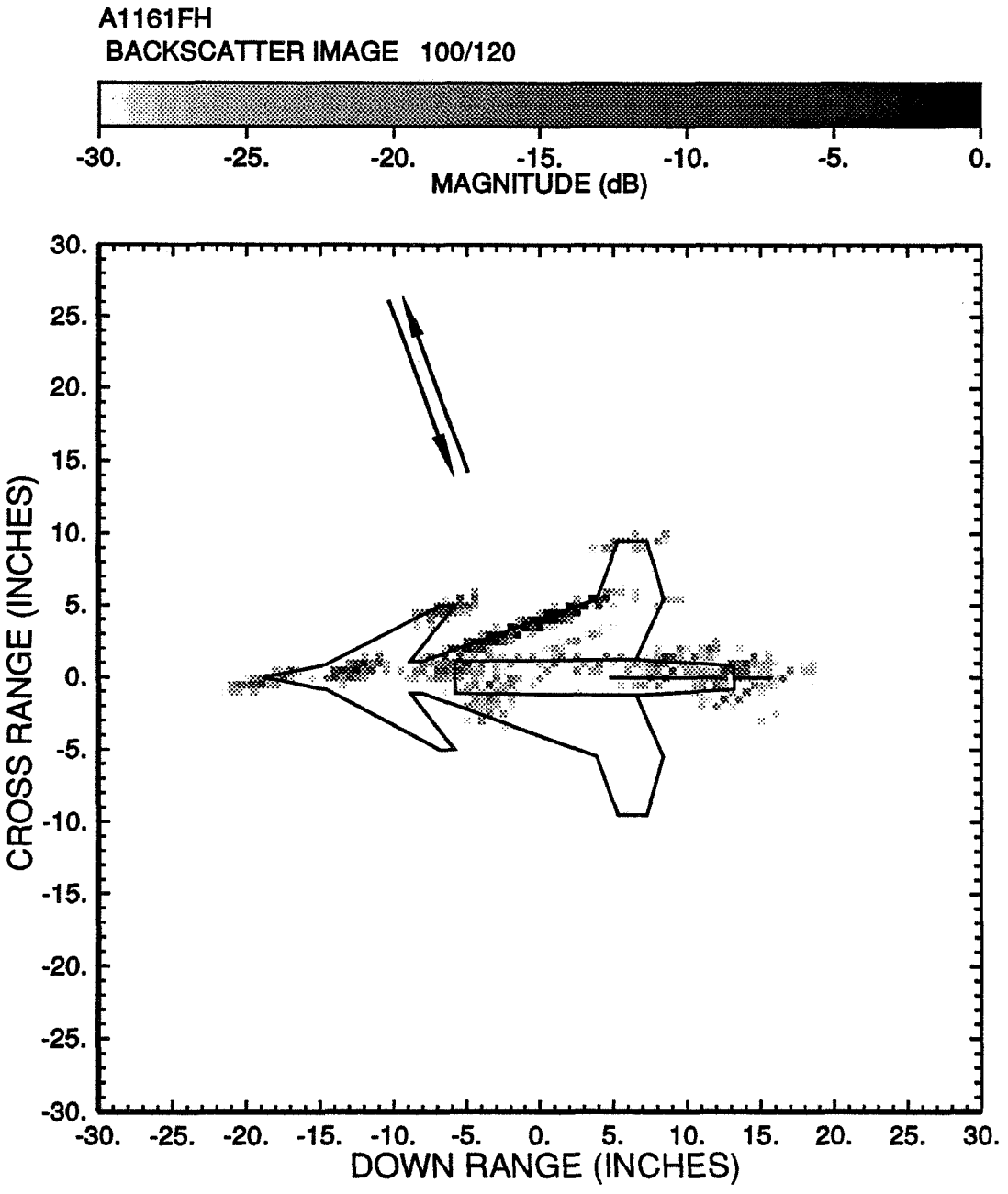

Figure 2.11: Backscatter ISAR image of the model aircraft. ($\theta = 110° \pm 10°$).

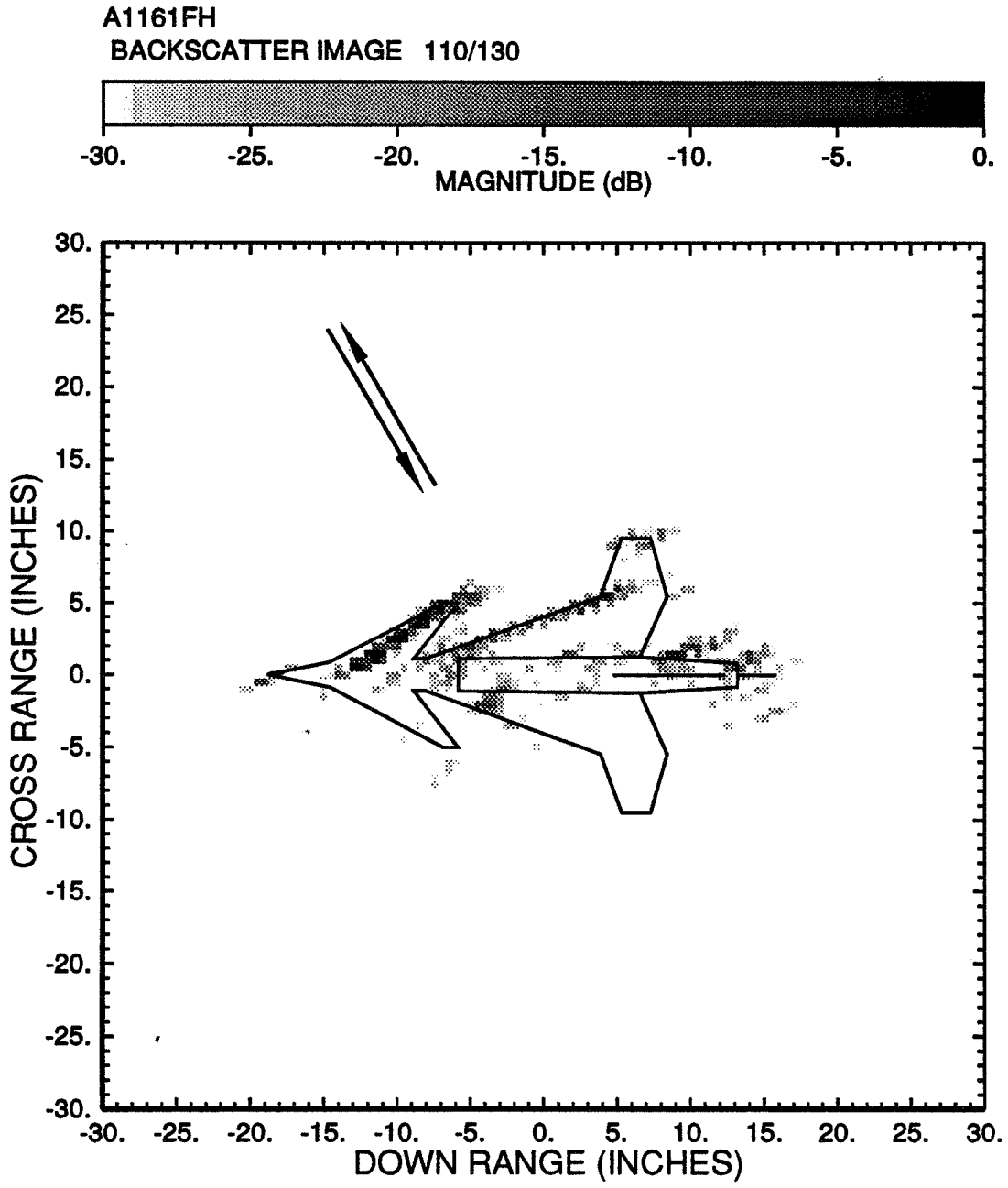

Figure 2.12: Backscatter ISAR image of the model aircraft. ($\theta = 120° \pm 10°$).

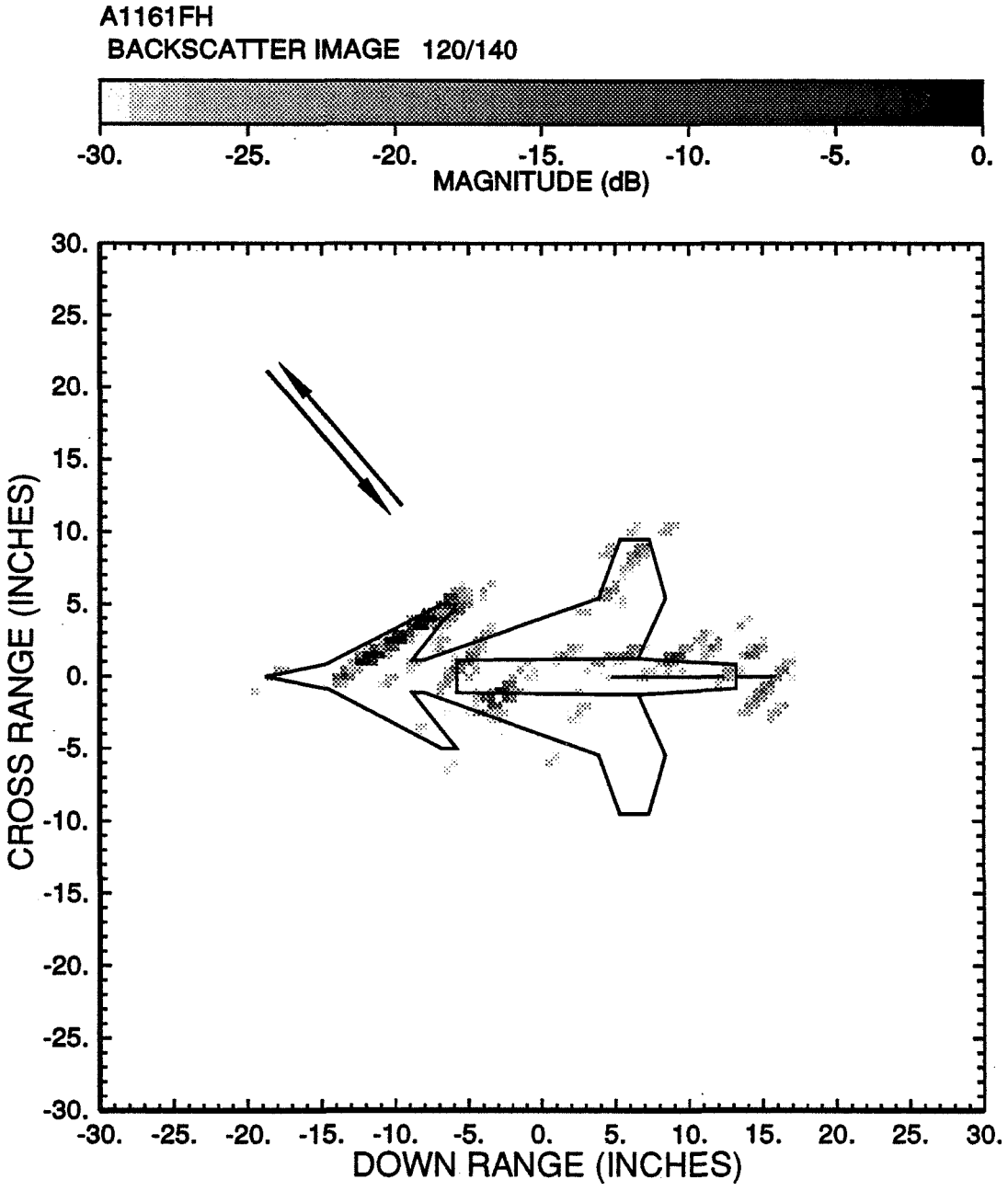

Figure 2.13: Backscatter ISAR image of the model aircraft. ($\theta = 130° \pm 10°$).

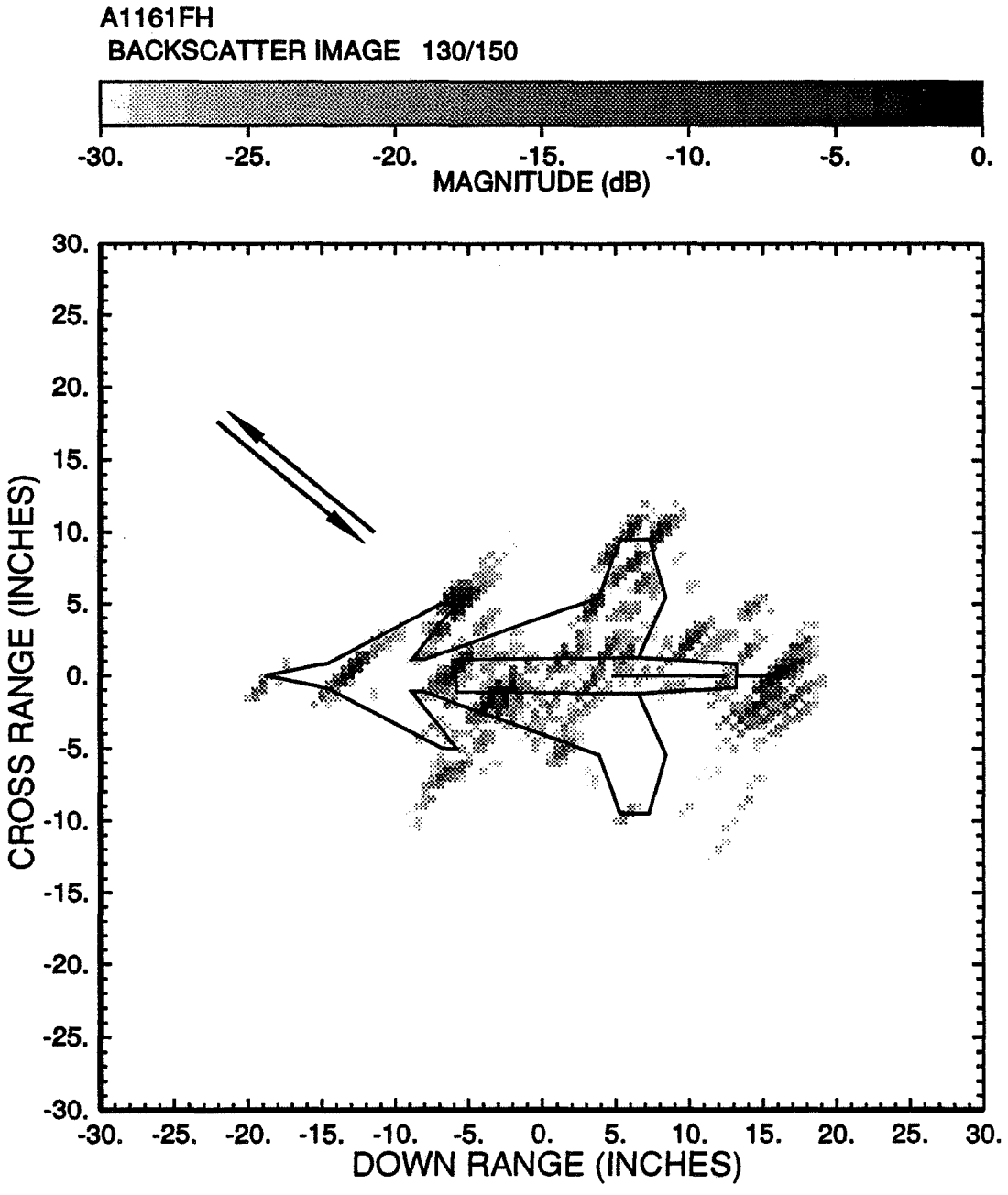

Figure 2.14: Backscatter ISAR image of the model aircraft. ($\theta = 140° \pm 10°$).

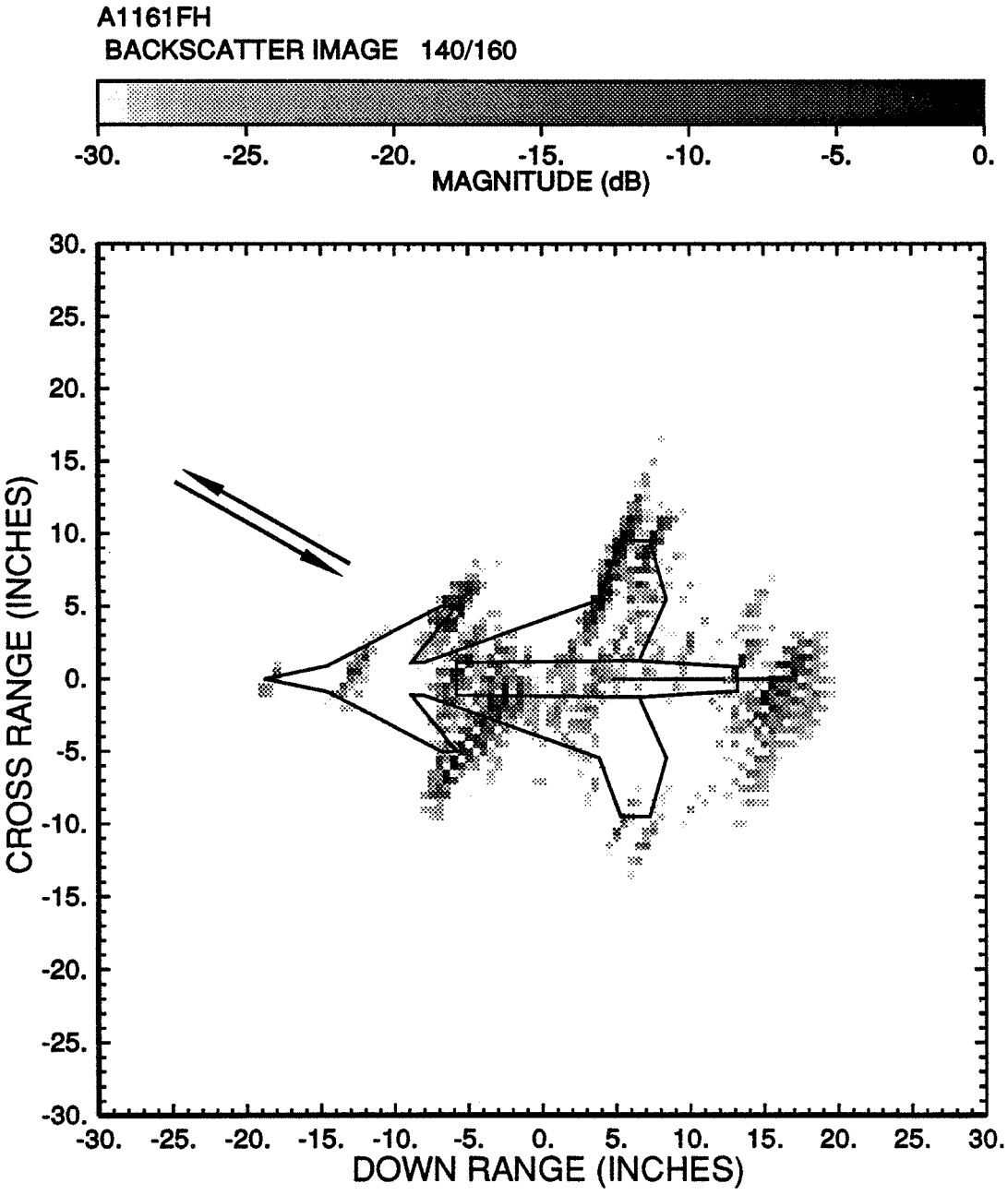

Figure 2.15: Backscatter ISAR image of the model aircraft. ($\theta = 150° \pm 10°$).

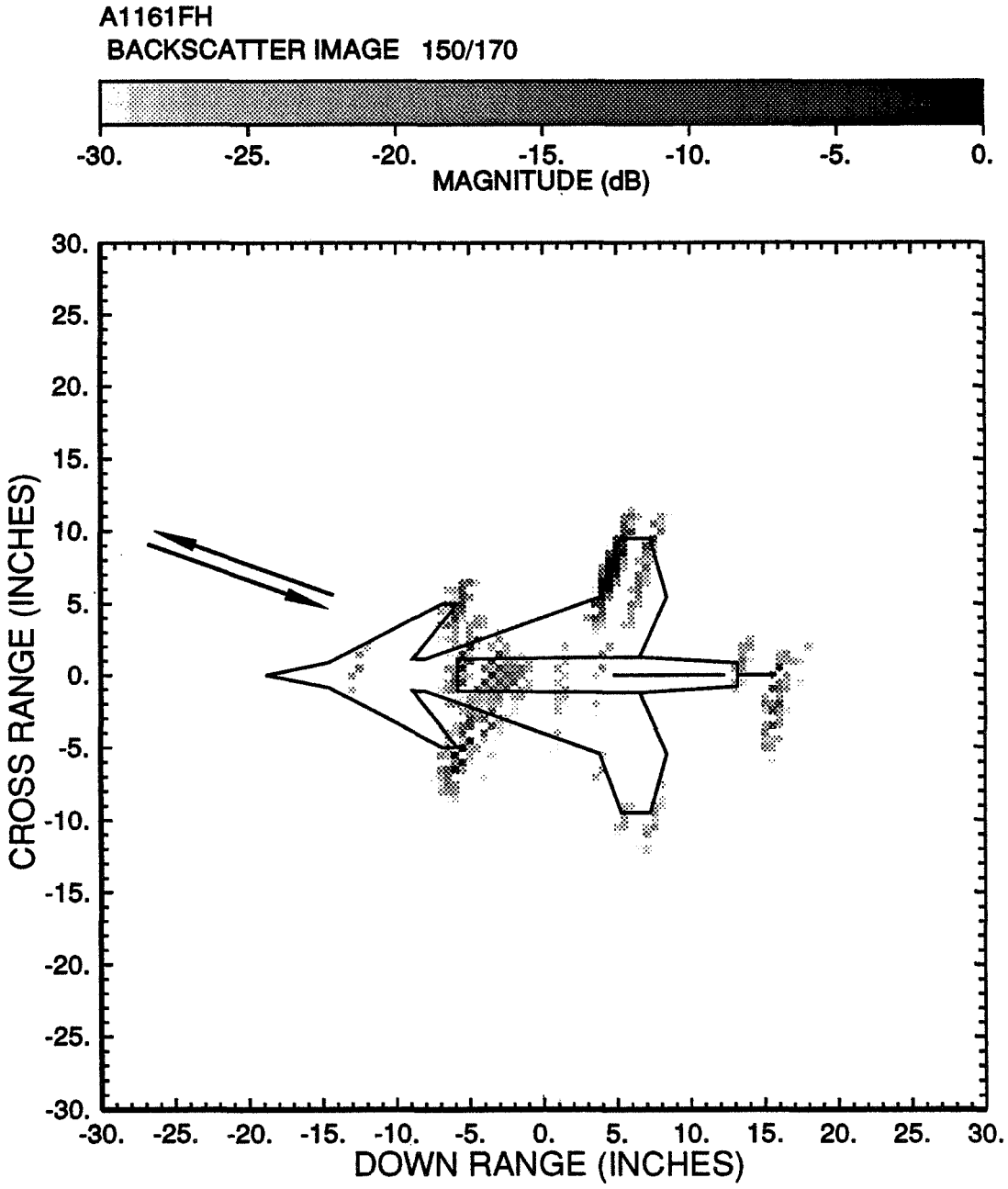

Figure 2.16: Backscatter ISAR image of the model aircraft. ($\theta = 160° \pm 10°$).

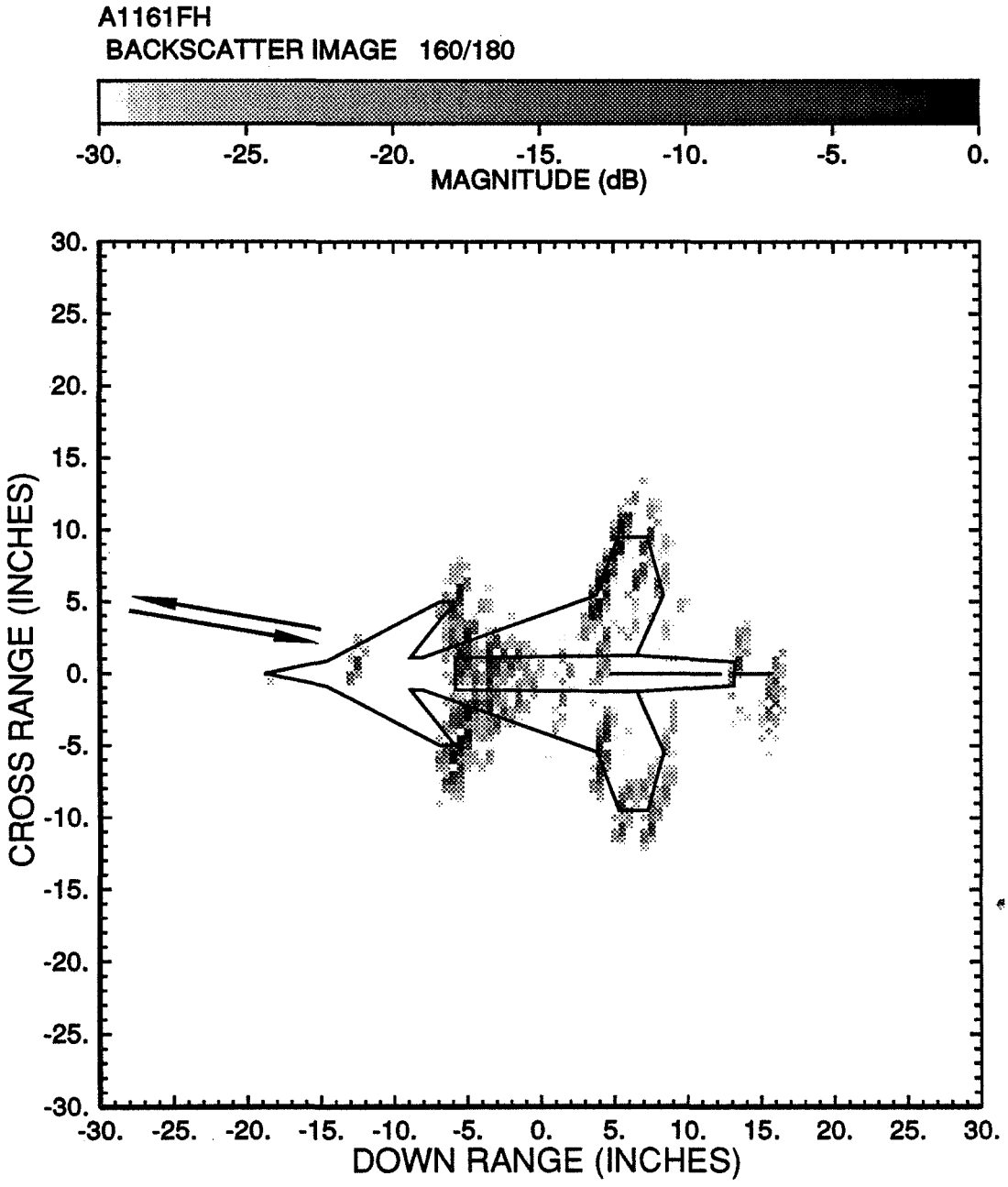

Figure 2.17: Backscatter ISAR image of the model aircraft. ($\theta = 170° \pm 10°$).

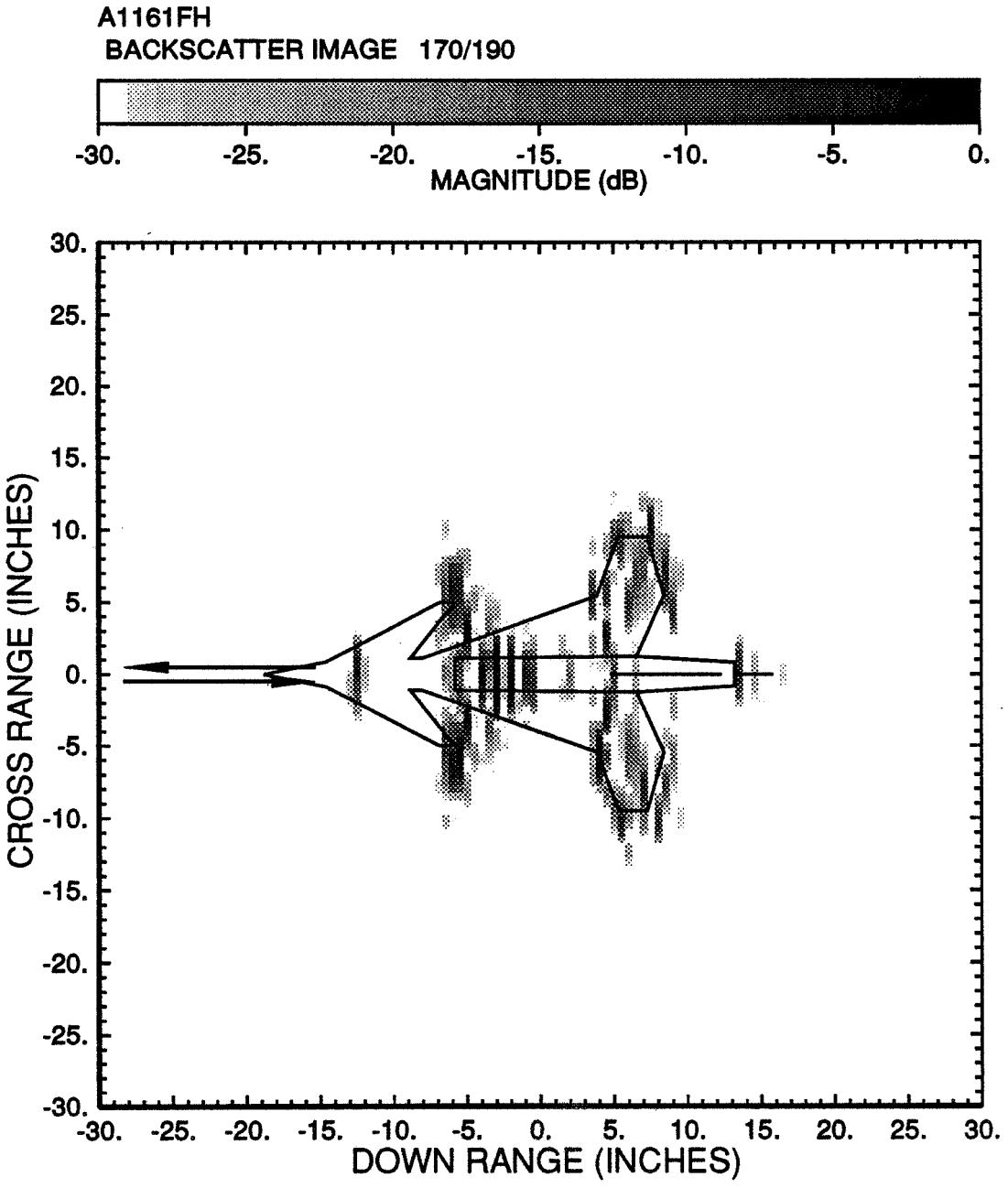

Figure 2.18: Backscatter ISAR image of the model aircraft. ($\theta = 180° \pm 10°$).

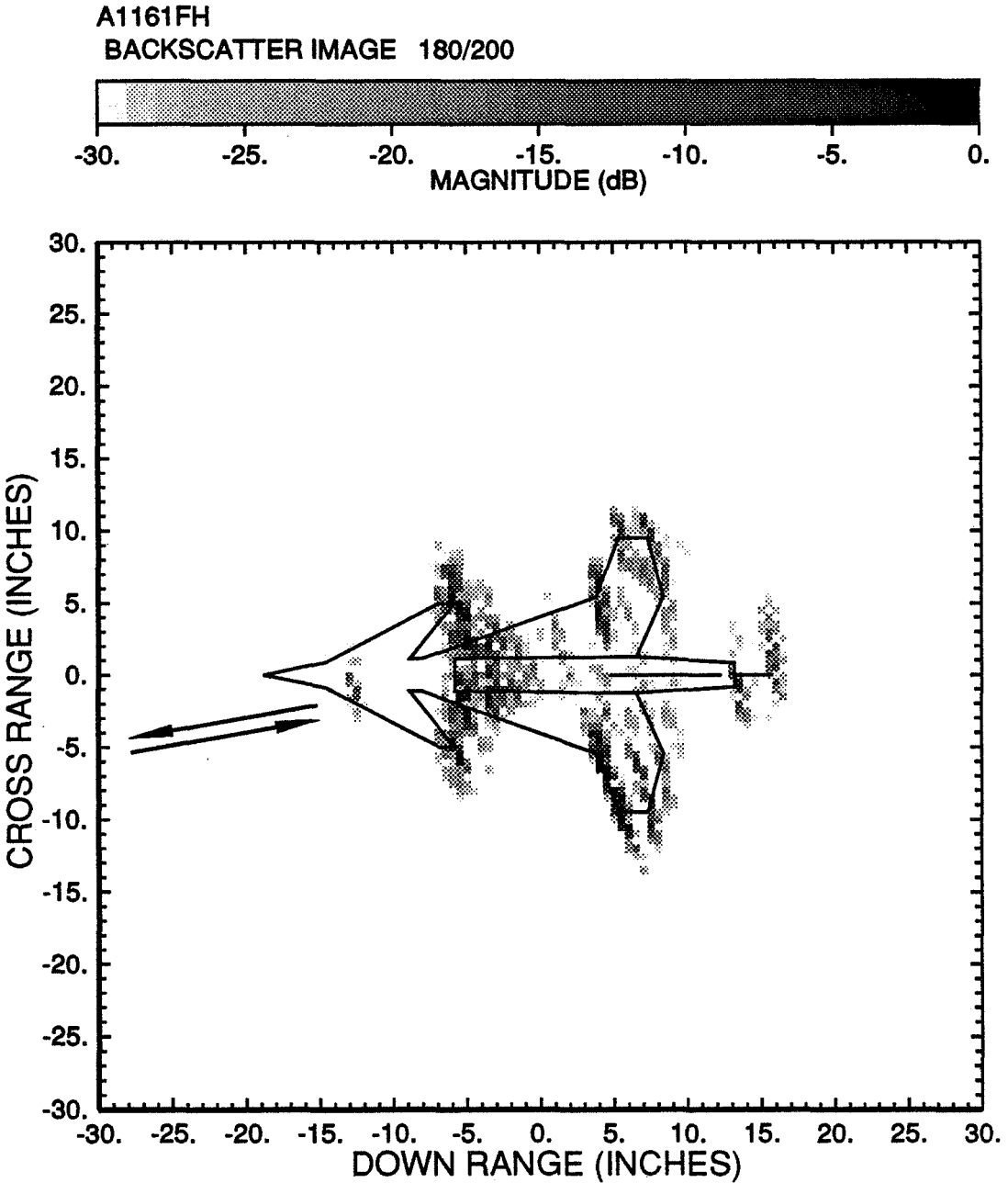

Figure 2.19: Backscatter ISAR image of the model aircraft. ($\theta = 190° \pm 10°$).

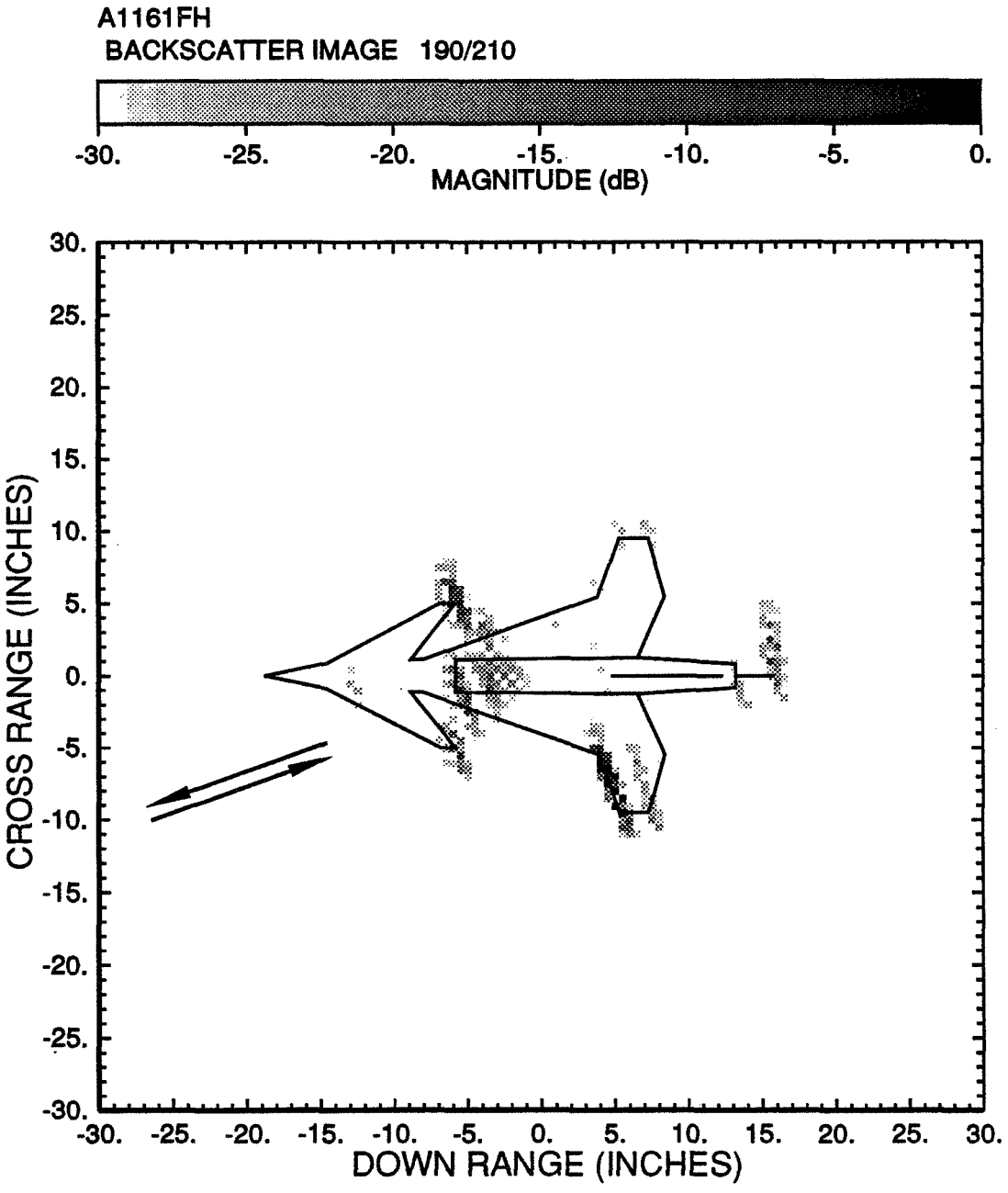

Figure 2.20: Backscatter ISAR image of the model aircraft. ($\theta = 200° \pm 10°$).

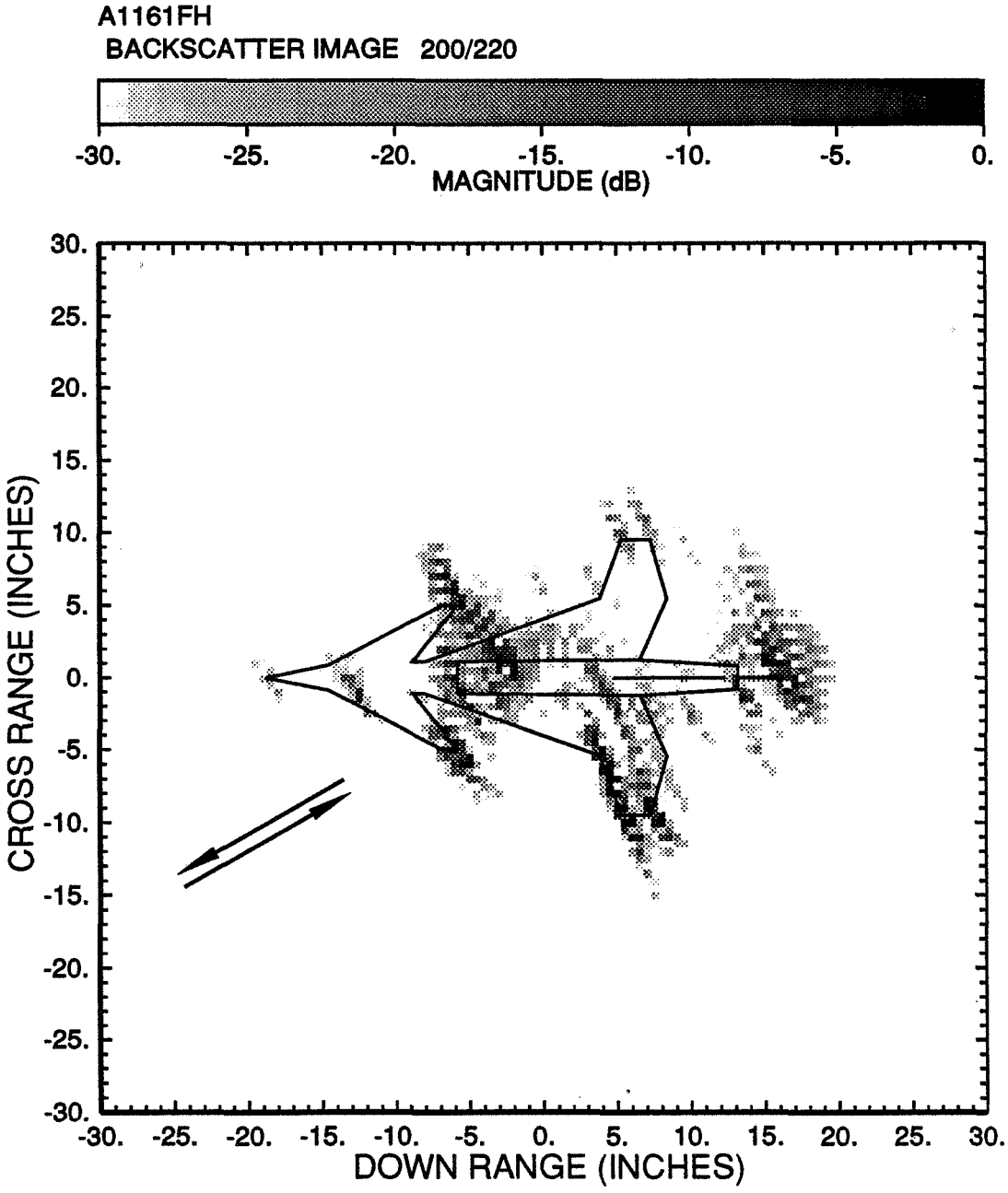

Figure 2.21: Backscatter ISAR image of the model aircraft. ($\theta = 210° \pm 10°$).

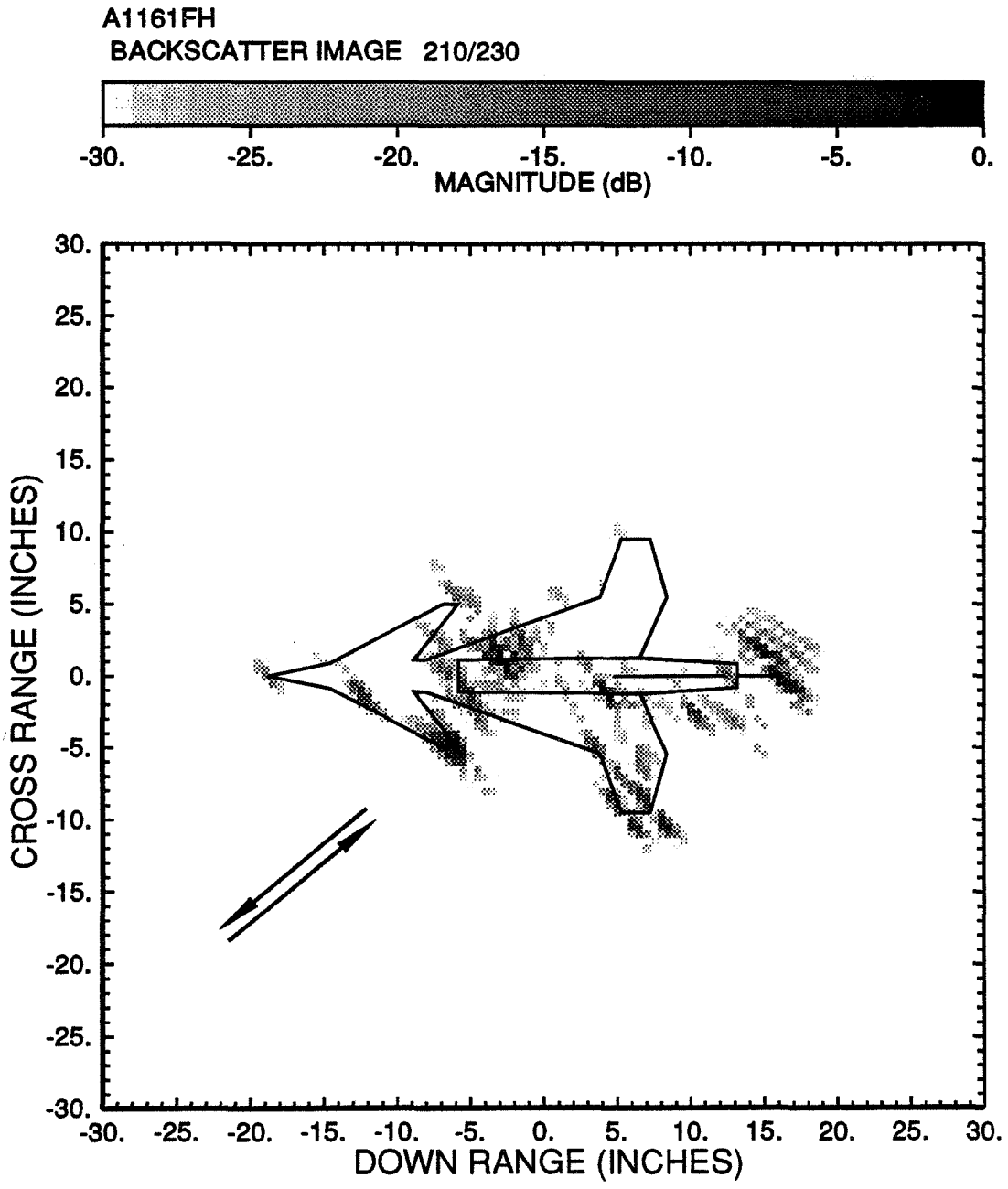

Figure 2.22: Backscatter ISAR image of the model aircraft. ($\theta = 220° \pm 10°$).

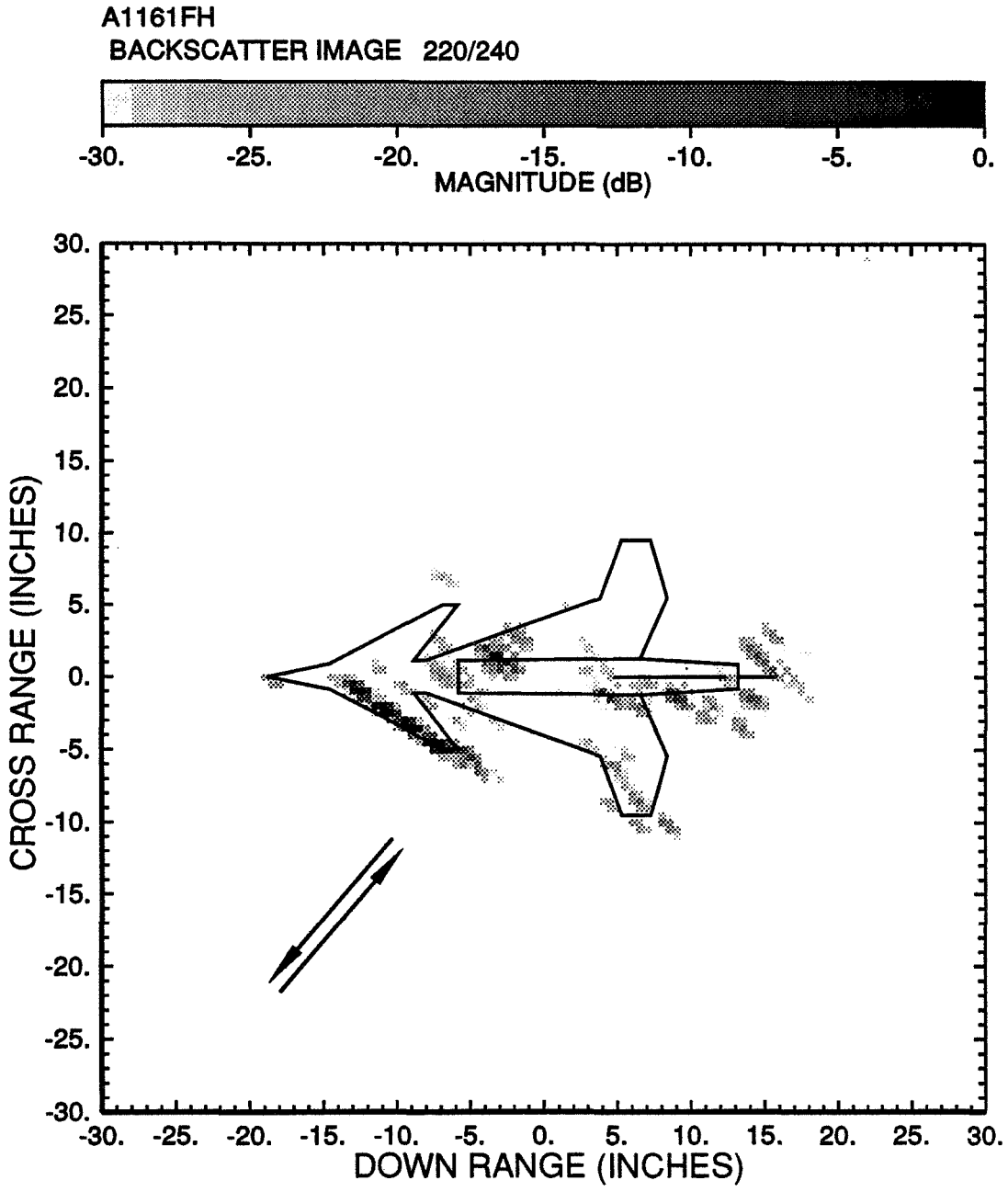

Figure 2.23: Backscatter ISAR image of the model aircraft. ($\theta = 230° \pm 10°$).

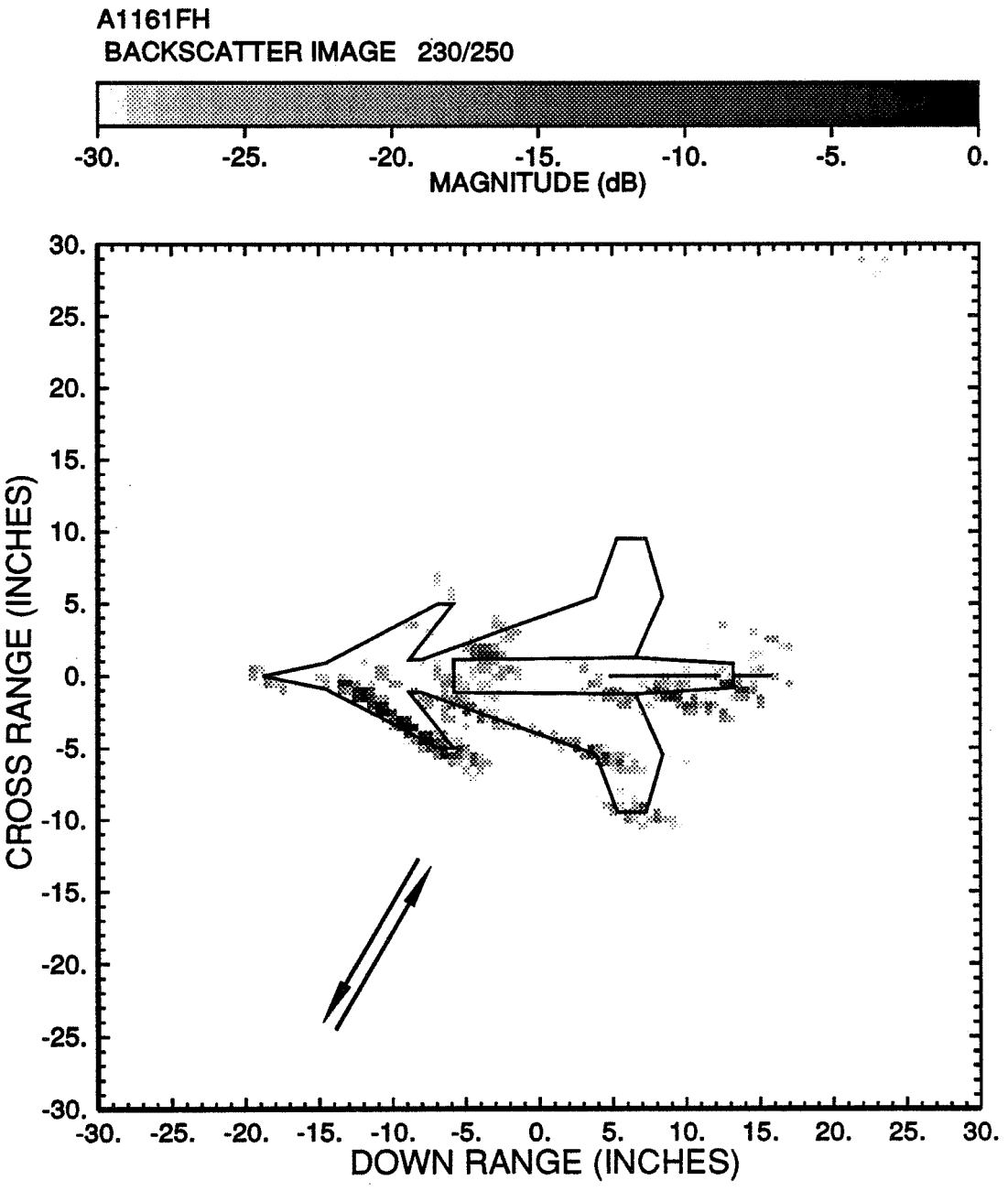

Figure 2.24: Backscatter ISAR image of the model aircraft. ($\theta = 240° \pm 10°$).

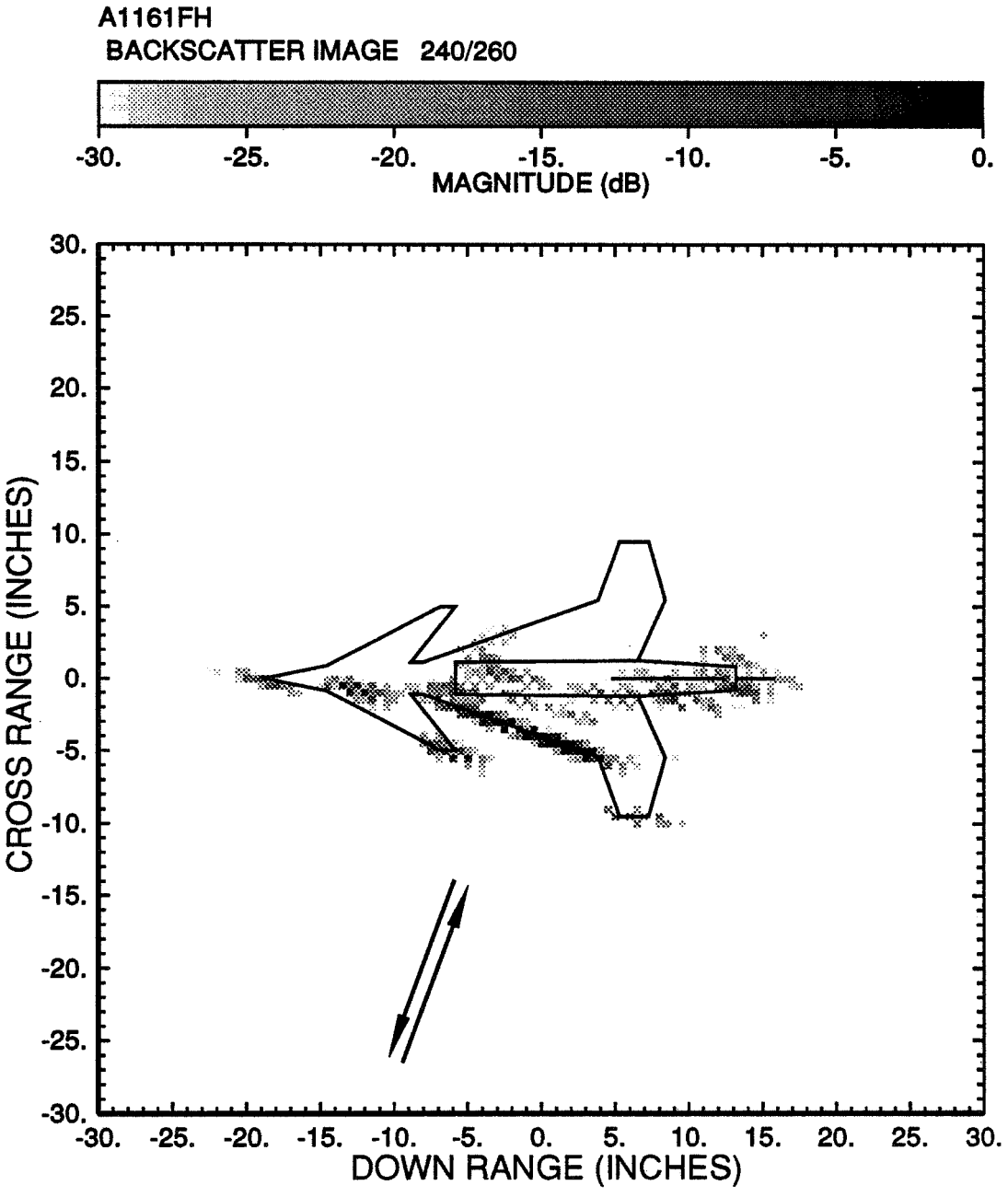

Figure 2.25: Backscatter ISAR image of the model aircraft. ($\theta = 250° \pm 10°$).

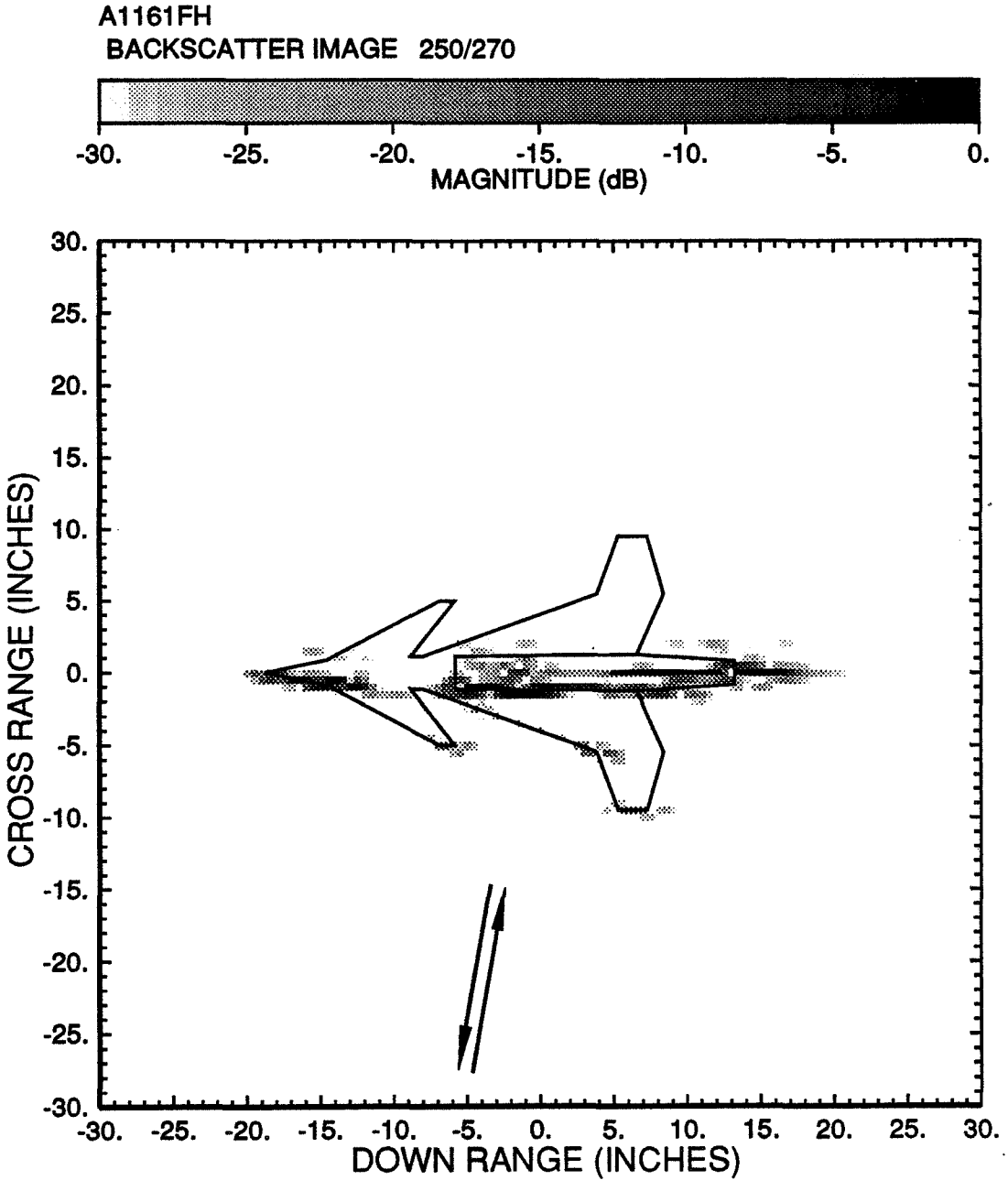

Figure 2.26: Backscatter ISAR image of the model aircraft. ($\theta = 260° \pm 10°$).

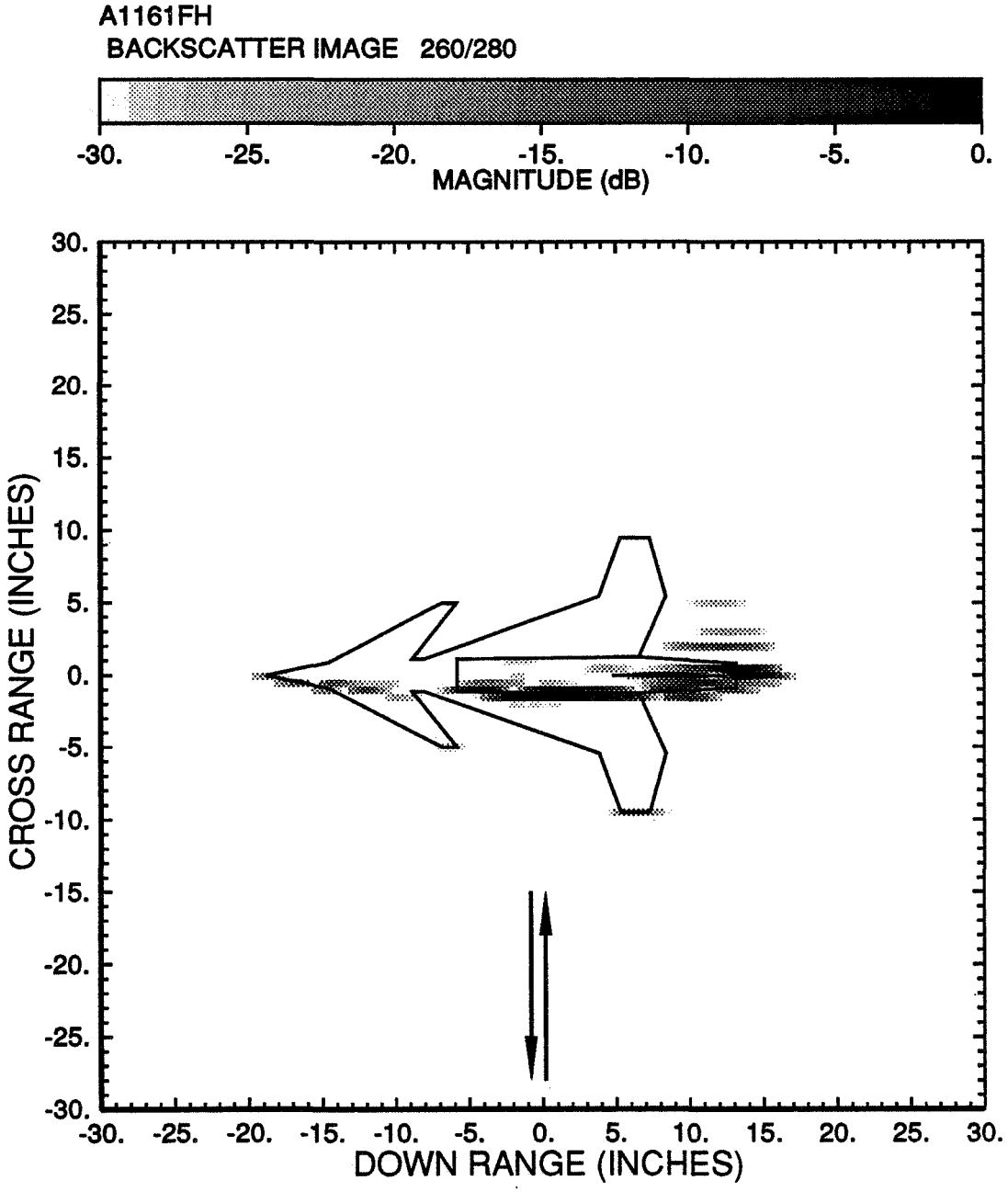

Figure 2.27: Backscatter ISAR image of the model aircraft. ($\theta = 270° \pm 10°$).

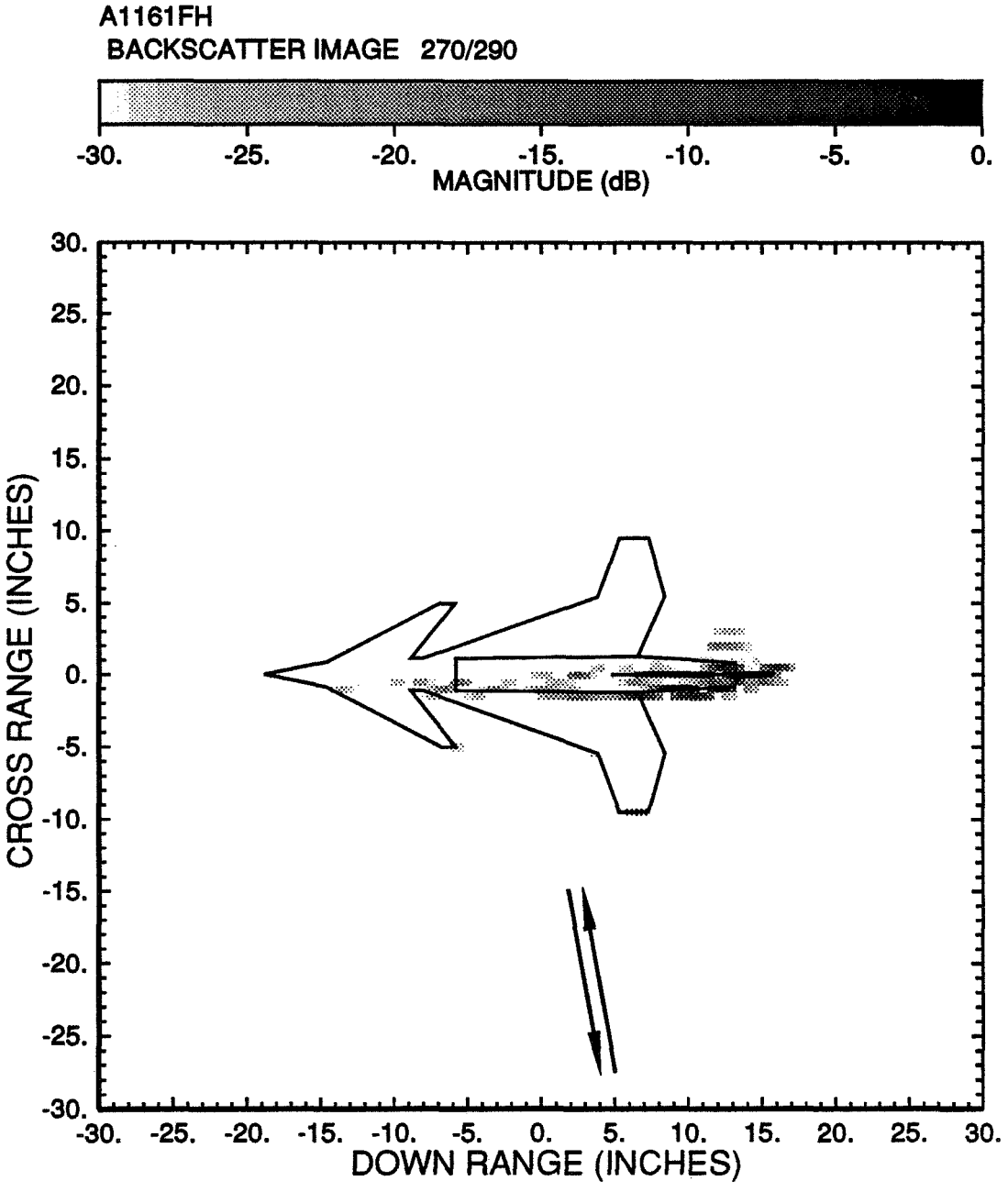

Figure 2.28: Backscatter ISAR image of the model aircraft. ($\theta = 280° \pm 10°$).

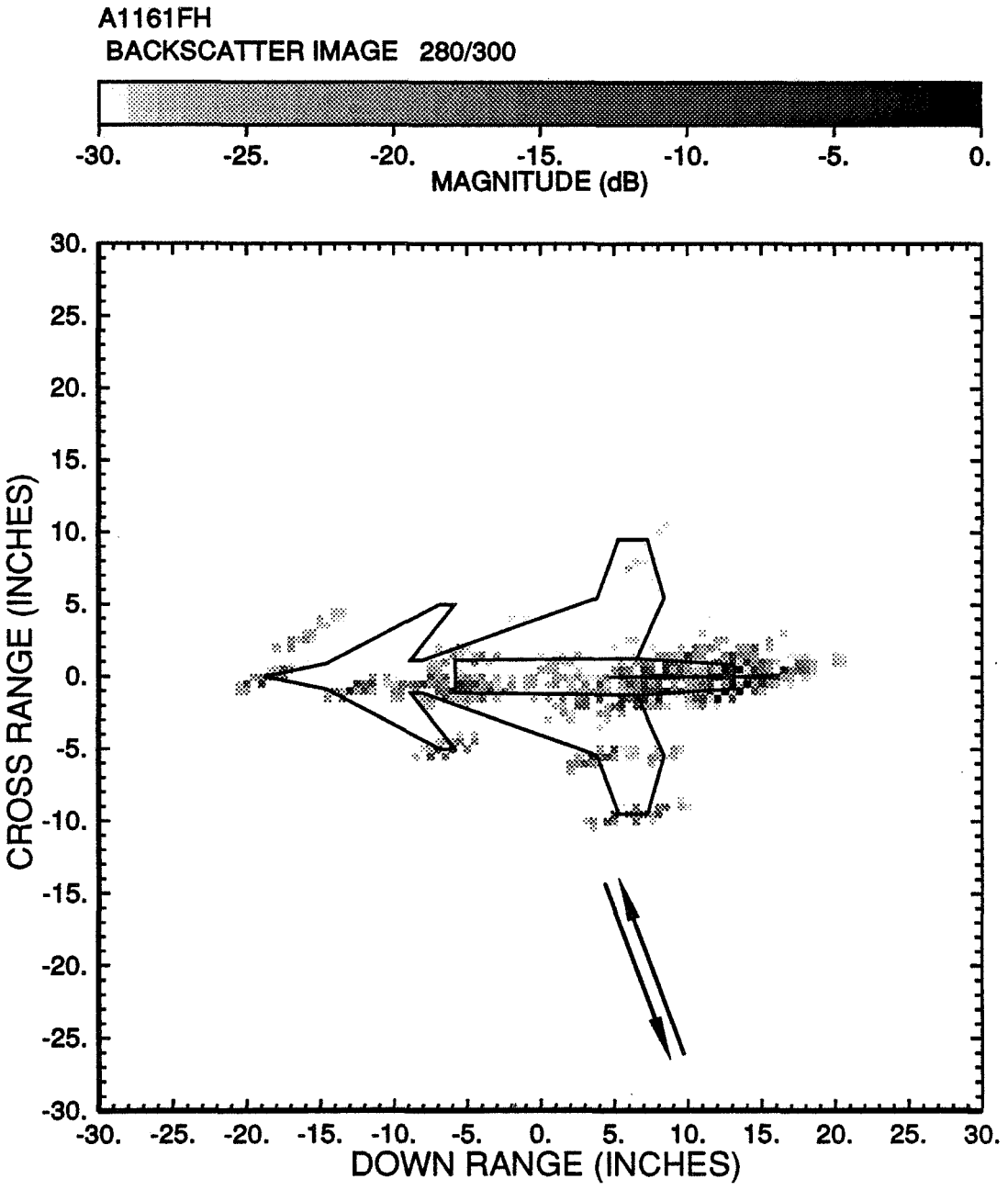

Figure 2.29: Backscatter ISAR image of the model aircraft. ($\theta = 290° \pm 10°$).

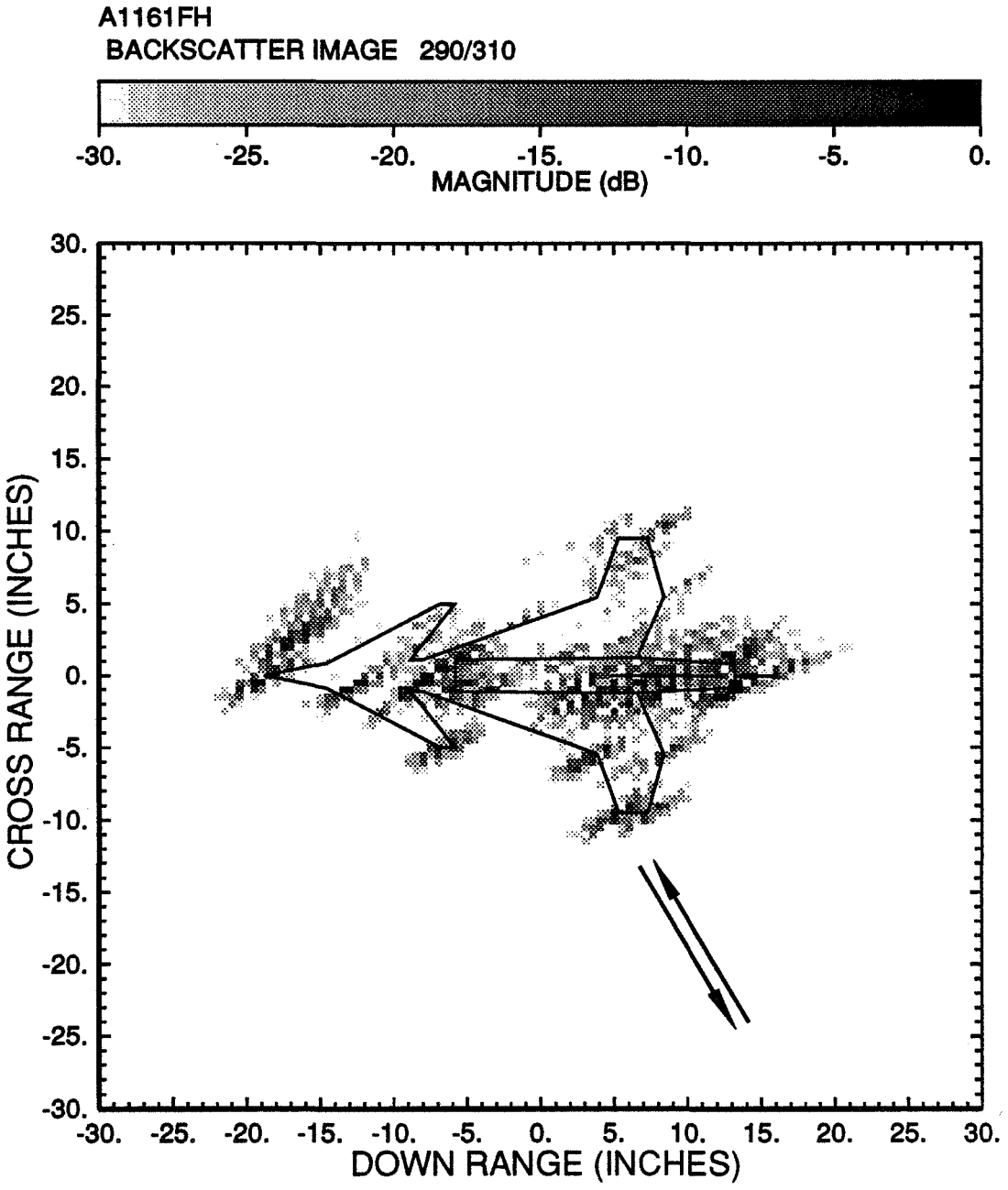

Figure 2.30: Backscatter ISAR image of the model aircraft. ($\theta = 300° \pm 10°$).

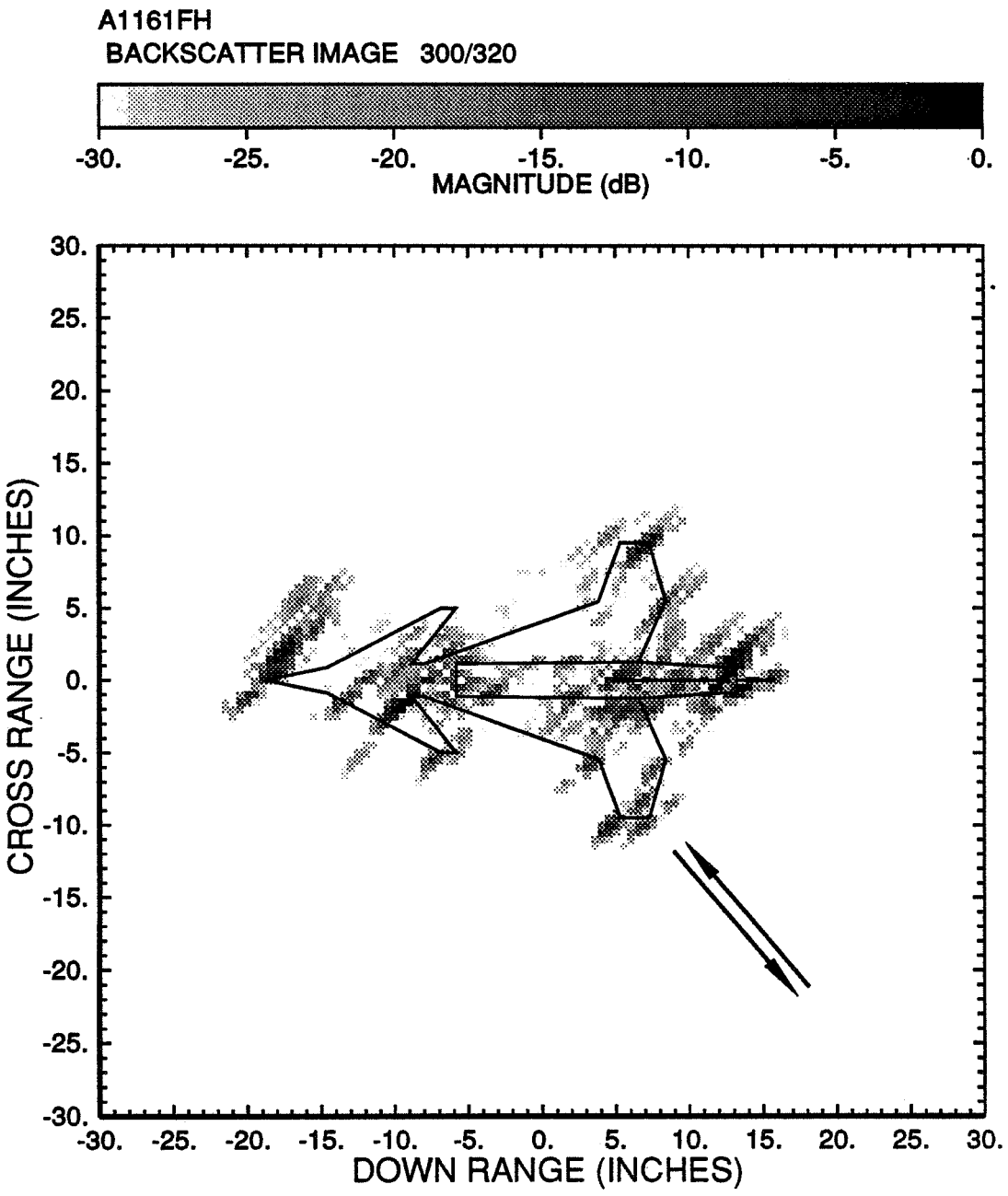

Figure 2.31: Backscatter ISAR image of the model aircraft. ($\theta = 310° \pm 10°$).

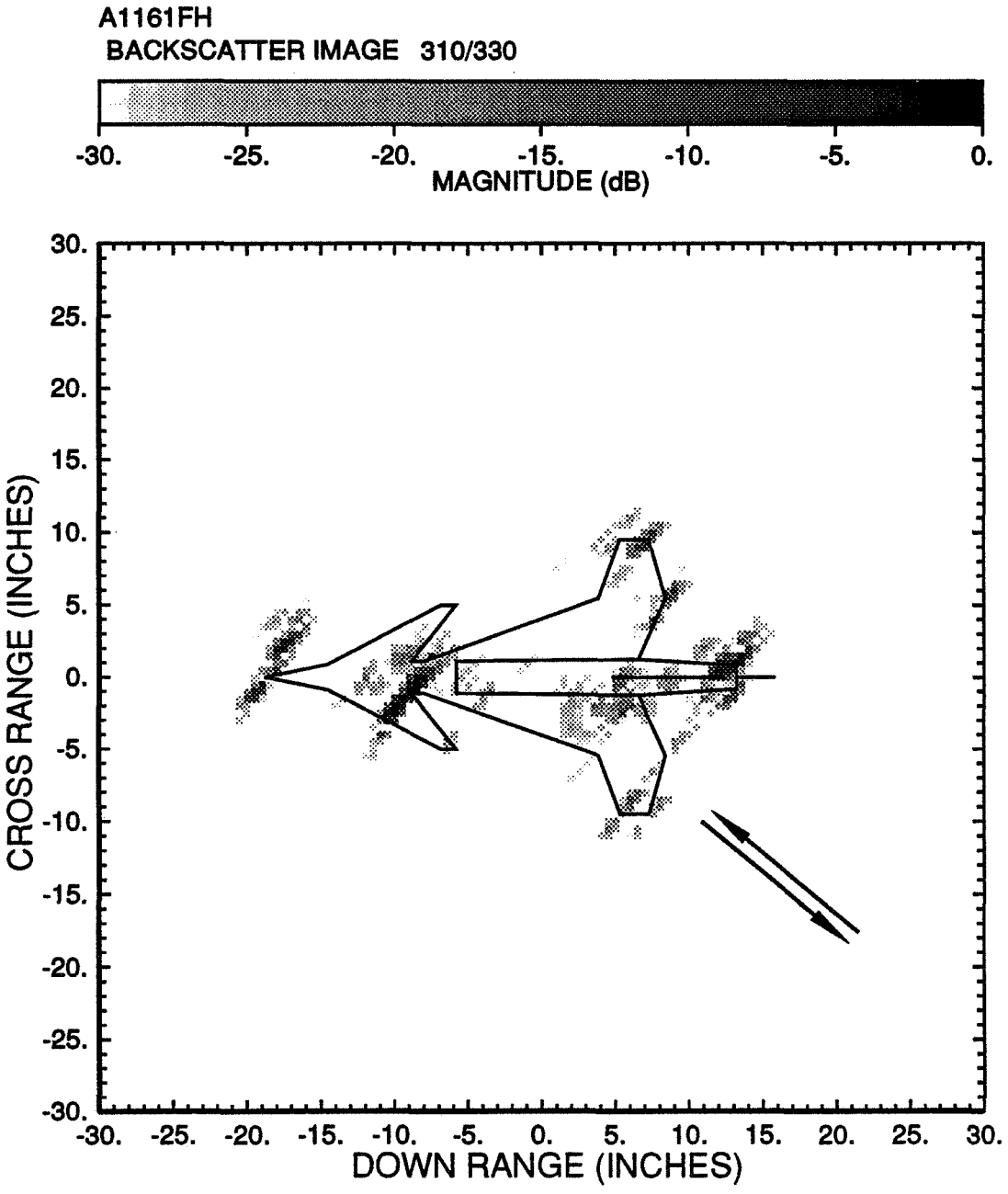

Figure 2.32: Backscatter ISAR image of the model aircraft. ($\theta = 320° \pm 10°$).

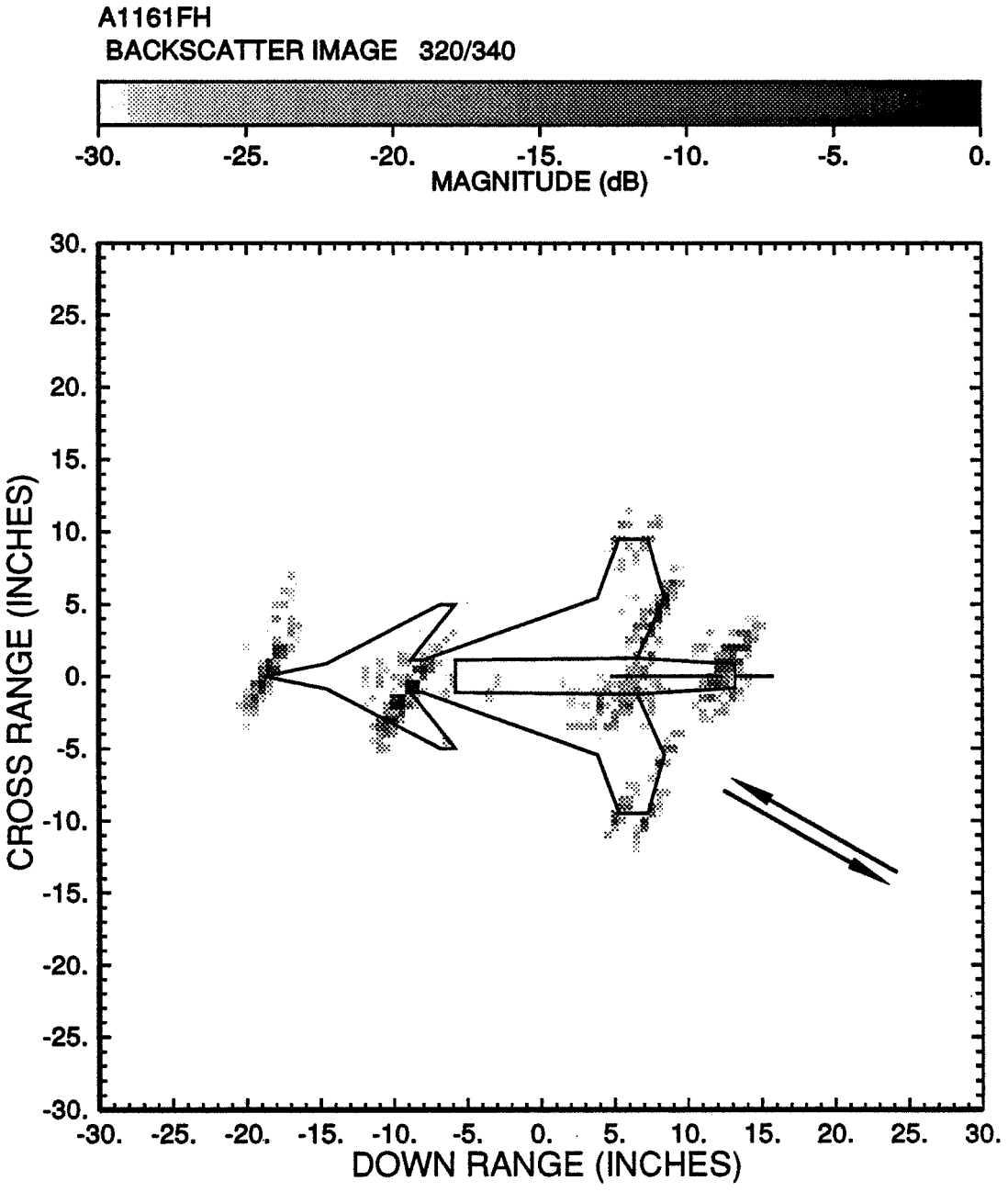

Figure 2.33: Backscatter ISAR image of the model aircraft. ($\theta = 330° \pm 10°$).

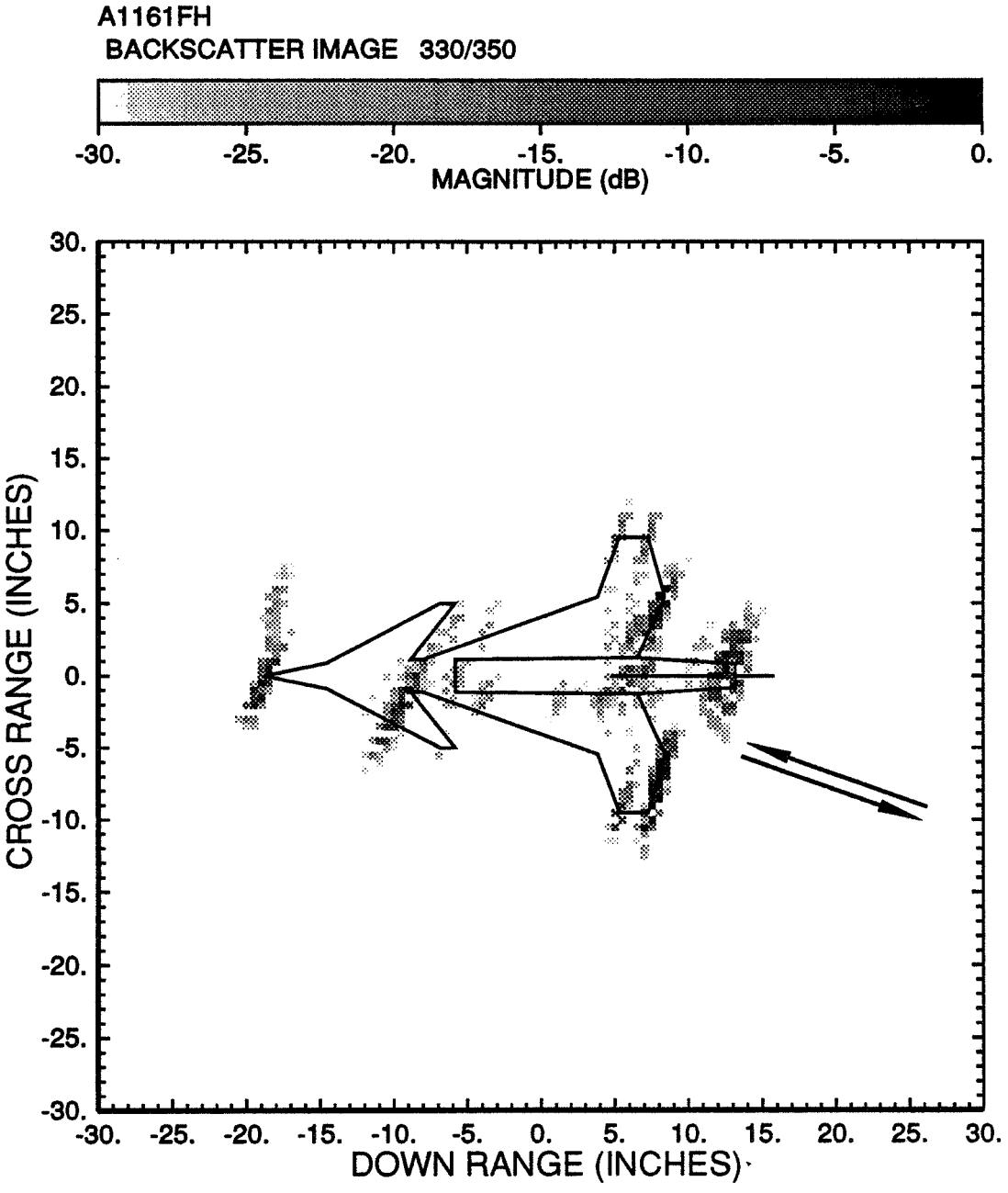

Figure 2.34: Backscatter ISAR image of the model aircraft. ($\theta = 340° \pm 10°$).

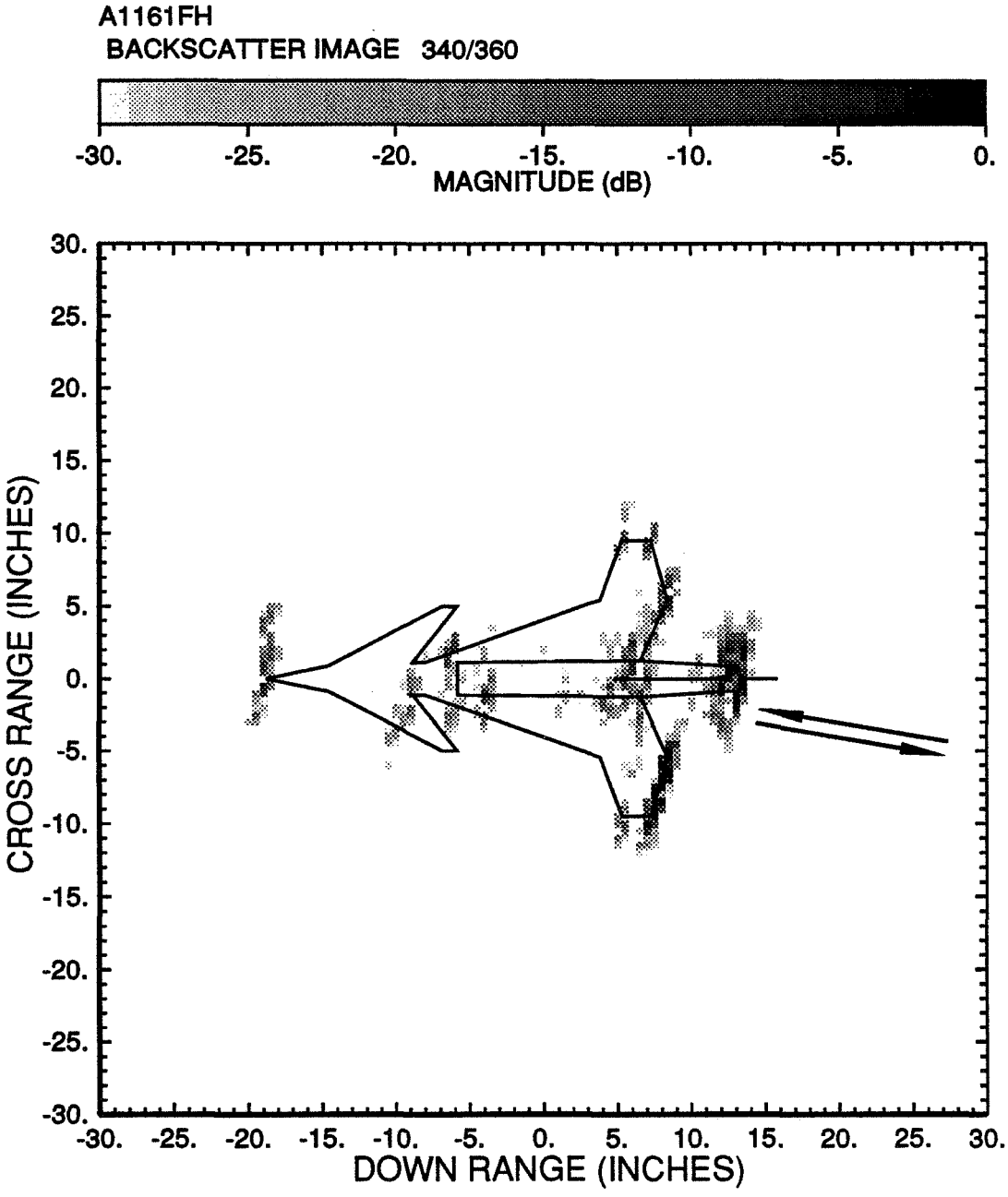

Figure 2.35: Backscatter ISAR image of the model aircraft. ($\theta = 350° \pm 10°$).

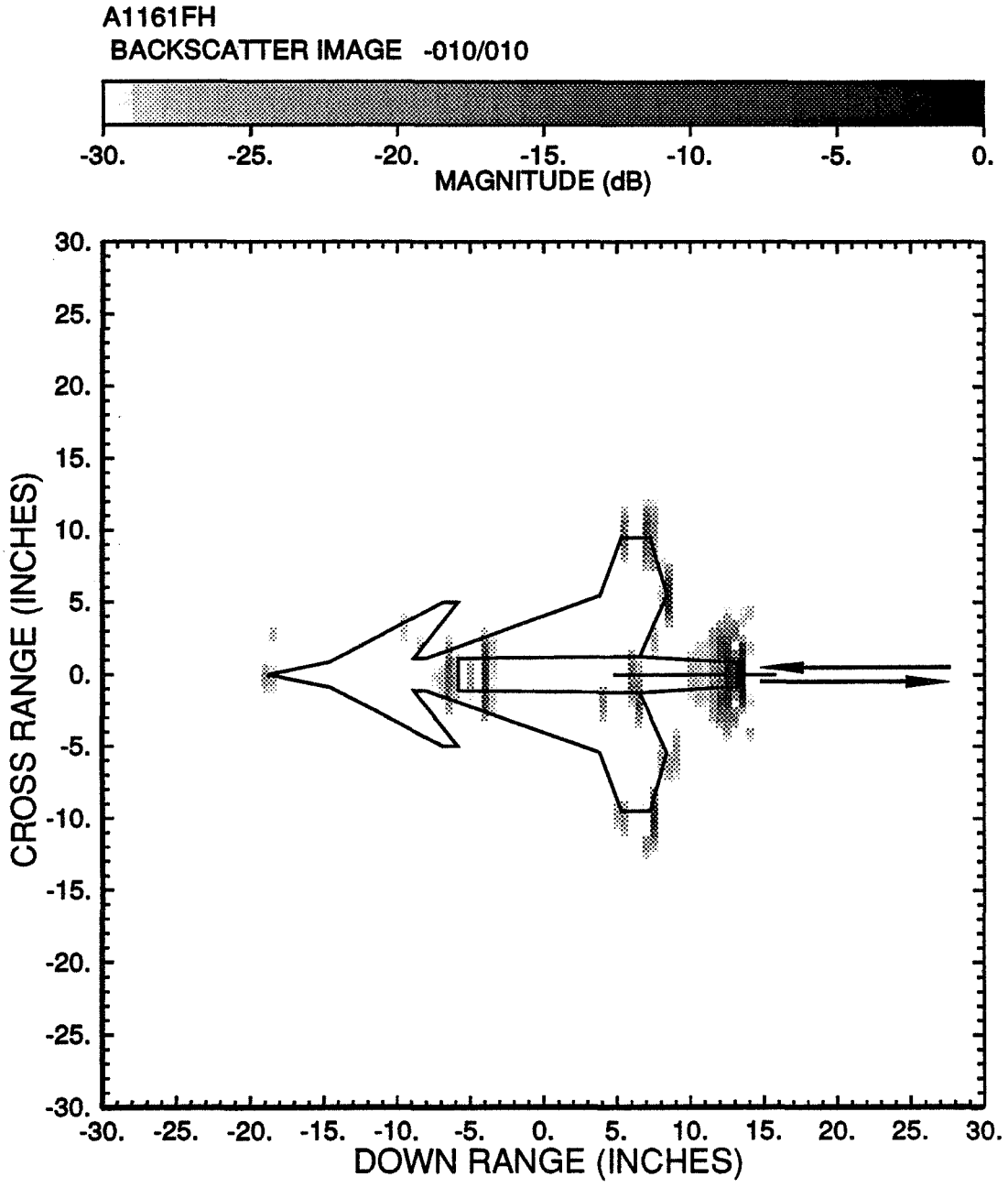

Figure 2.36: Backscatter ISAR image of the model aircraft. ($\theta = 360° \pm 10°$).

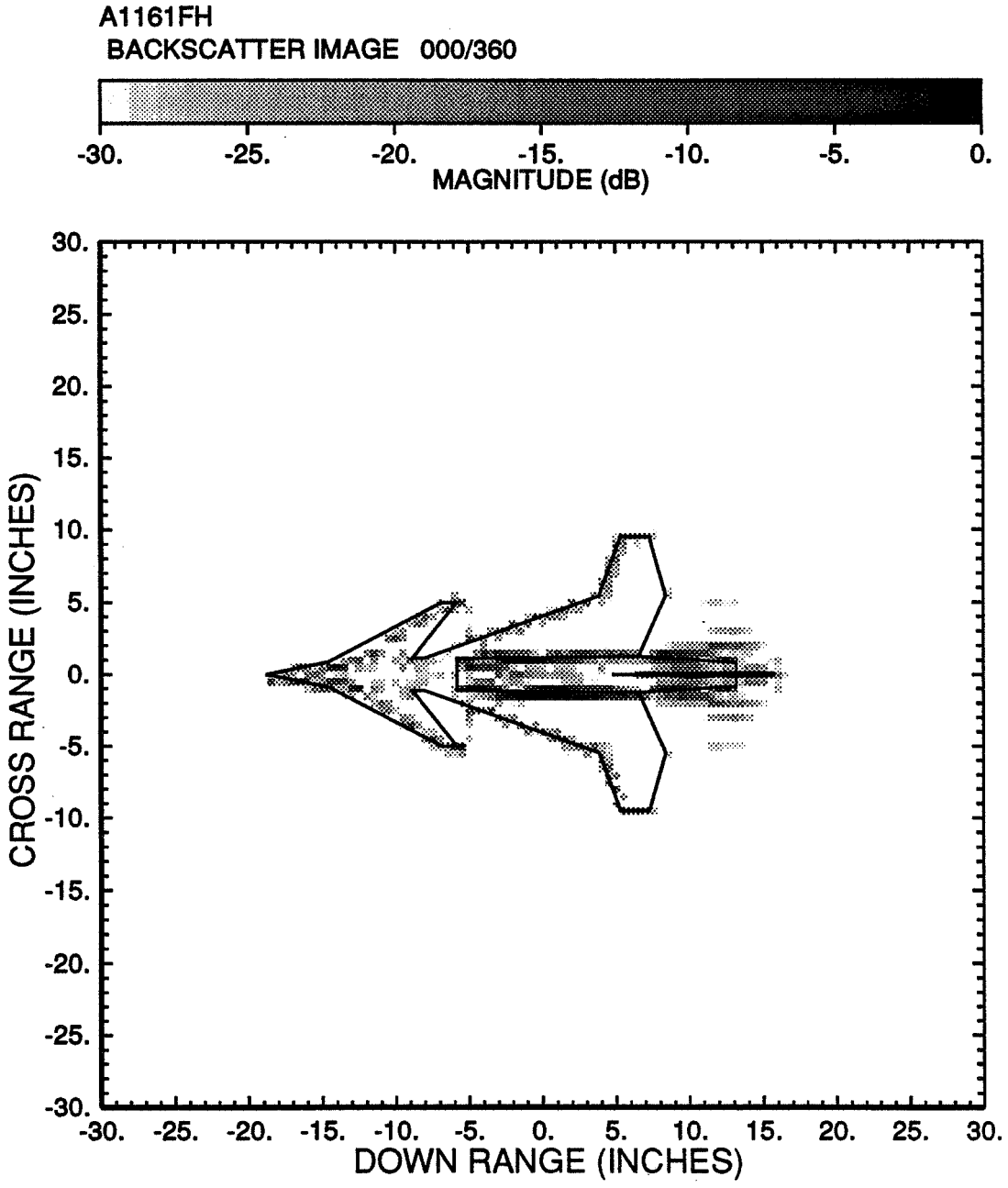

Figure 2.37: Backscatter ISAR image of the model aircraft. (complete 360°).

Chapter 3

Bistatic Images of the $32'' \times 19''$ Model Aircraft for $90°$ Bistatic Angle

This chapter summarizes the ISAR images of the model aircraft processed from the measured bistatic scattered fields for horizontal polarization. The compact range was used as the transmitting antenna, and a 2-18 GHz broad band double ridge horn was used as the receiving antenna as shown in Figure 3.1. The receiving antenna was located $216''$ north relative to the target and was in the near field of the target. Consequently, the bistatic angle is $90°$. The bistatic ISAR images ($90°$ bistatic angle) for mean incident angles from $10°$ to $360°$ with a $10°$ step are shown in Figures 3.2 to 3.37. The image for each mean incident angle was normalized with respect to its own maximum. The simplified outline of the model aircraft is also shown in these images so that one can identify the scattering centers. One should notice that the cross range image of the target is perpendicular to the direction which bisects the incident and scattering directions. The complete $360°$ image is shown in Figure 3.38.

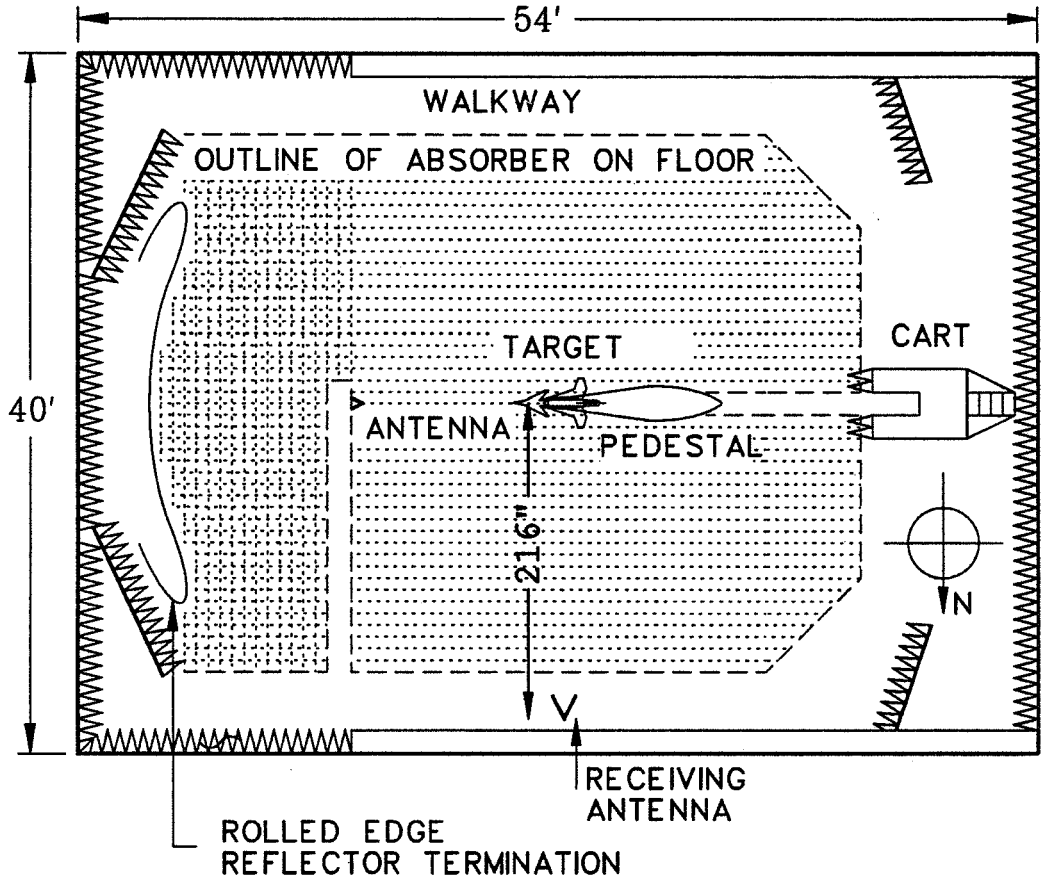

Figure 3.1: Bistatic scattered field measurement setup in OSU-ESL compact range. (90° bistatic angle).

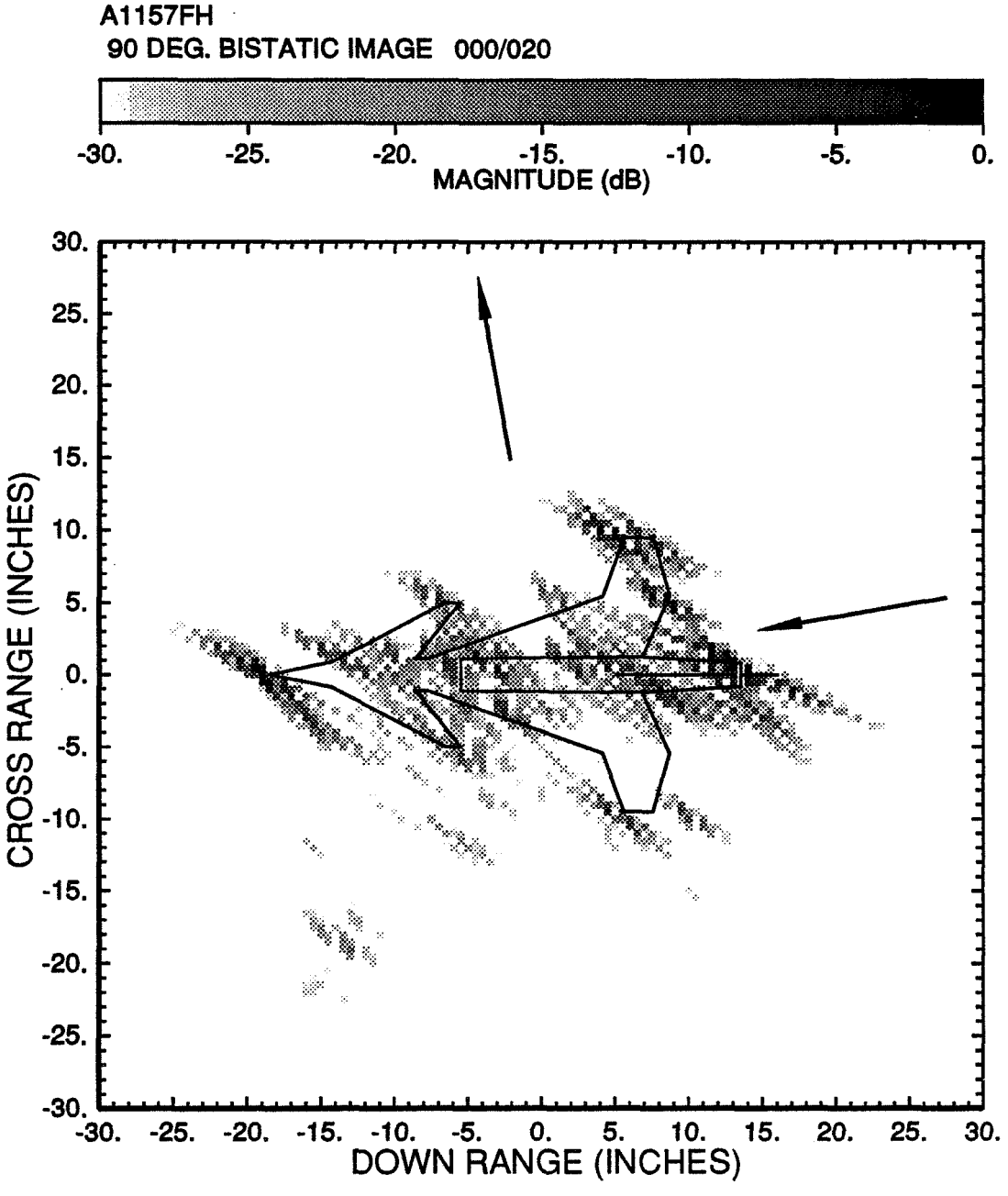

Figure 3.2: Bistatic ISAR image of the model aircraft. (90° bistatic angle, $\theta = 10° \pm 10°$).

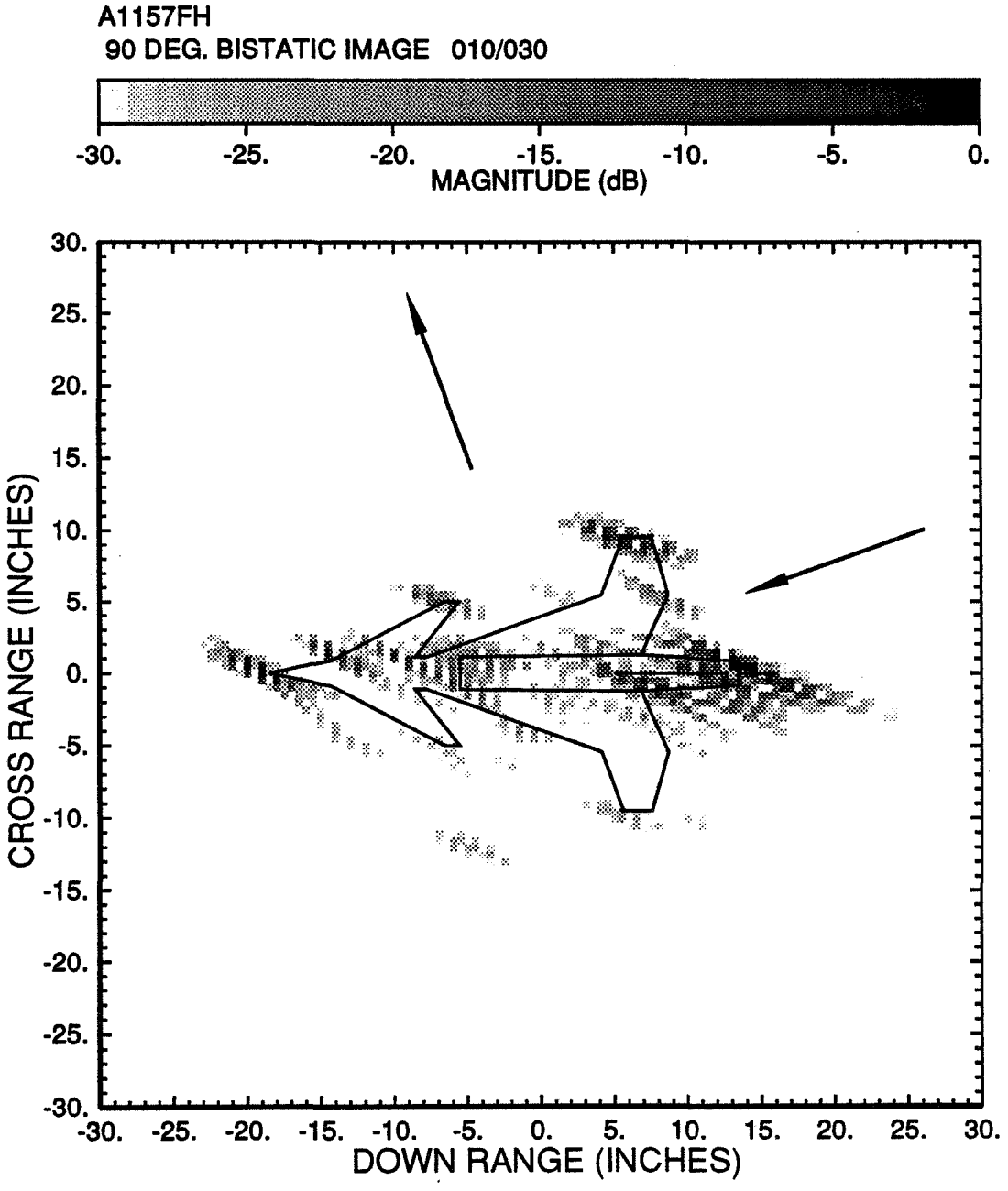

Figure 3.3: Bistatic ISAR image of the model aircraft. (90° bistatic angle, $\theta = 20° \pm 10°$).

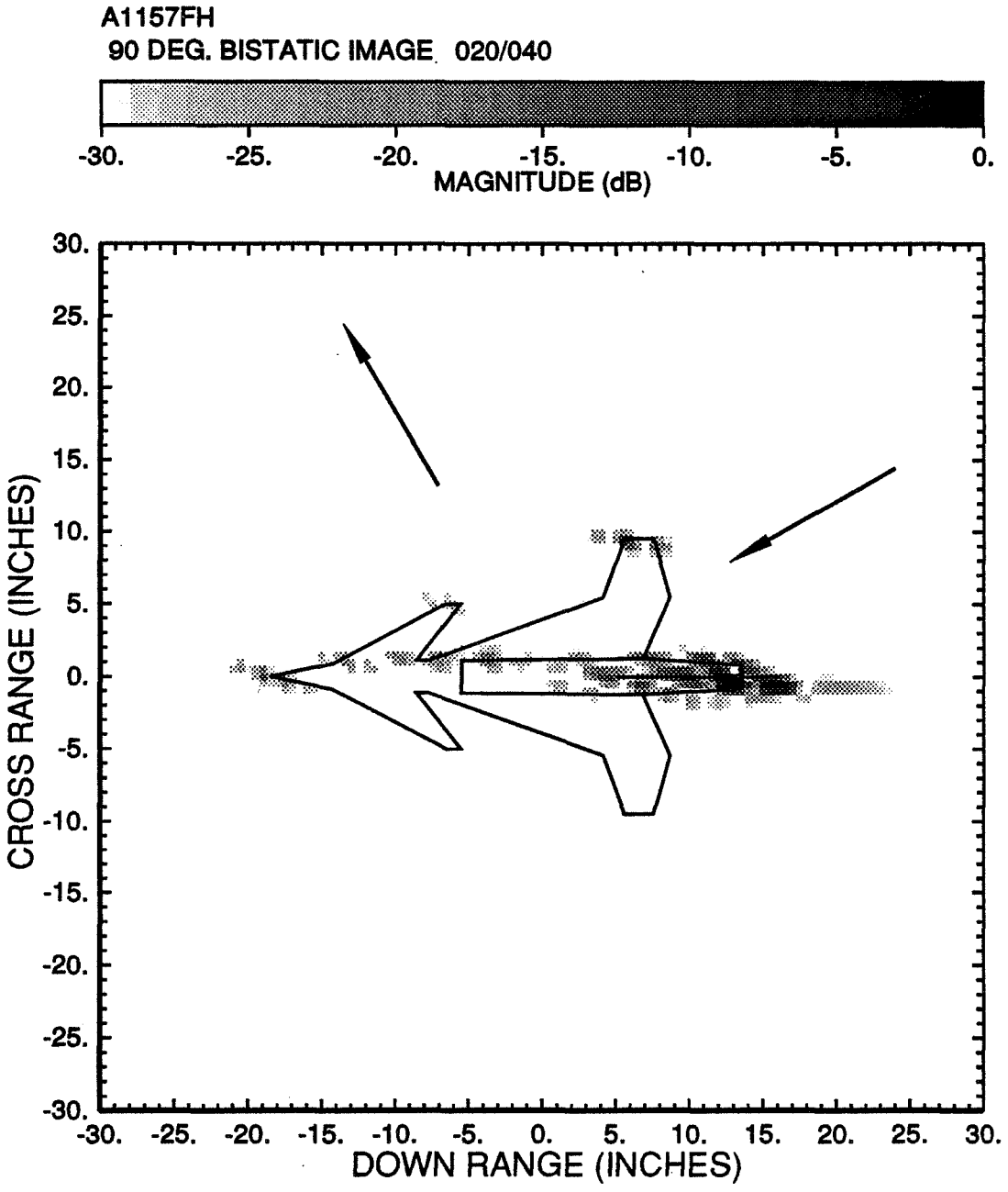

Figure 3.4: Bistatic ISAR image of the model aircraft. (90° bistatic angle, $\theta = 30° \pm 10°$).

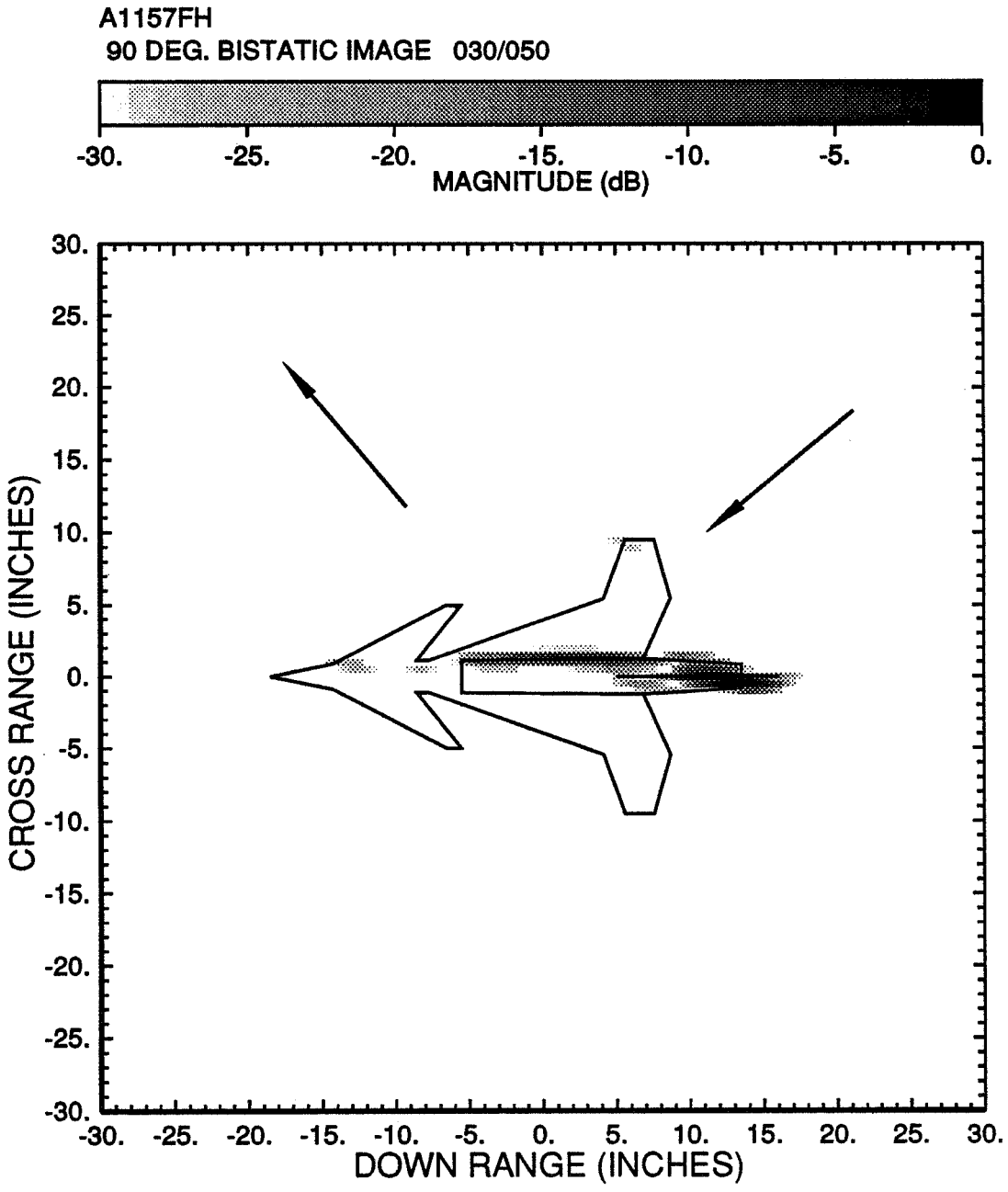

Figure 3.5: Bistatic ISAR image of the model aircraft. (90° bistatic angle, $\theta = 40° \pm 10°$).

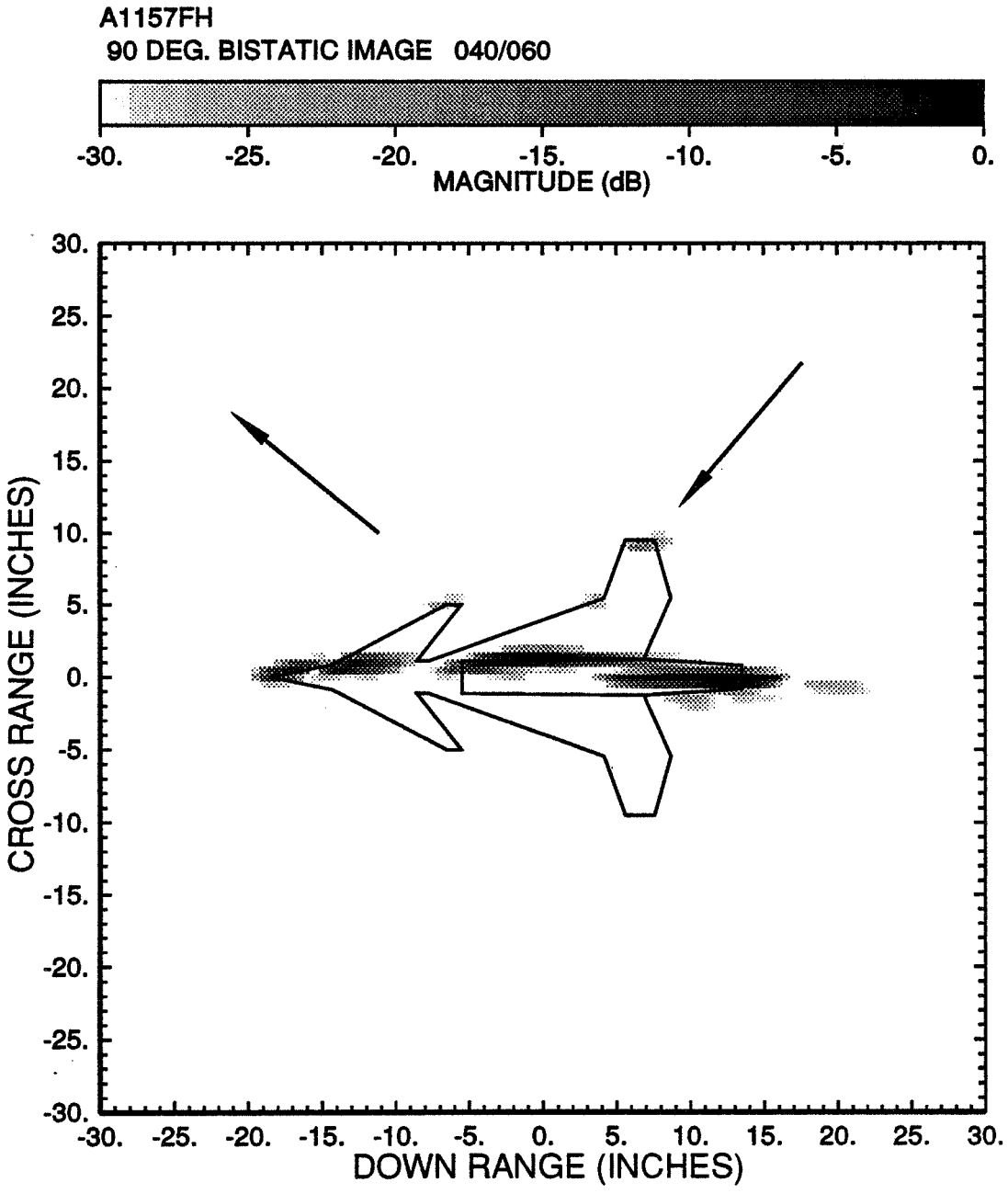

Figure 3.6: Bistatic ISAR image of the model aircraft. (90° bistatic angle, $\theta = 50° \pm 10°$).

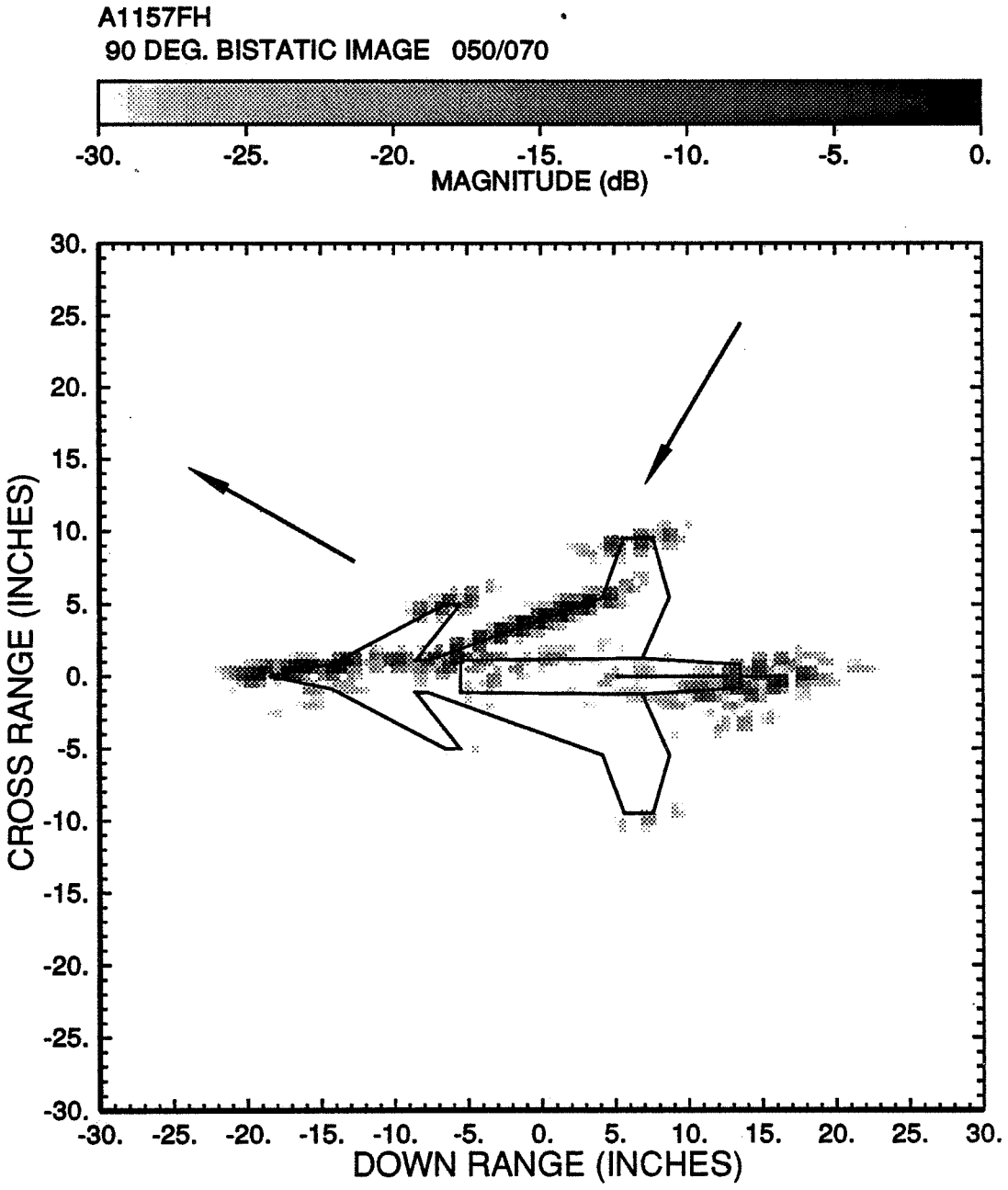

Figure 3.7: Bistatic ISAR image of the model aircraft. (90° bistatic angle, $\theta = 60° \pm 10°$).

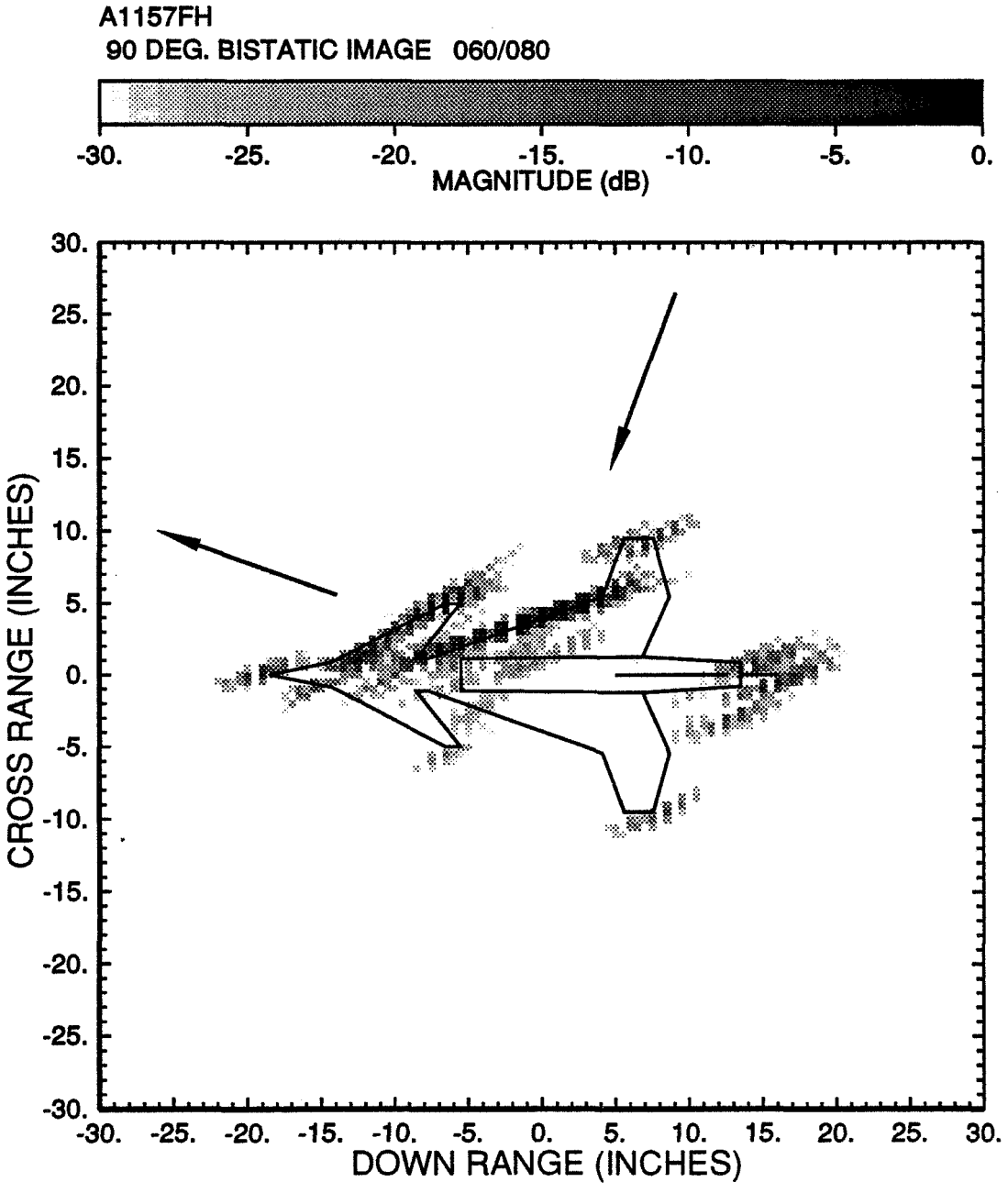

Figure 3.8: Bistatic ISAR image of the model aircraft. (90° bistatic angle, $\theta = 70° \pm 10°$).

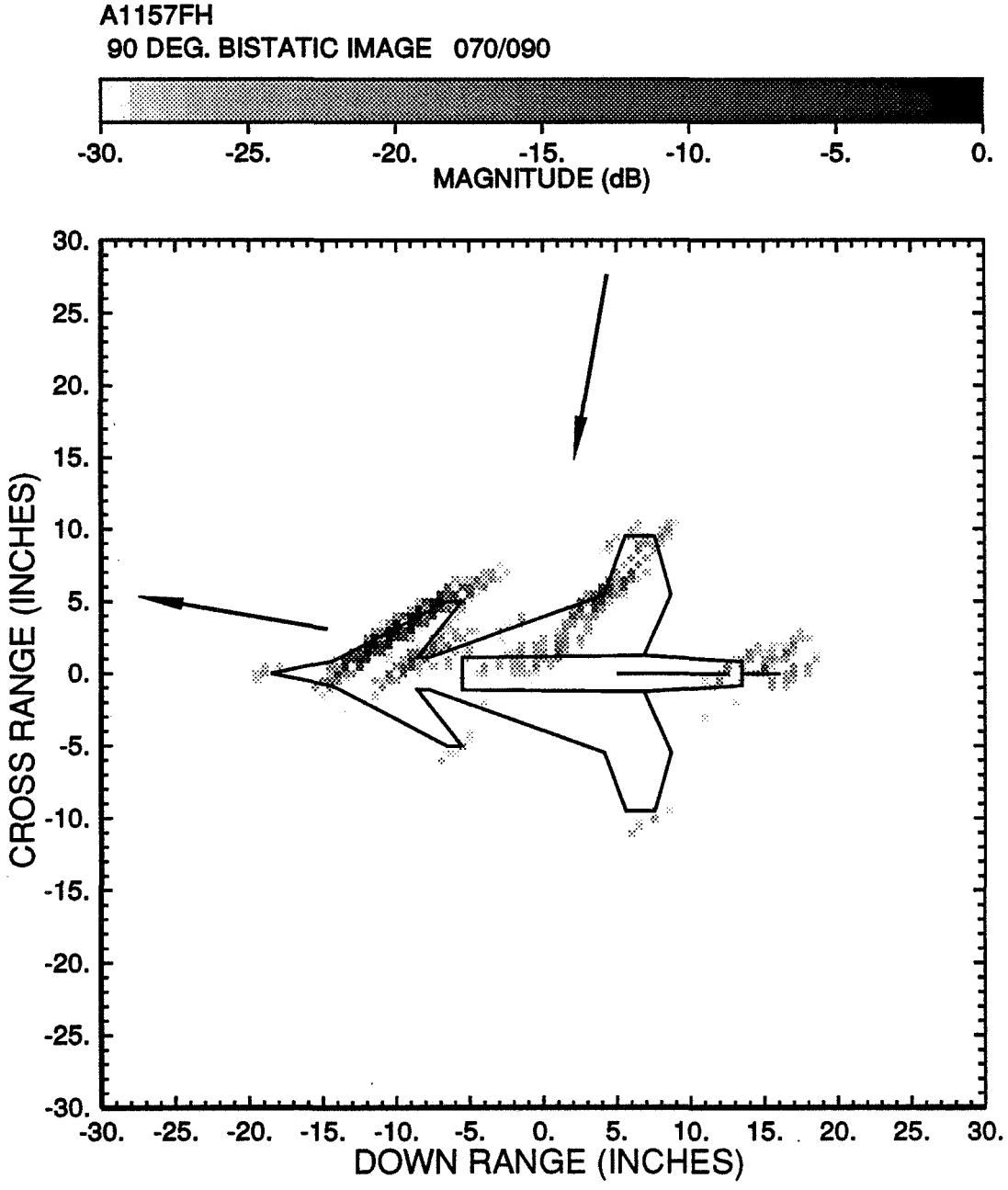

Figure 3.9: Bistatic ISAR image of the model aircraft. (90° bistatic angle, $\theta = 80° \pm 10°$).

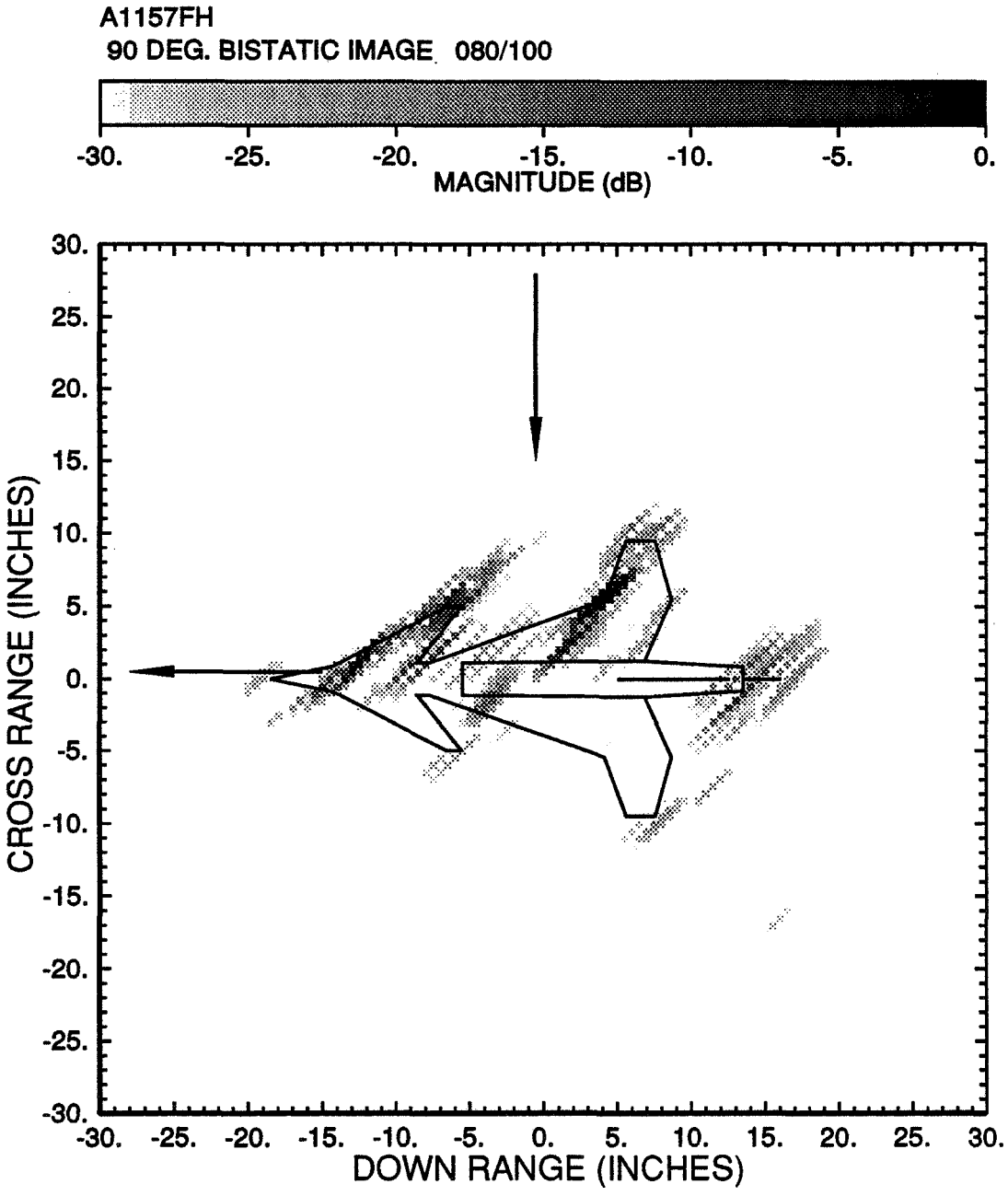

Figure 3.10: Bistatic ISAR image of the model aircraft. (90° bistatic angle, $\theta = 90° \pm 10°$).

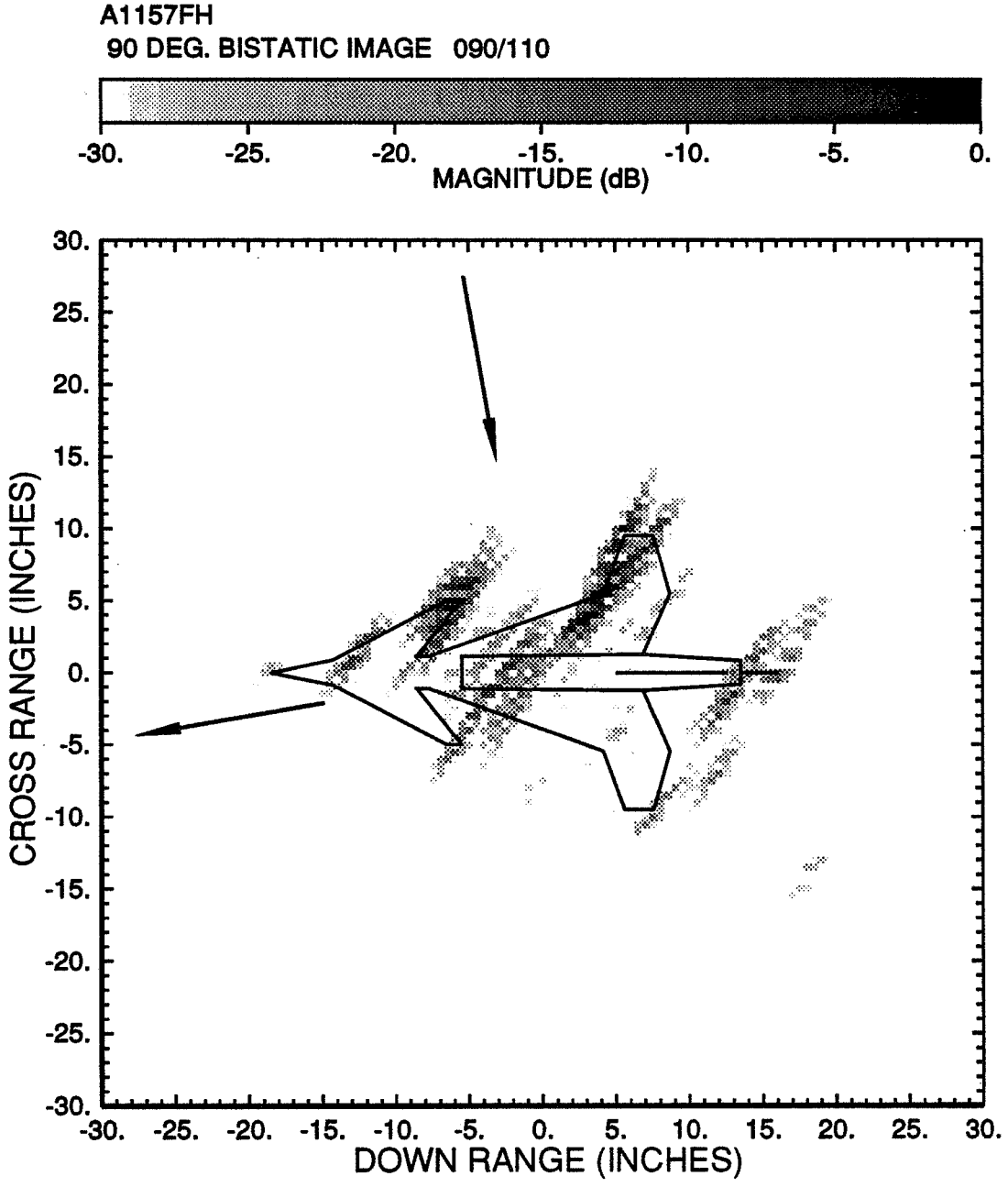

Figure 3.11: Bistatic ISAR image of the model aircraft. (90° bistatic angle, $\theta = 100° \pm 10°$).

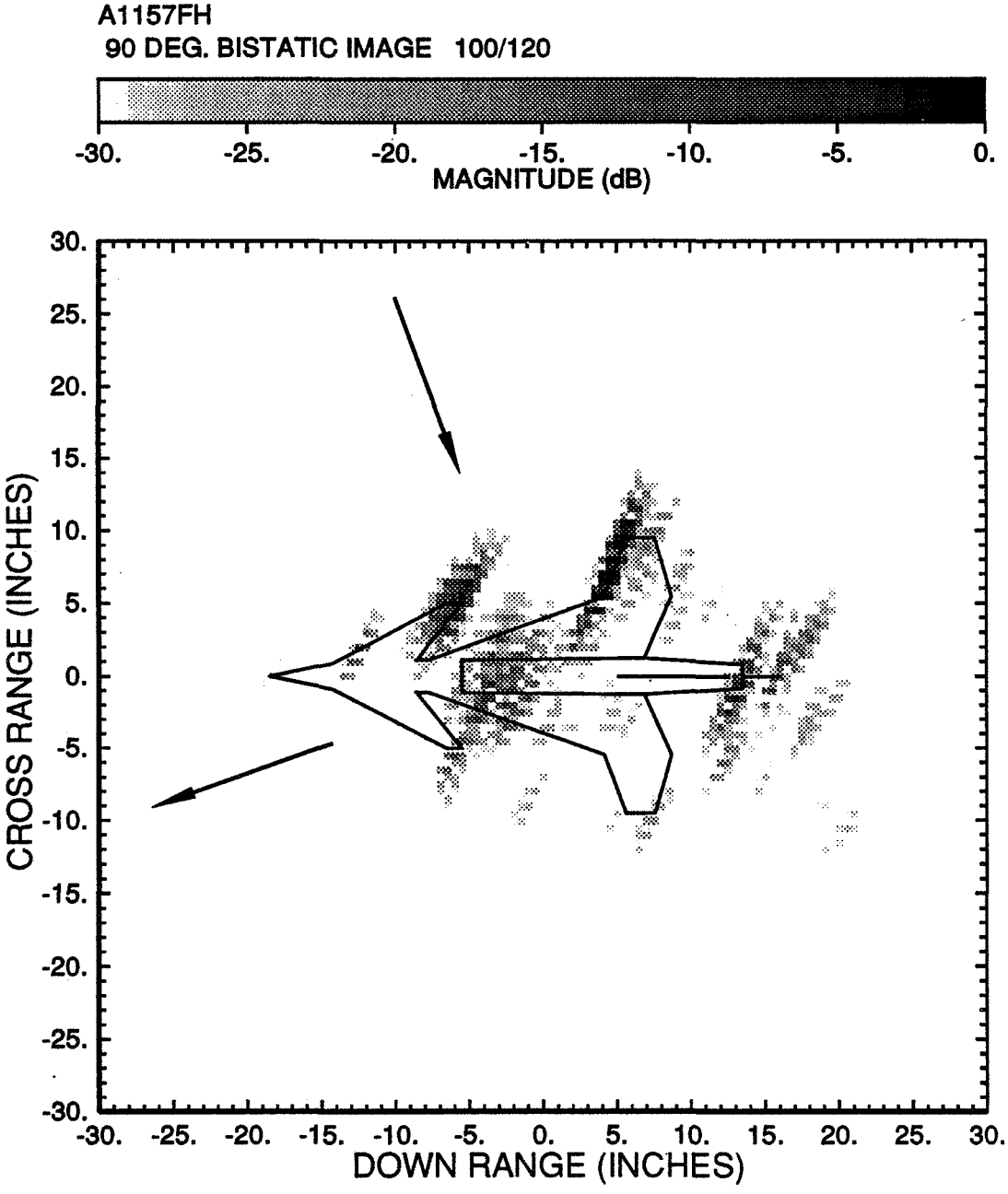

Figure 3.12: Bistatic ISAR image of the model aircraft. (90° bistatic angle, $\theta = 110° \pm 10°$).

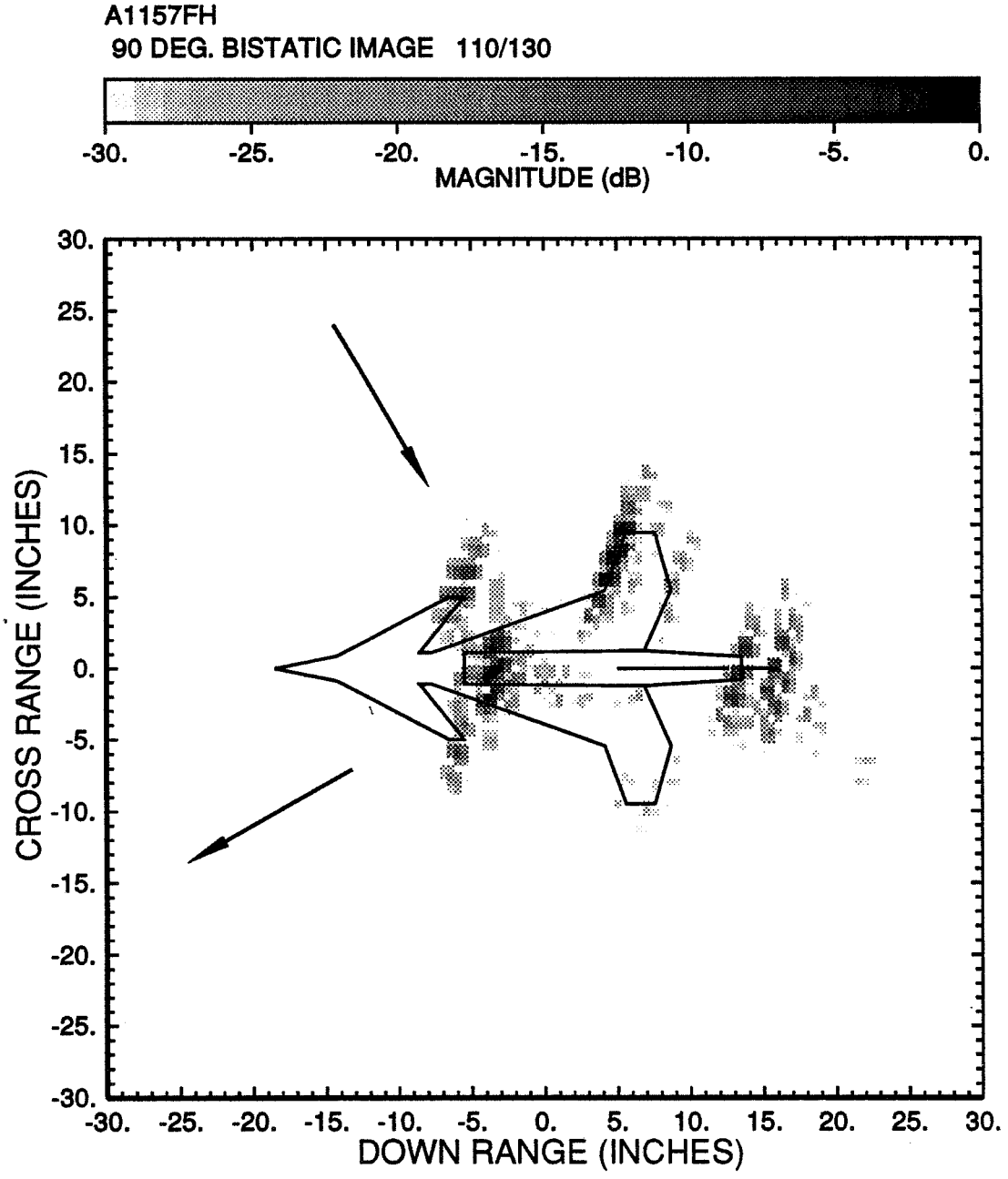

Figure 3.13: Bistatic ISAR image of the model aircraft. (90° bistatic angle, $\theta = 120° \pm 10°$).

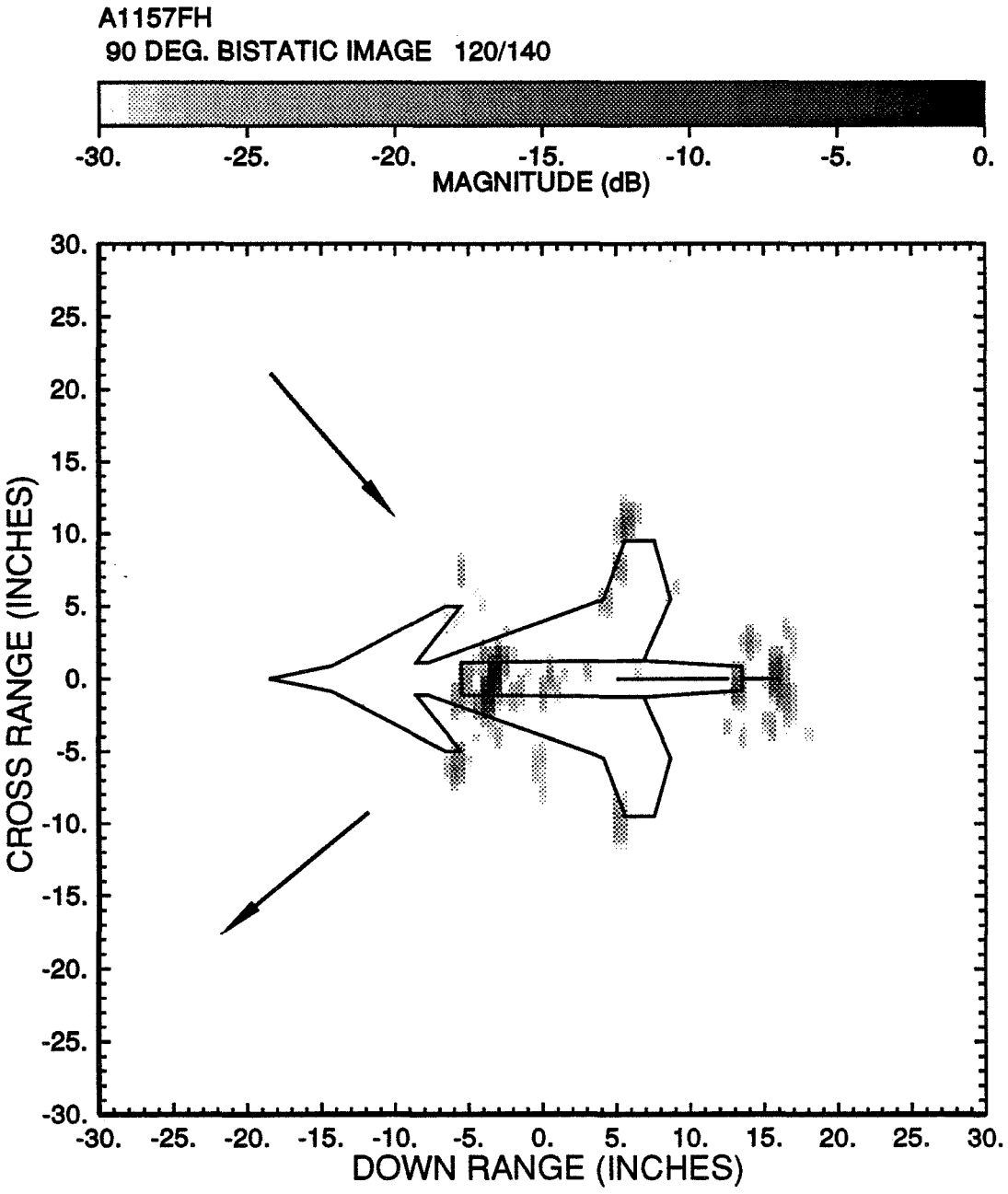

Figure 3.14: Bistatic ISAR image of the model aircraft. (90° bistatic angle, $\theta = 130° \pm 10°$).

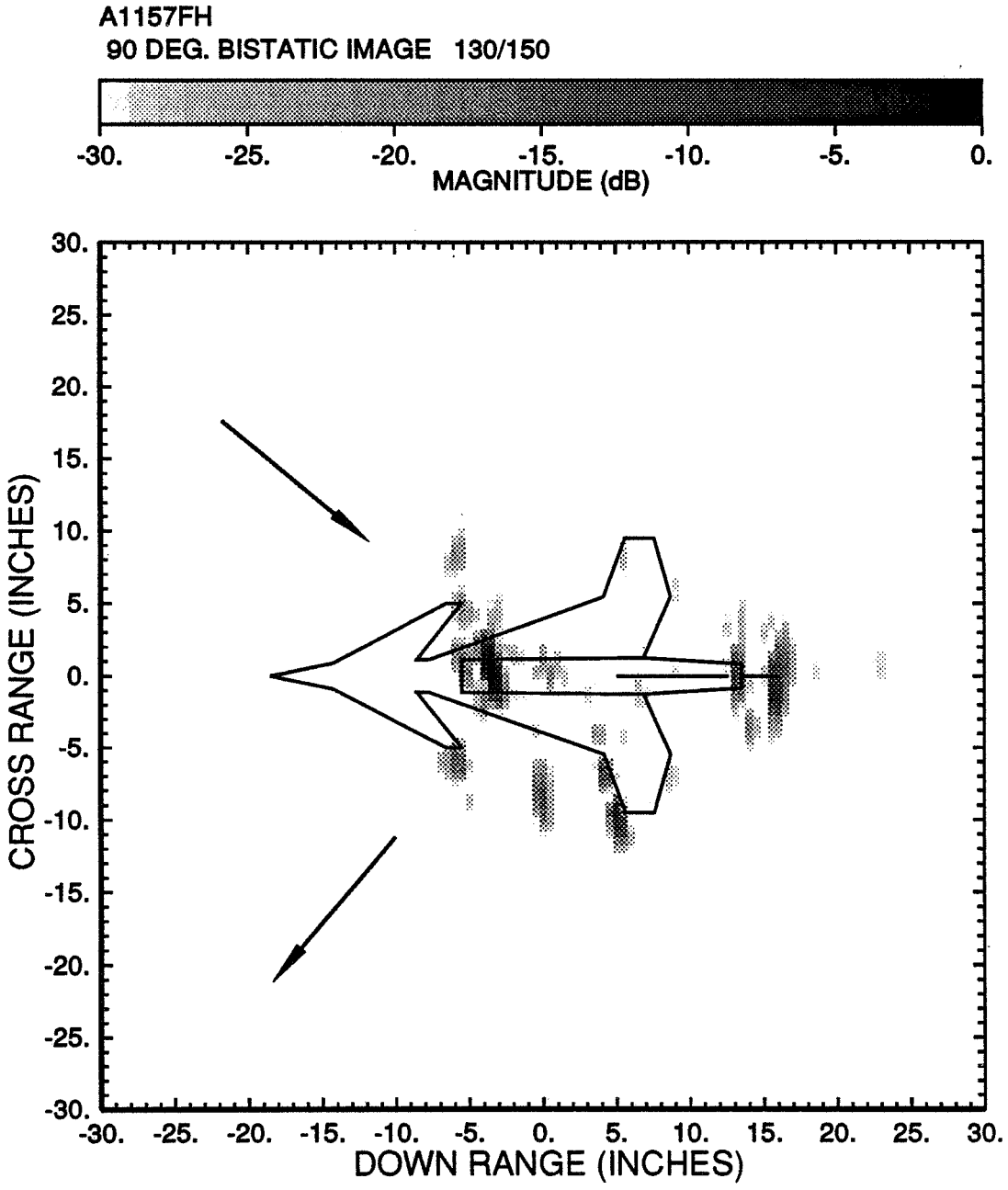

Figure 3.15: Bistatic ISAR image of the model aircraft. (90° bistatic angle, $\theta = 140° \pm 10°$).

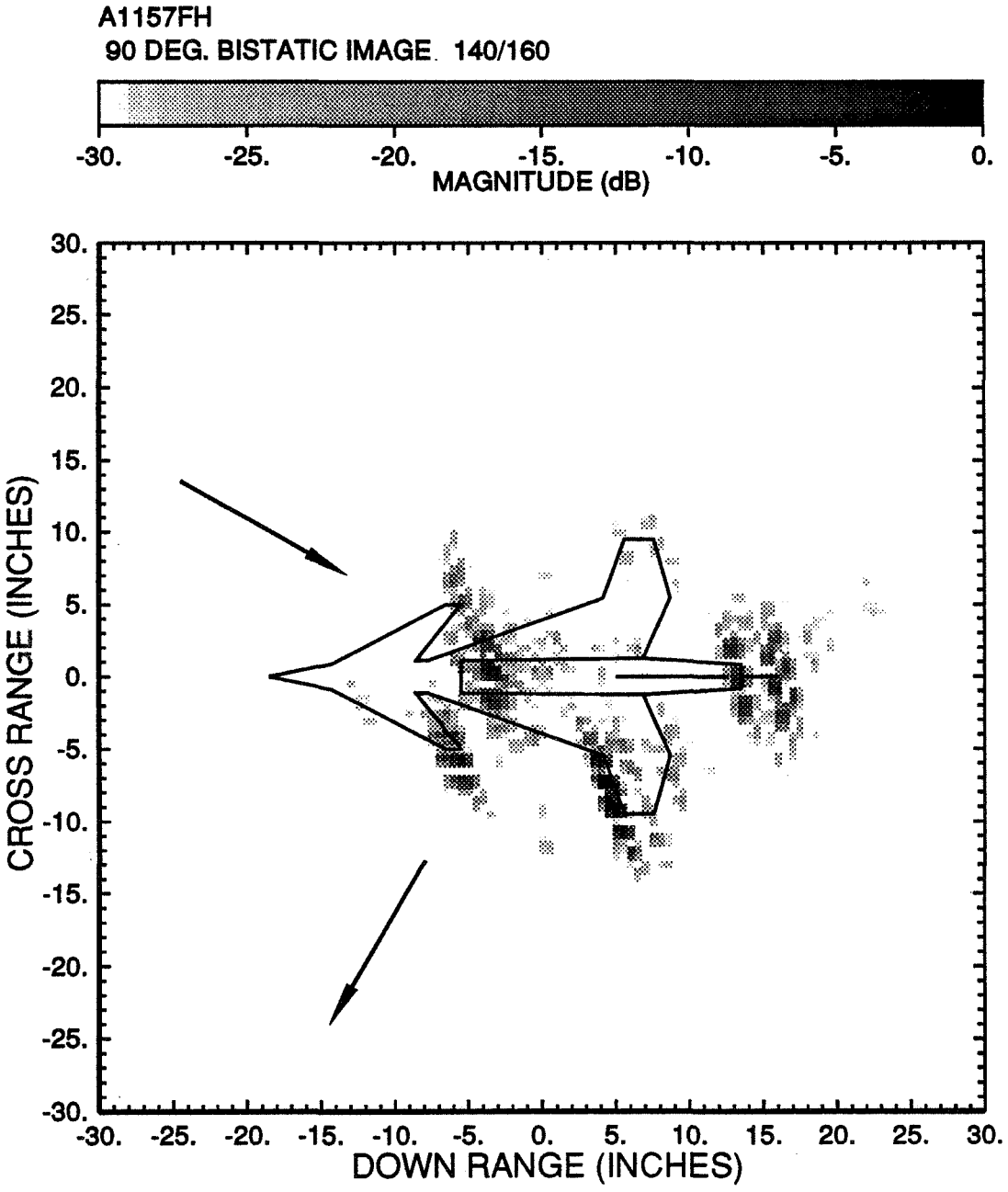

Figure 3.16: Bistatic ISAR image of the model aircraft. (90° bistatic angle, $\theta = 150° \pm 10°$).

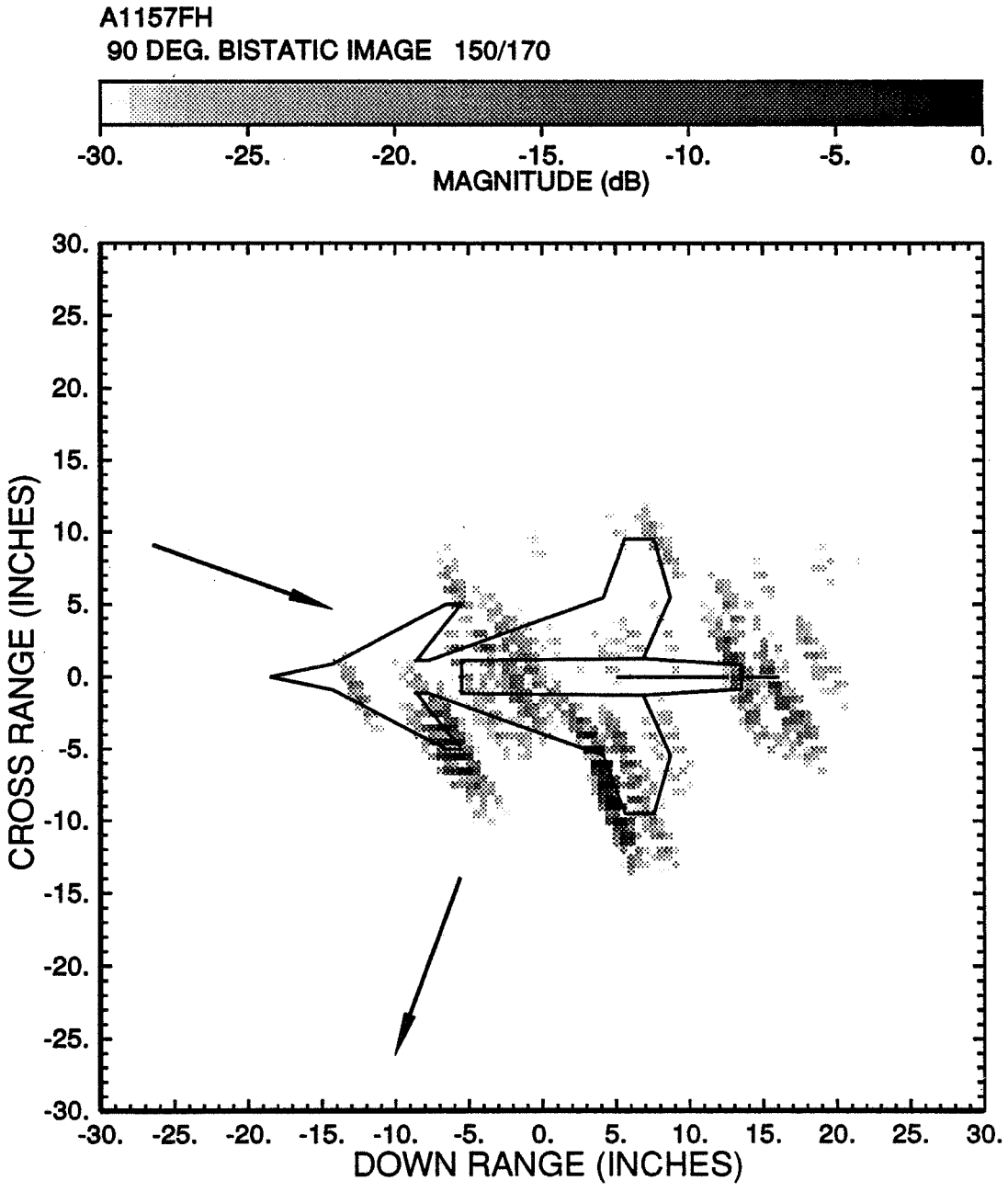

Figure 3.17: Bistatic ISAR image of the model aircraft. (90° bistatic angle, $\theta = 160° \pm 10°$).

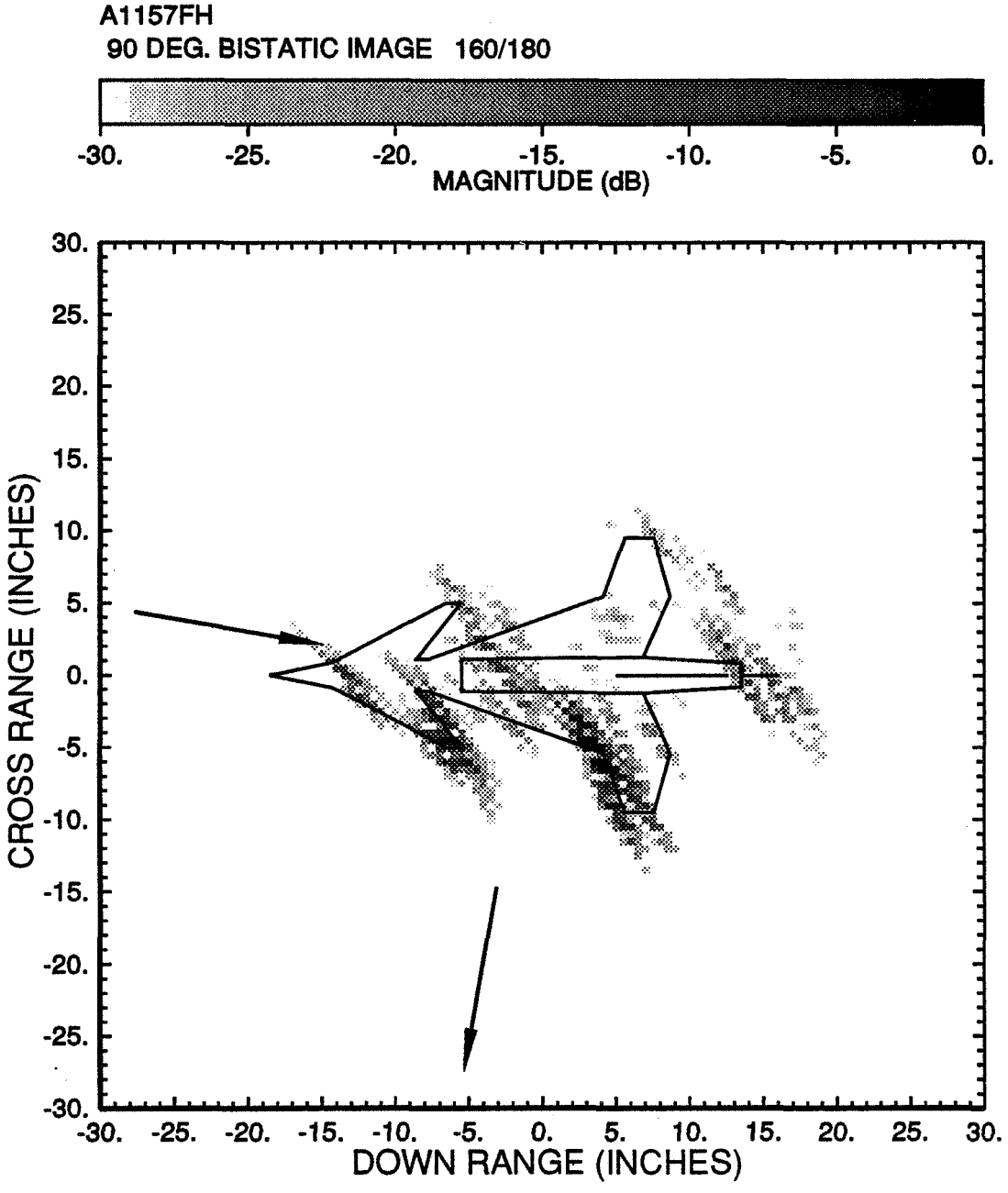

Figure 3.18: Bistatic ISAR image of the model aircraft. (90° bistatic angle, $\theta = 170° \pm 10°$).

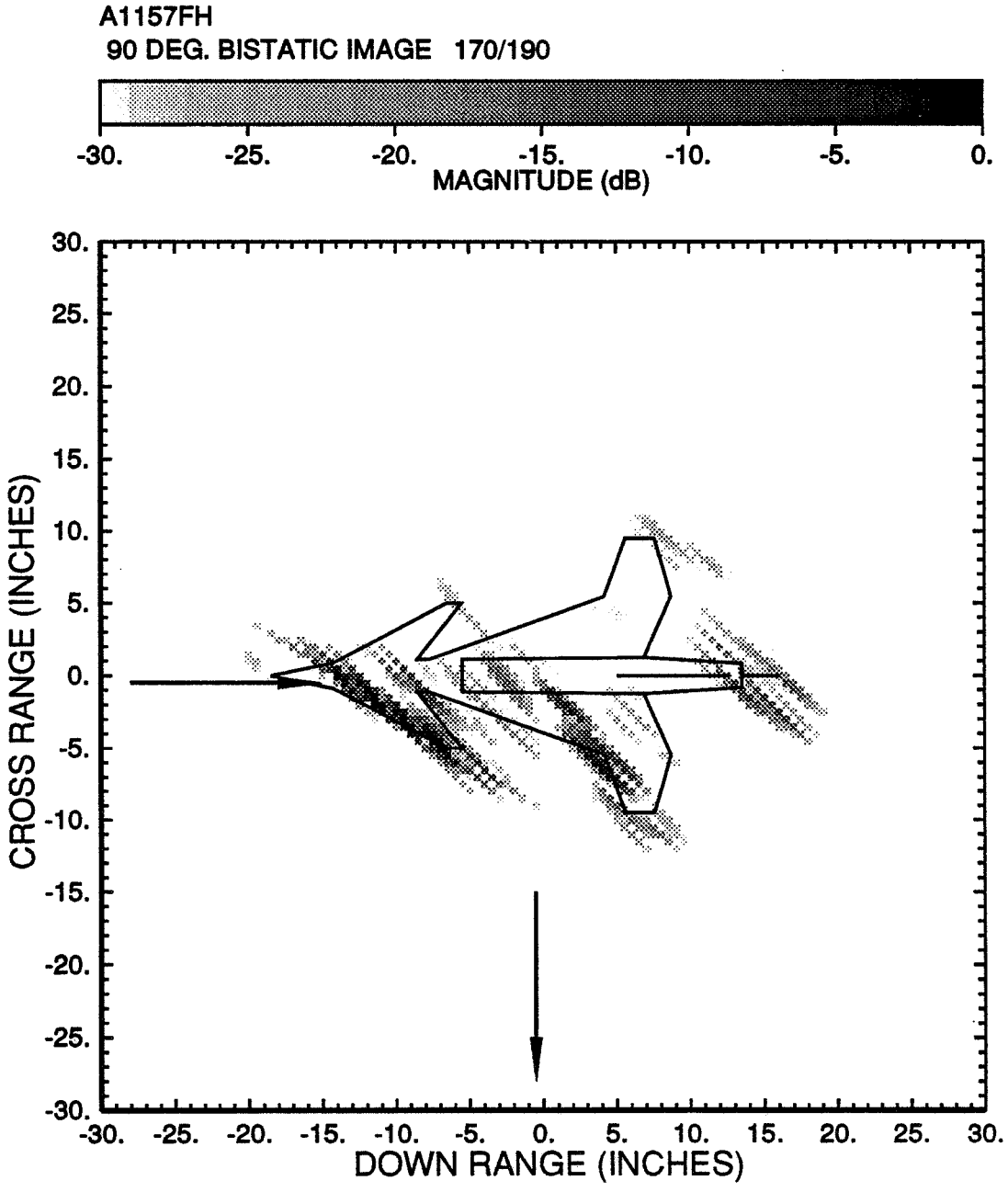

Figure 3.19: Bistatic ISAR image of the model aircraft. (90° bistatic angle, $\theta = 180° \pm 10°$).

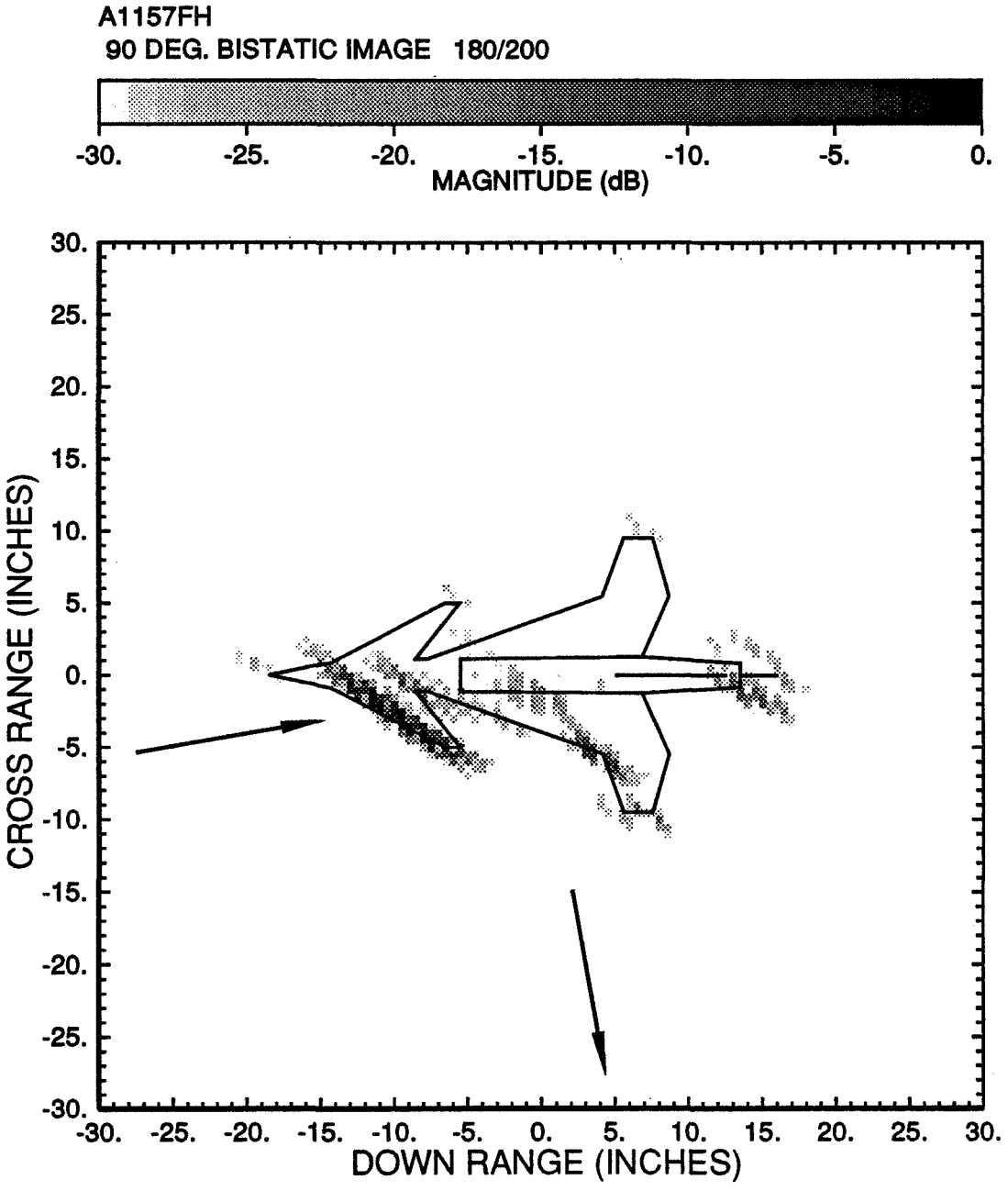

Figure 3.20: Bistatic ISAR image of the model aircraft. (90° bistatic angle, $\theta = 190° \pm 10°$).

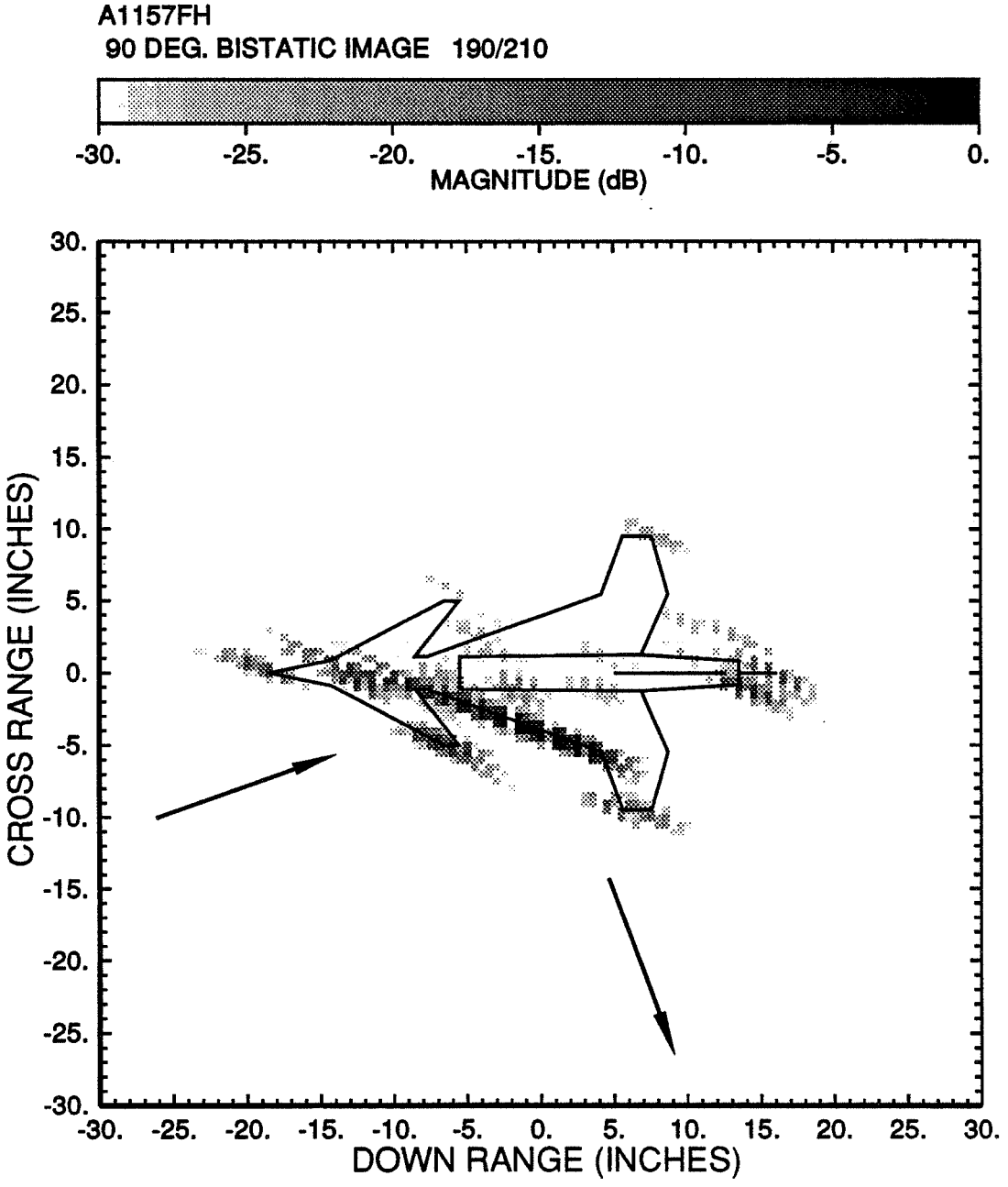

Figure 3.21: Bistatic ISAR image of the model aircraft. (90° bistatic angle, $\theta = 200° \pm 10°$).

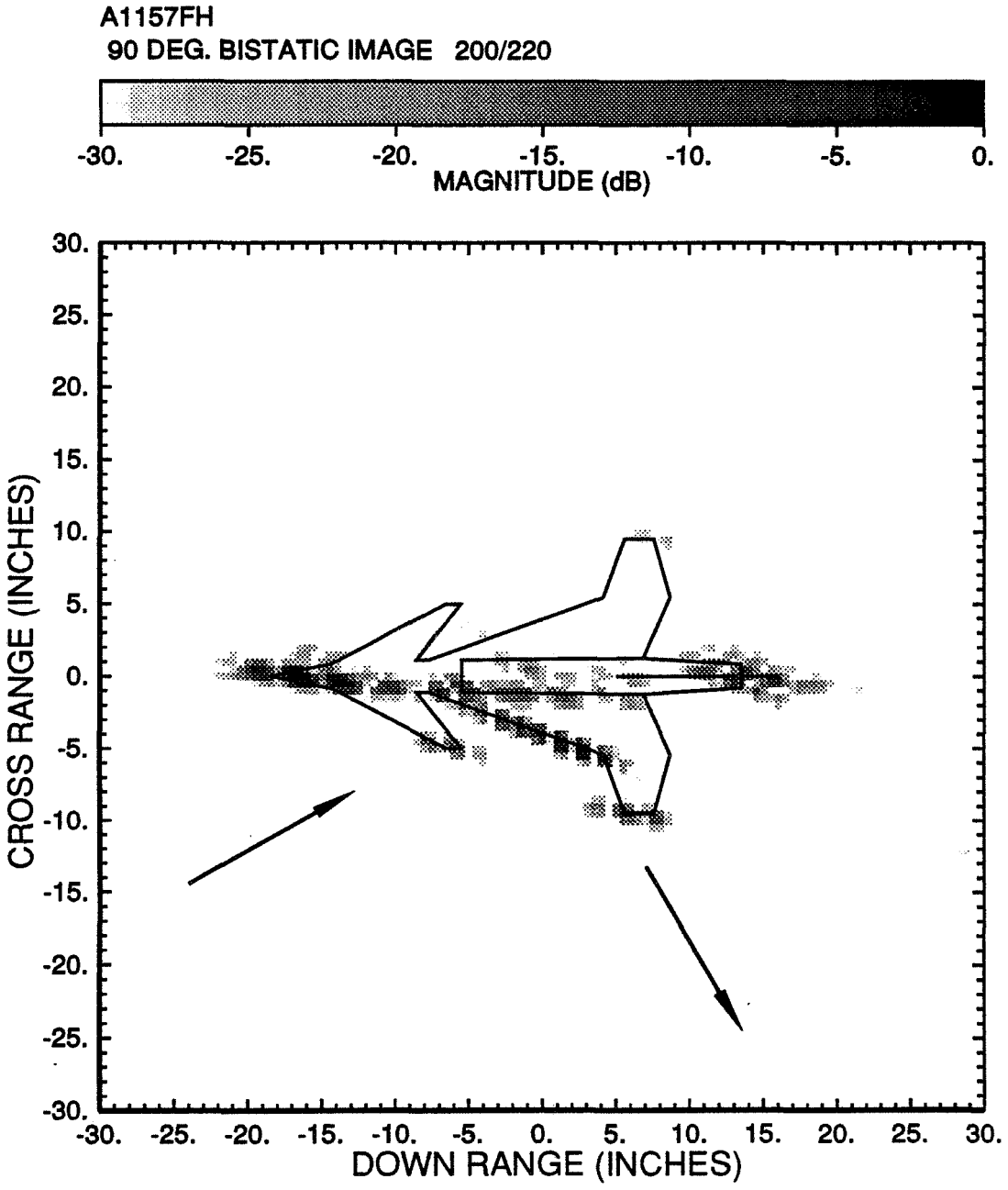

Figure 3.22: Bistatic ISAR image of the model aircraft. (90° bistatic angle, $\theta = 210° \pm 10°$).

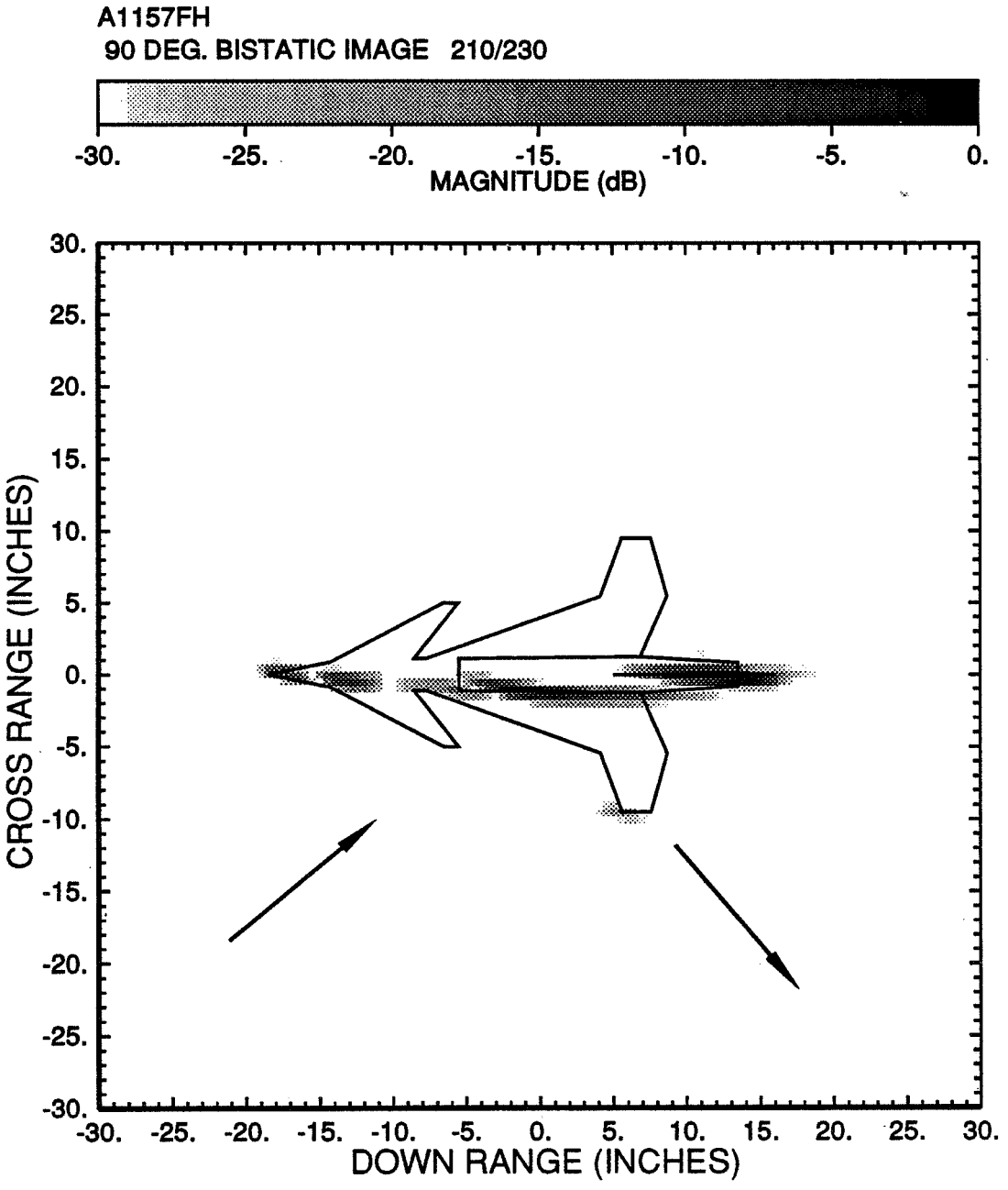

Figure 3.23: Bistatic ISAR image of the model aircraft. (90° bistatic angle, $\theta = 220° \pm 10°$).

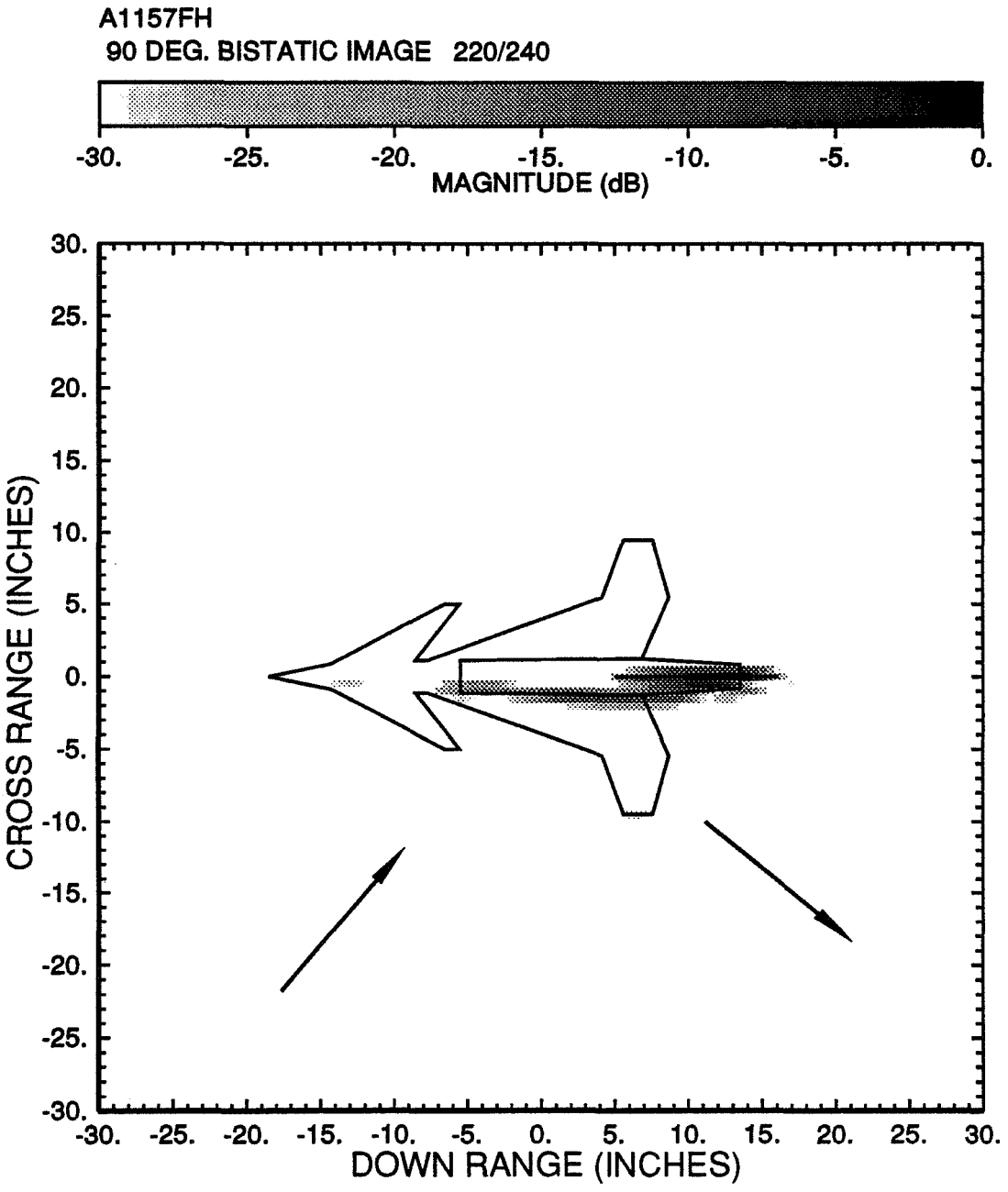

Figure 3.24: Bistatic ISAR image of the model aircraft. (90° bistatic angle, $\theta = 230° \pm 10°$).

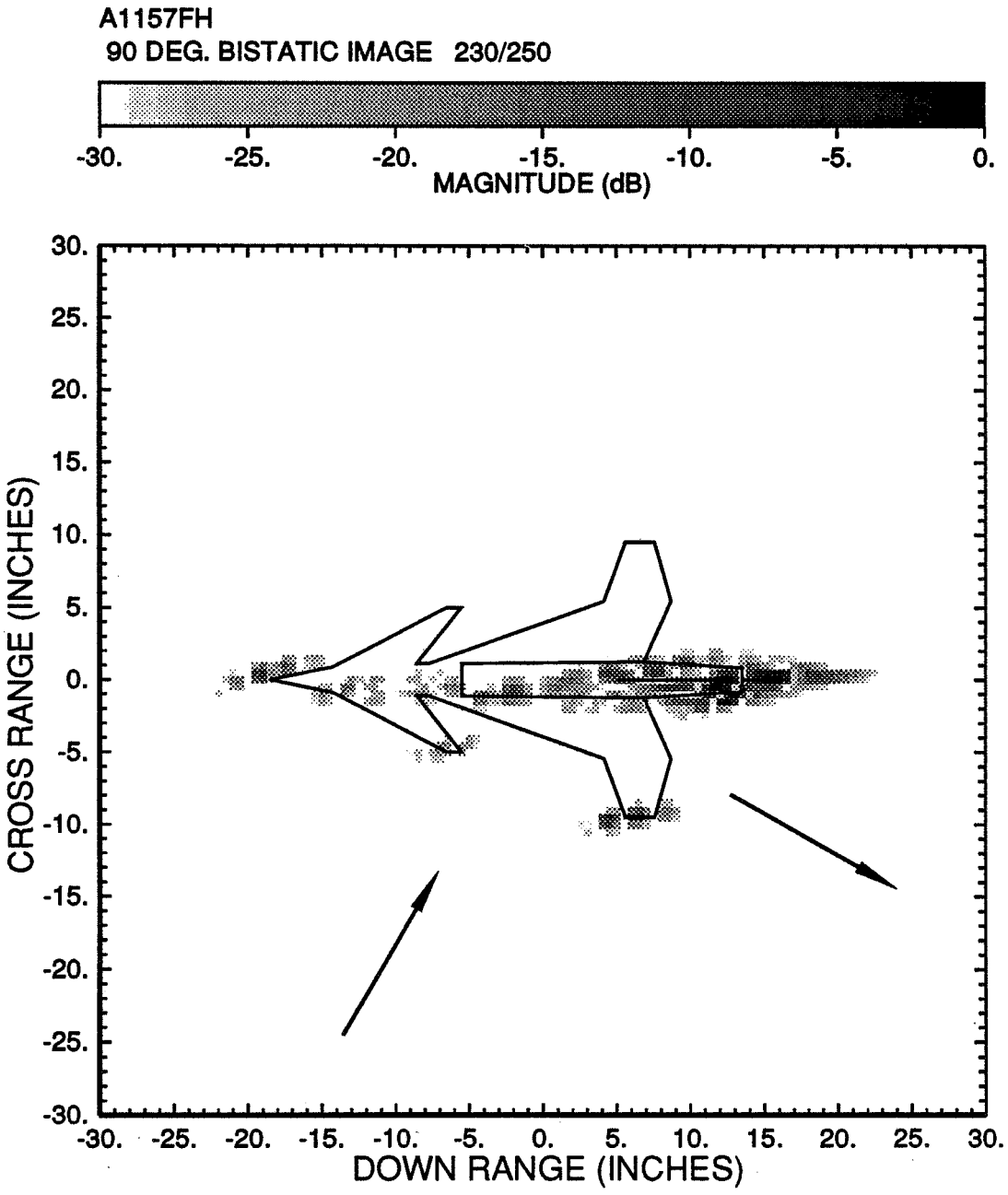

Figure 3.25: Bistatic ISAR image of the model aircraft. (90° bistatic angle, $\theta = 240° \pm 10°$).

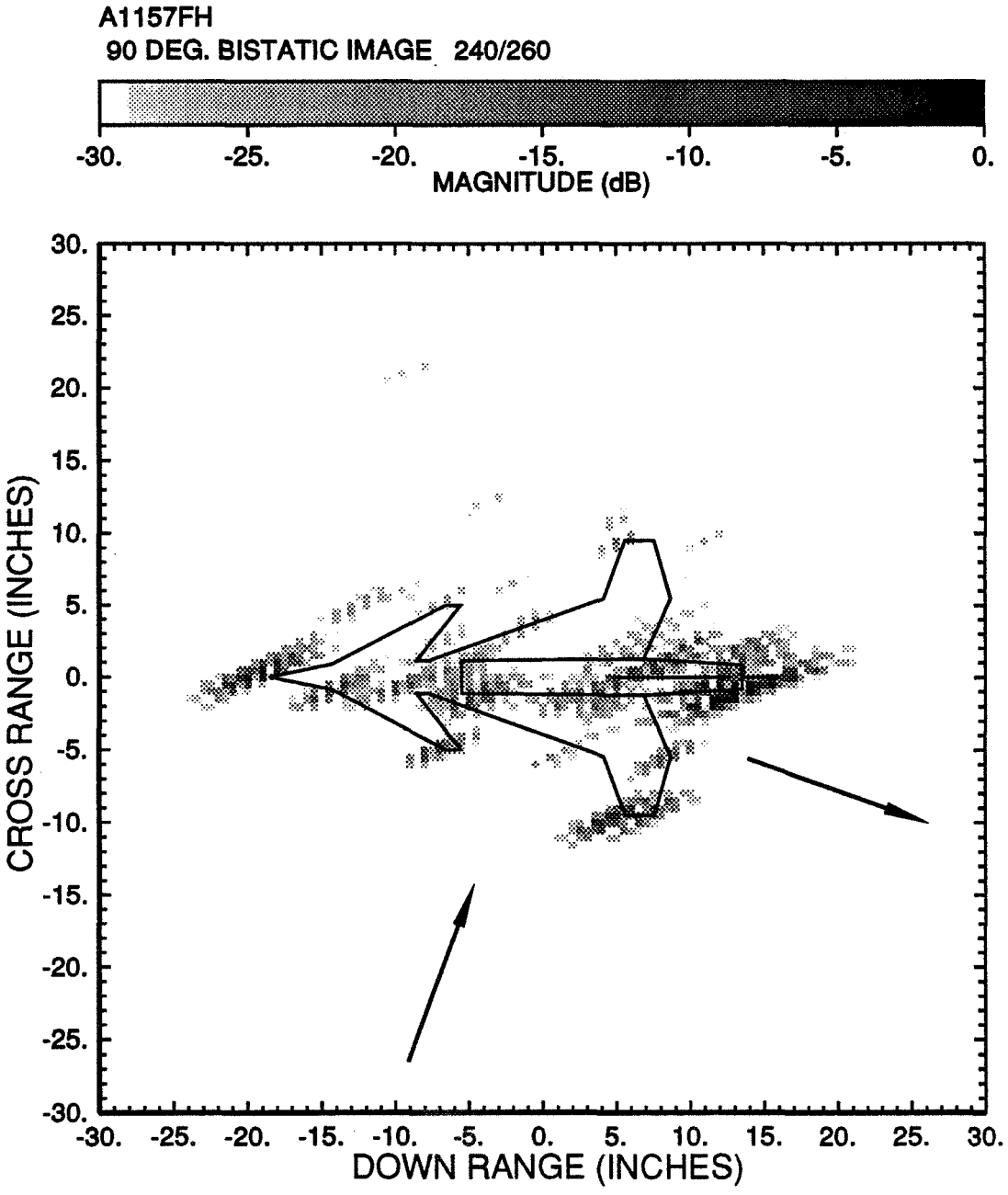

Figure 3.26: Bistatic ISAR image of the model aircraft. (90° bistatic angle, $\theta = 250° \pm 10°$).

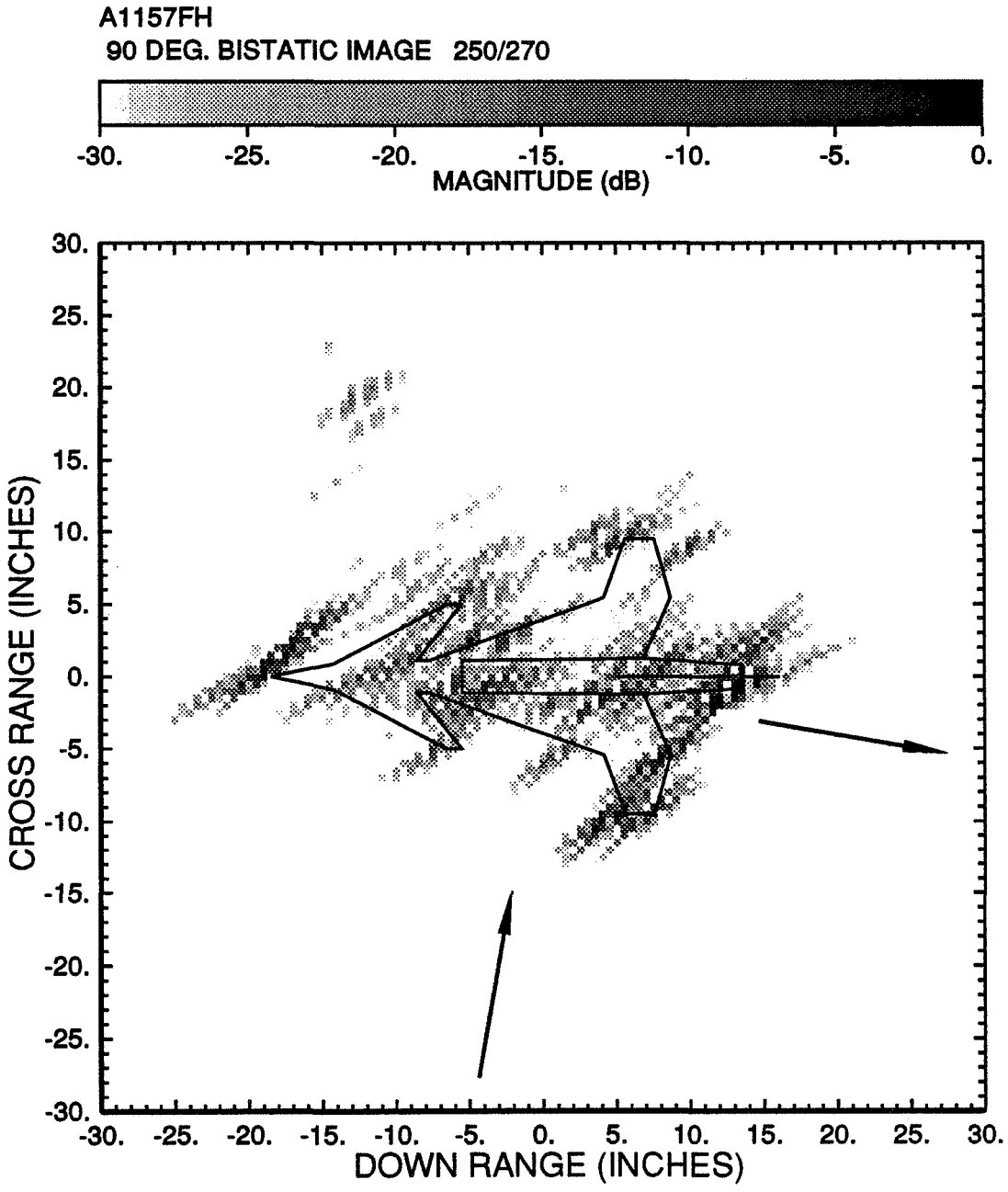

Figure 3.27: Bistatic ISAR image of the model aircraft. (90° bistatic angle, $\theta = 260° \pm 10°$).

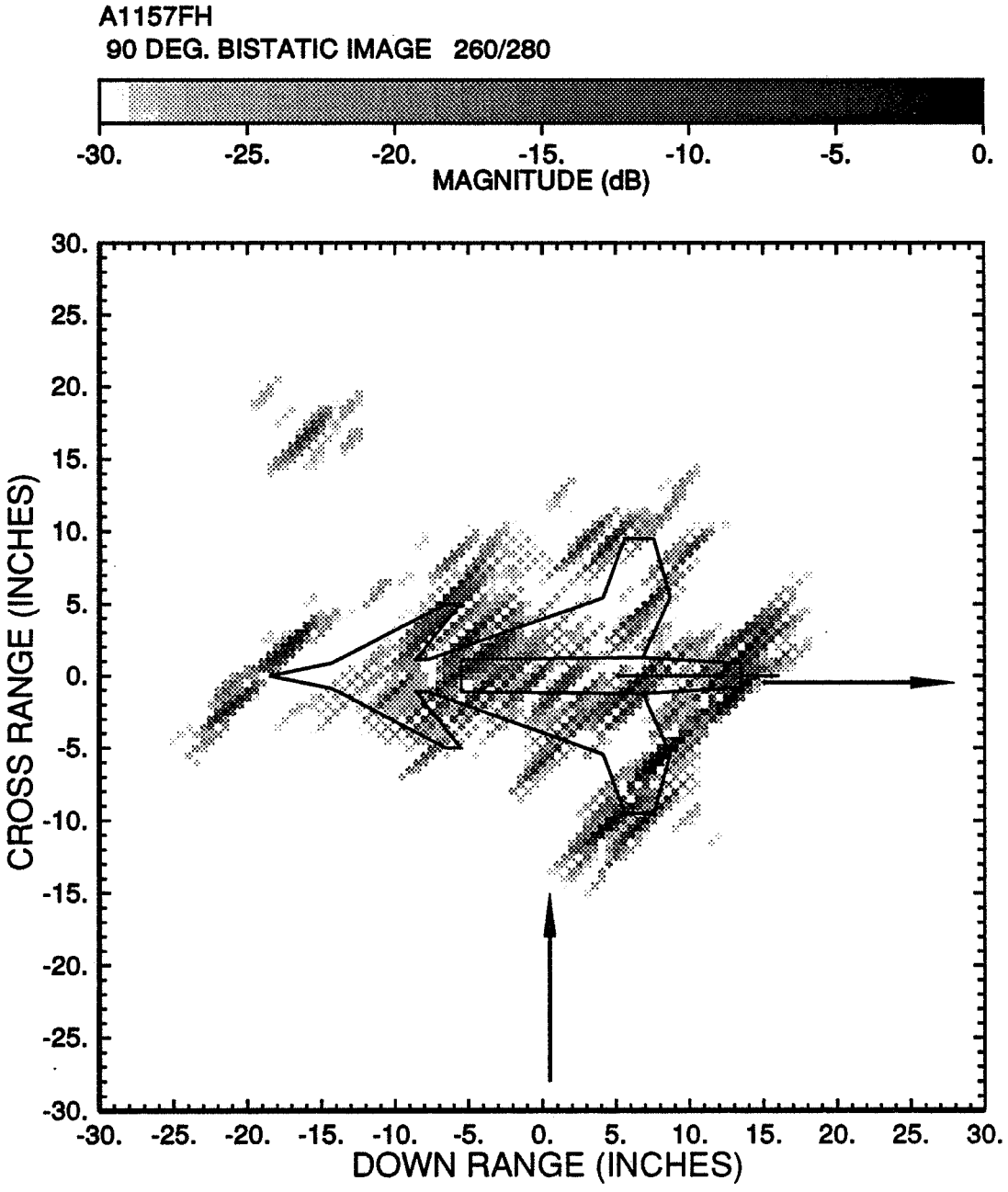

Figure 3.28: Bistatic ISAR image of the model aircraft. (90° bistatic angle, $\theta = 270° \pm 10°$).

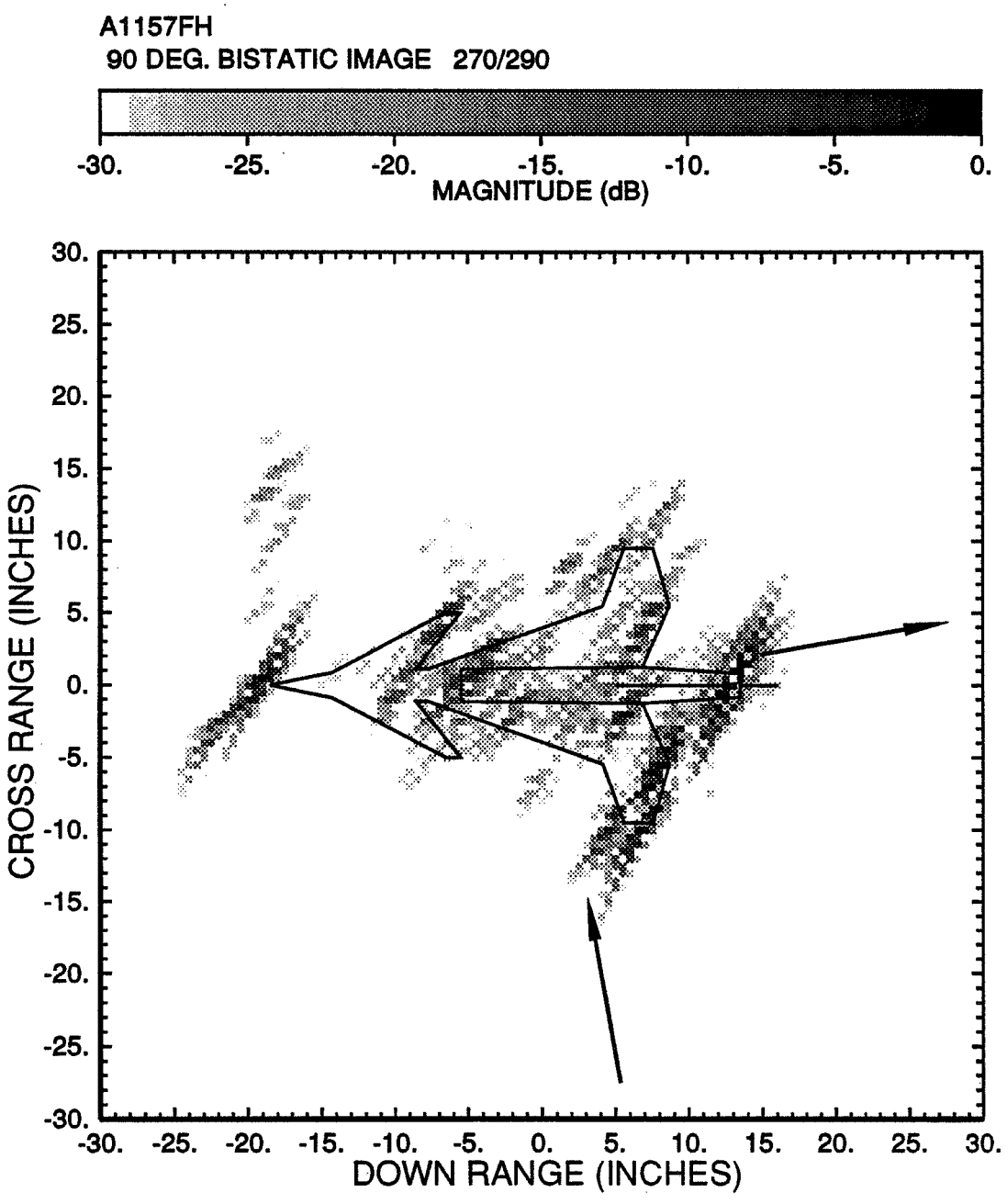

Figure 3.29: Bistatic ISAR image of the model aircraft. (90° bistatic angle, $\theta = 280° \pm 10°$).

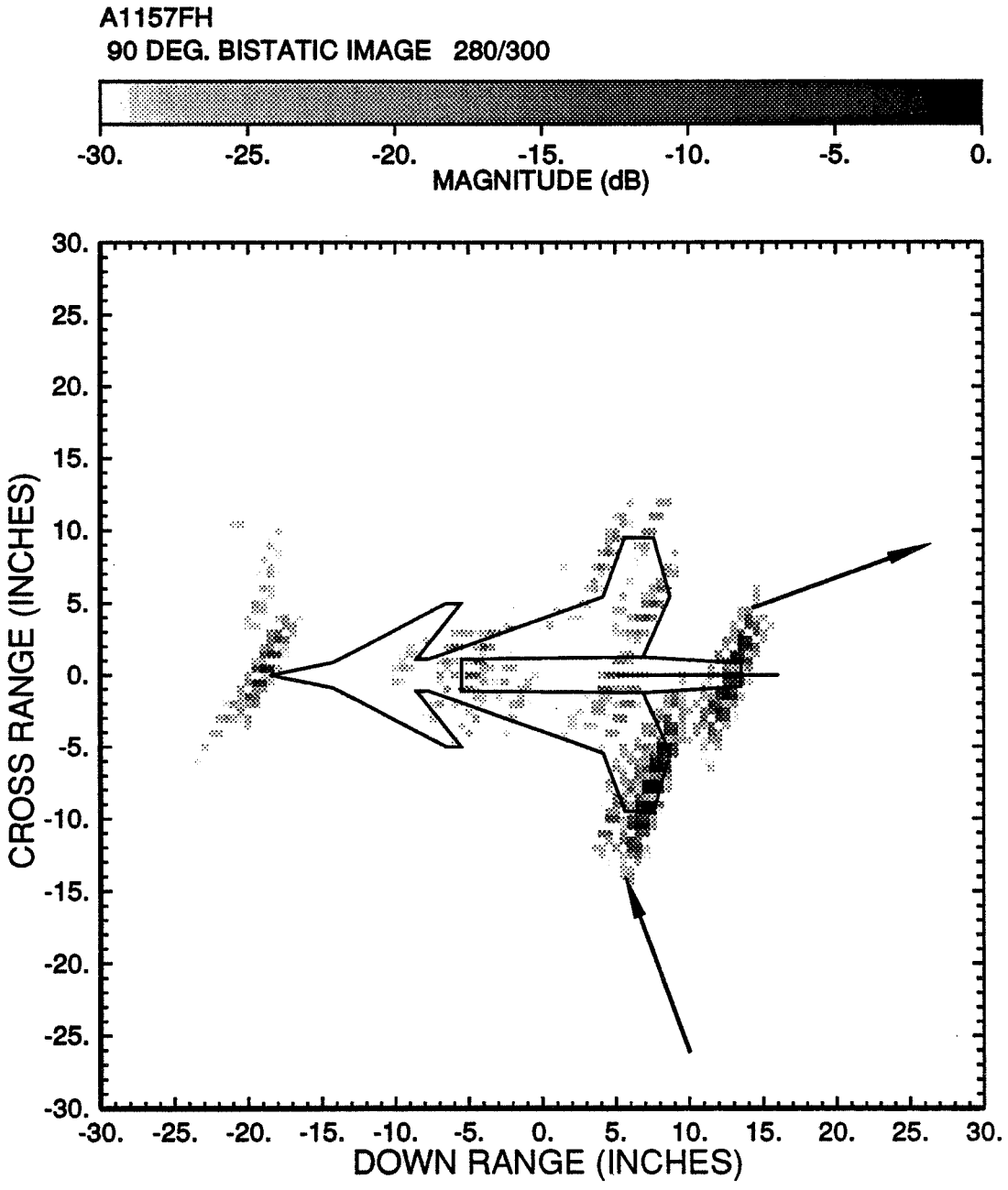

Figure 3.30: Bistatic ISAR image of the model aircraft. (90° bistatic angle, $\theta = 290° \pm 10°$).

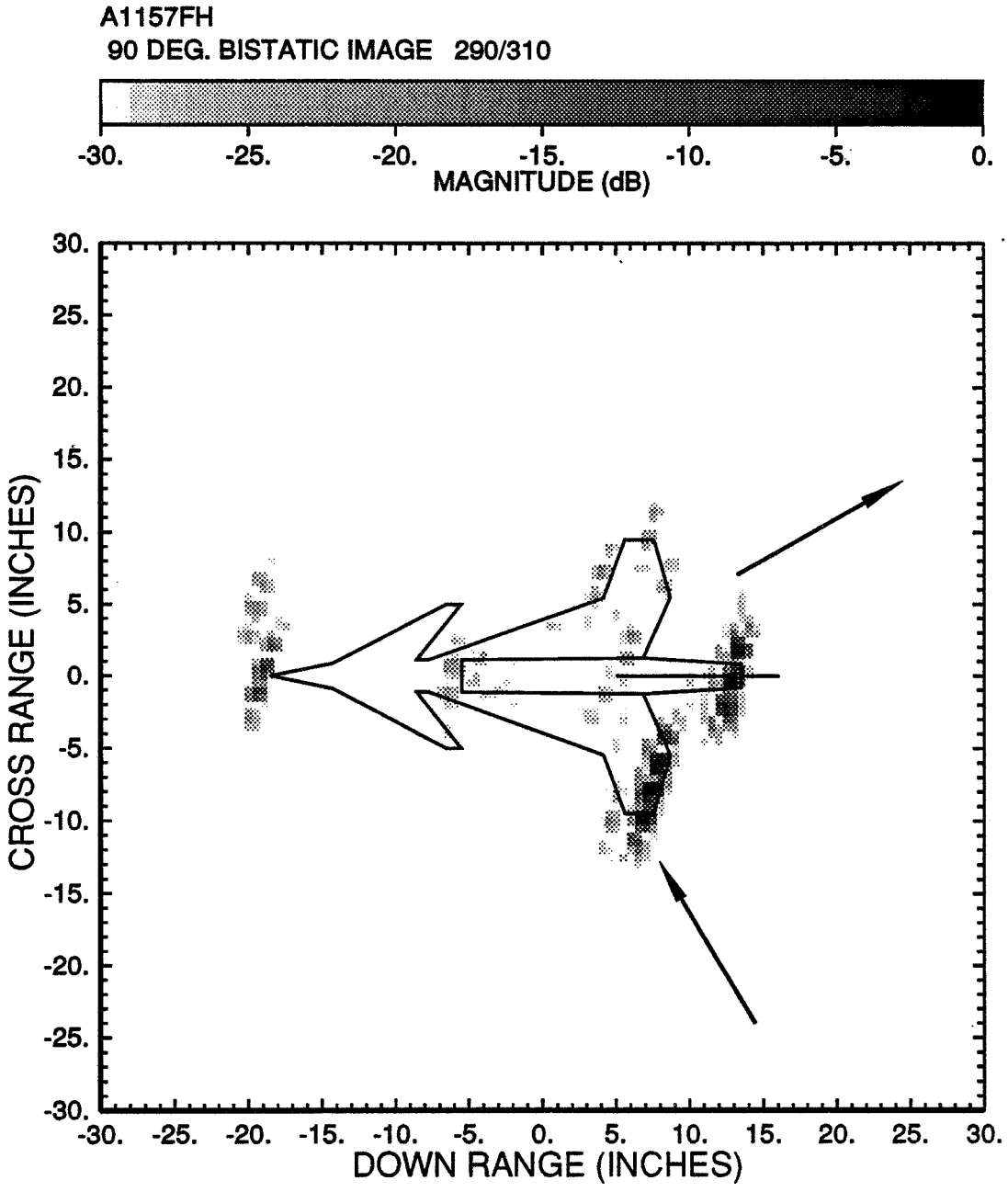

Figure 3.31: Bistatic ISAR image of the model aircraft. (90° bistatic angle, $\theta = 300° \pm 10°$).

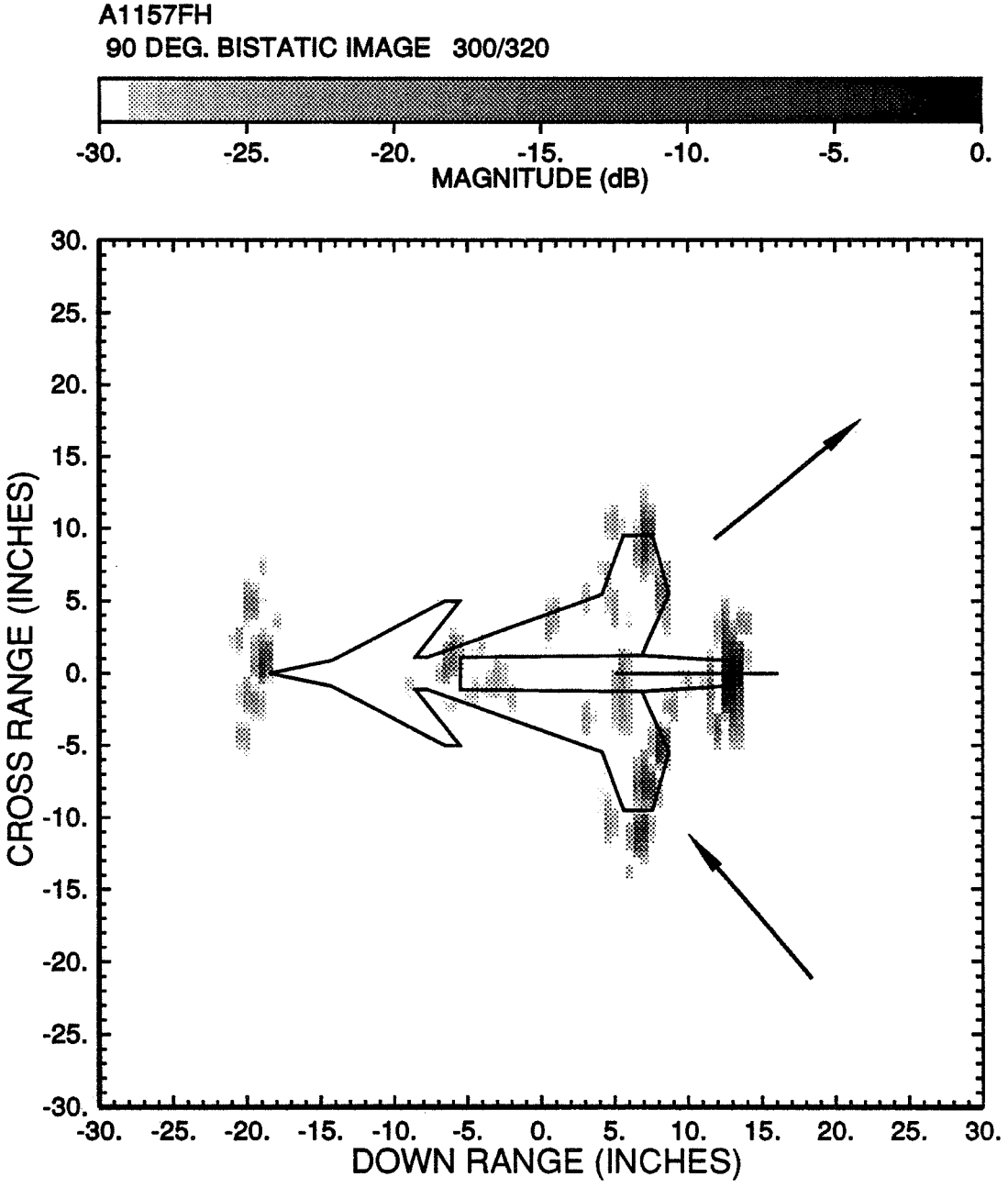

Figure 3.32: Bistatic ISAR image of the model aircraft. (90° bistatic angle, $\theta = 310° \pm 10°$).

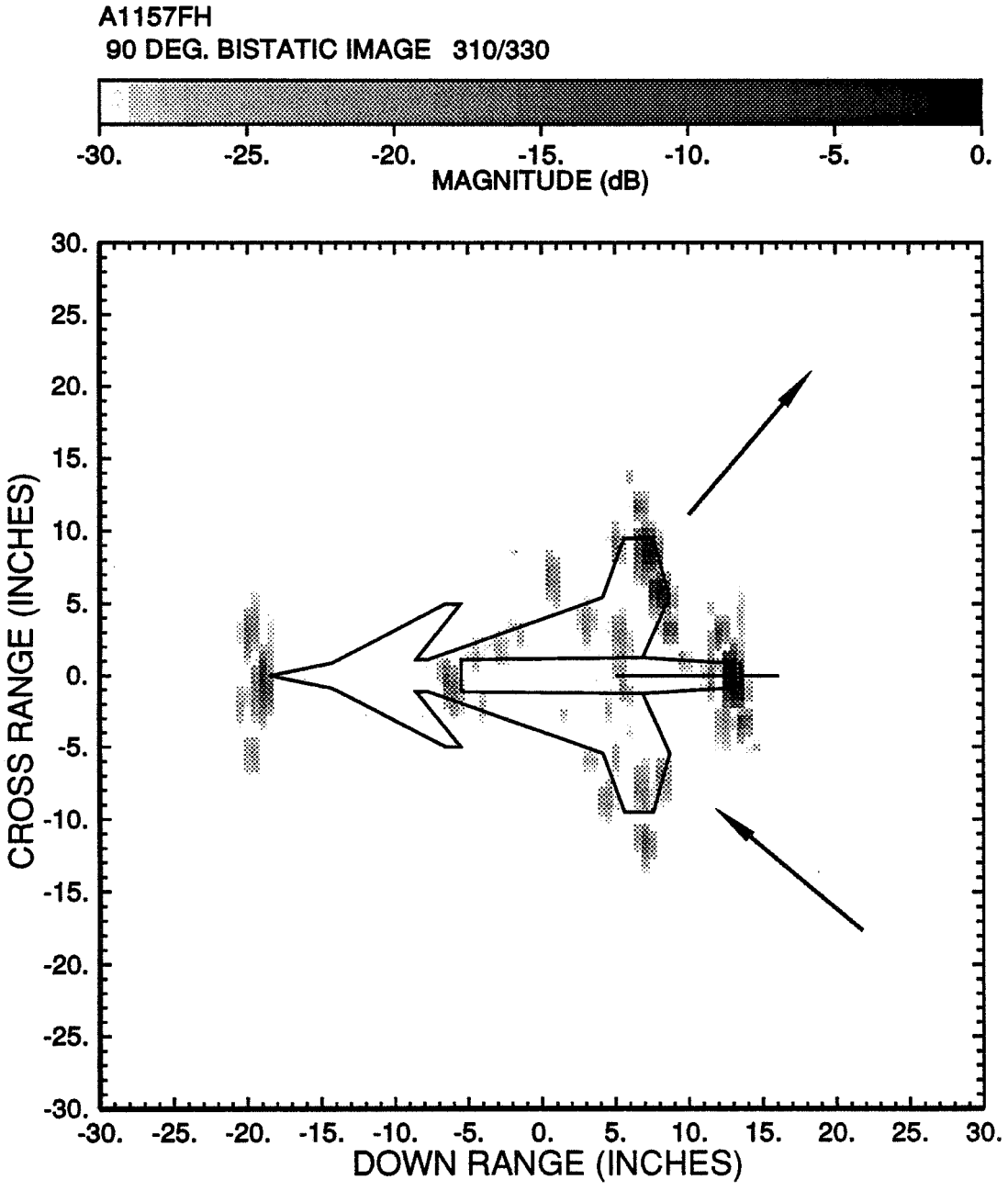

Figure 3.33: Bistatic ISAR image of the model aircraft. (90° bistatic angle, $\theta = 320° \pm 10°$).

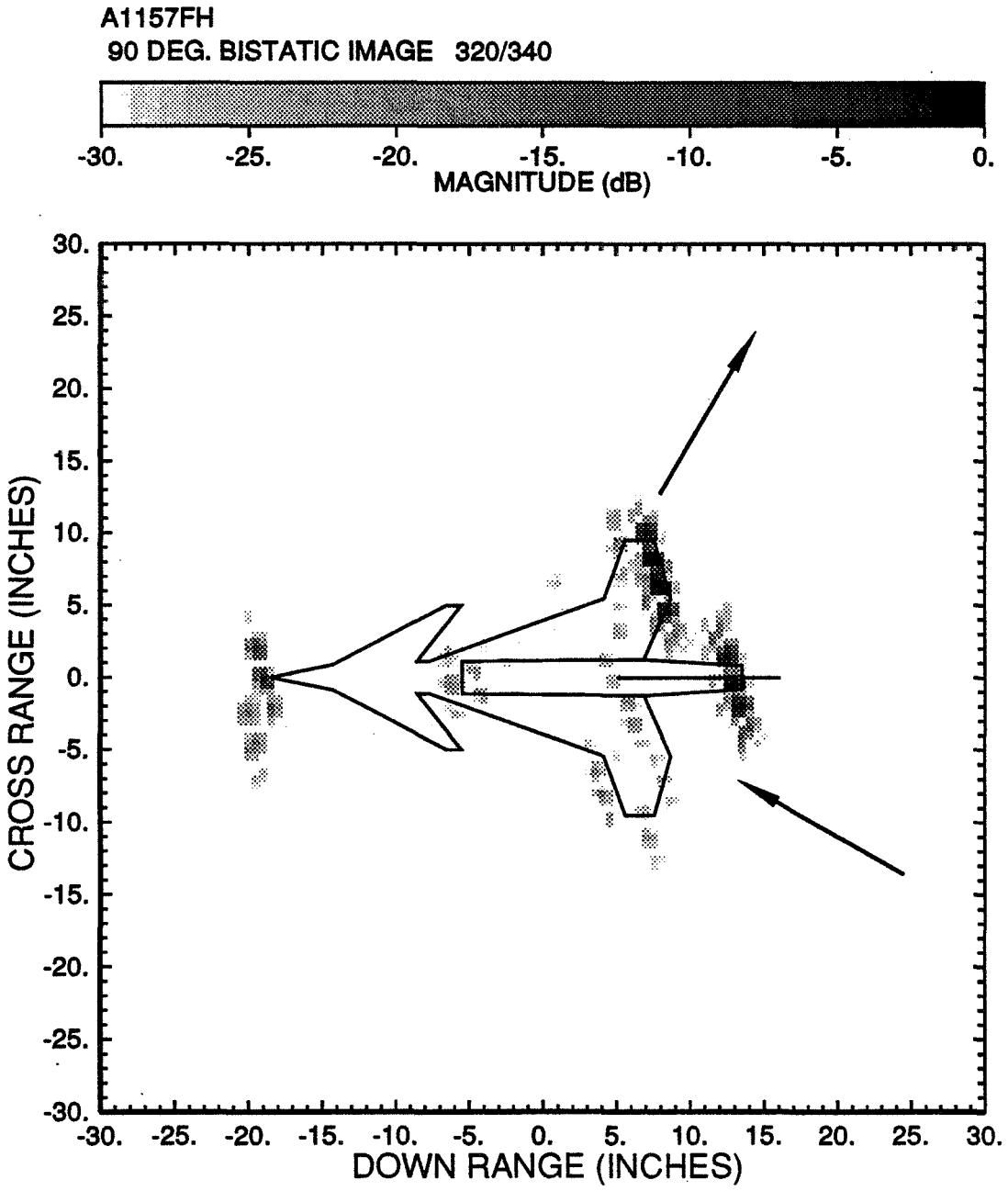

Figure 3.34: Bistatic ISAR image of the model aircraft. (90° bistatic angle, $\theta = 330° \pm 10°$).

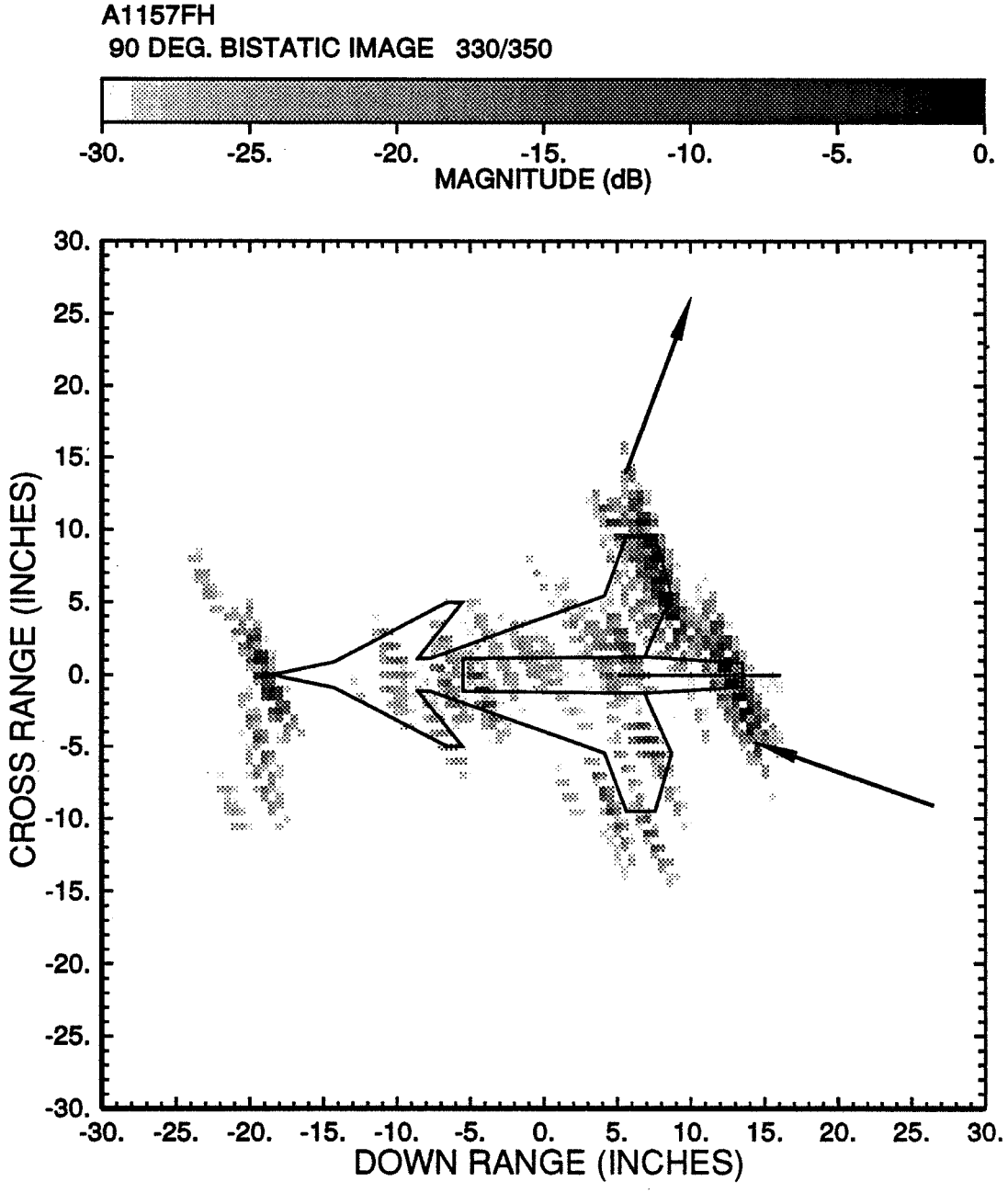

Figure 3.35: Bistatic ISAR image of the model aircraft. (90° bistatic angle, $\theta = 340° \pm 10°$).

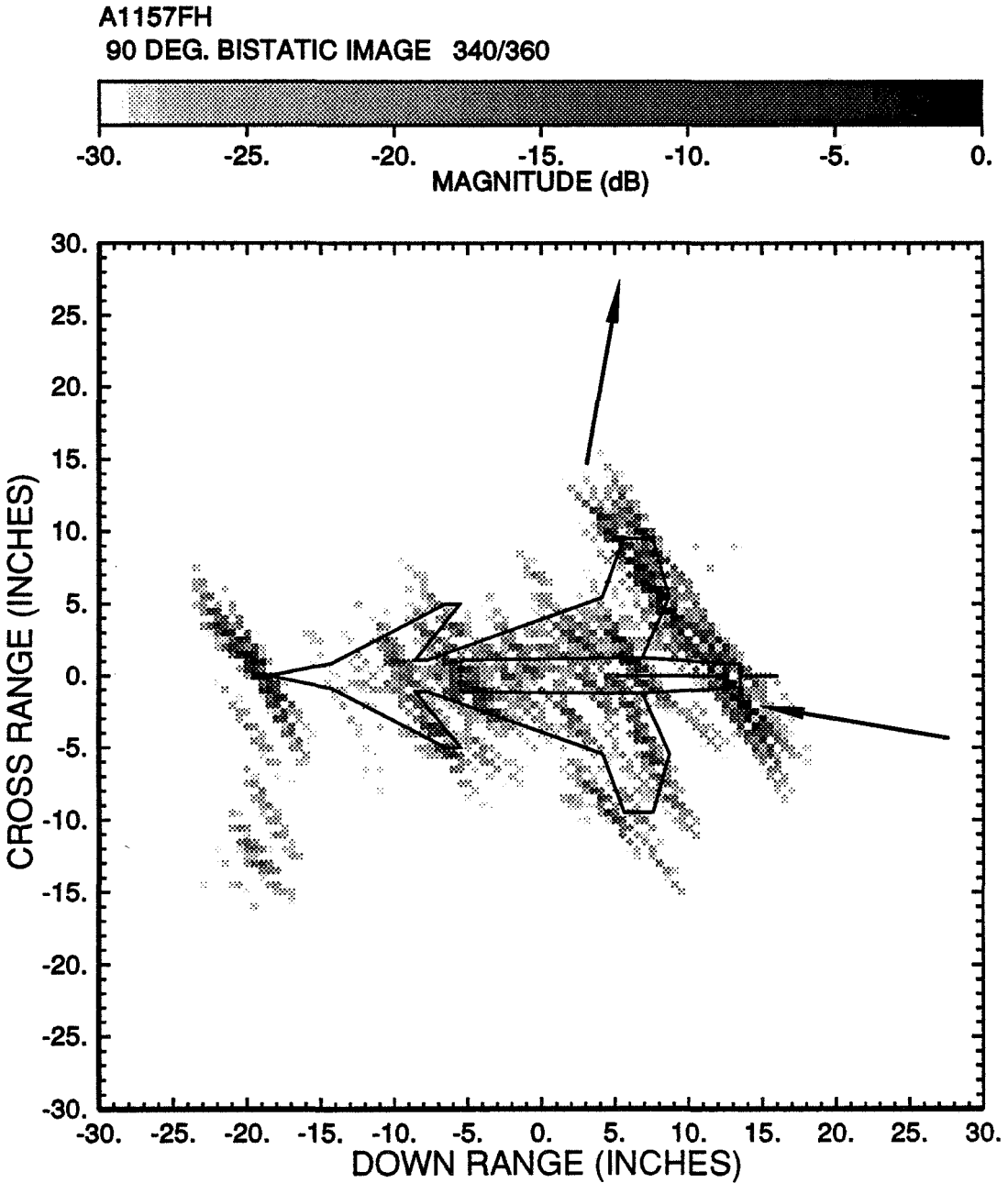

Figure 3.36: Bistatic ISAR image of the model aircraft. (90° bistatic angle, $\theta = 350° \pm 10°$).

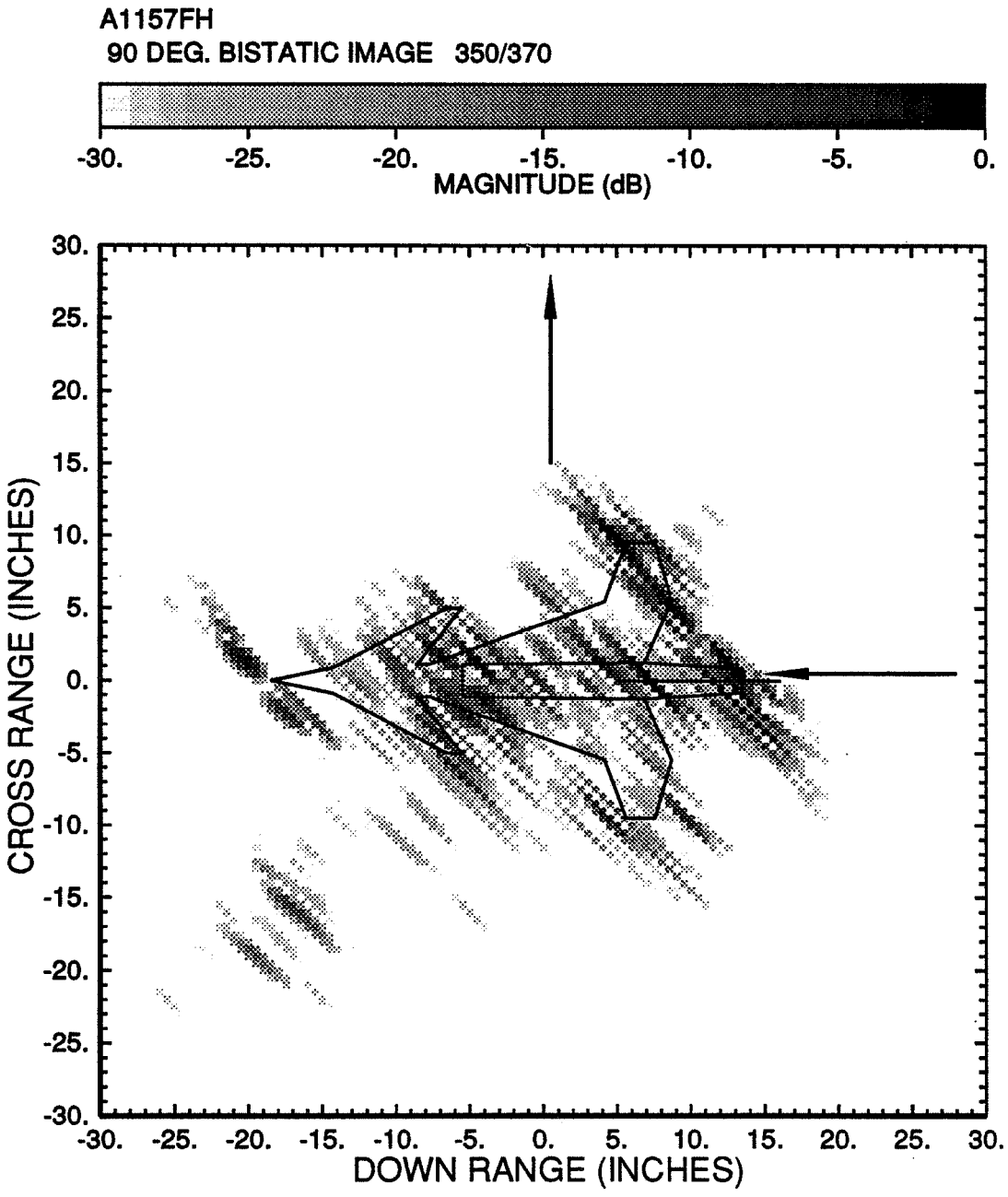

Figure 3.37: Bistatic ISAR image of the model aircraft. (90° bistatic angle, $\theta = 360° \pm 10°$).

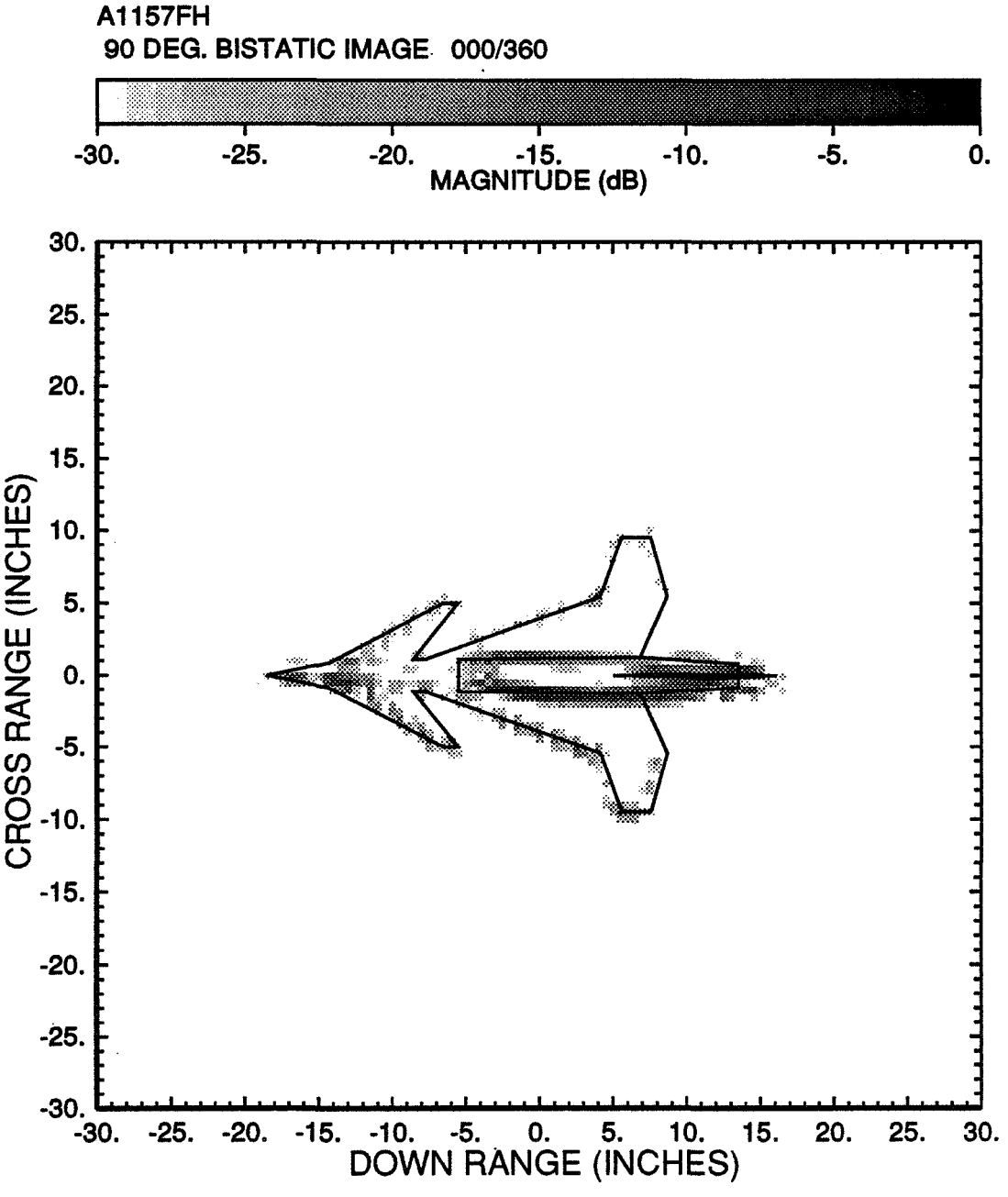

Figure 3.38: Bistatic ISAR image of the model aircraft. (complete 360°).

Chapter 4

Bistatic Images of the $32'' \times 19''$ Model Aircraft for 135° Bistatic Angle

This chapter summarizes the ISAR images of the model aircraft processed from the measured bistatic scattered fields for horizontal polarization. The receiving antenna was located 171″ west and 171″ north from the target as shown in Figure 1.1 and was in the near field of the target. Consequently, the bistatic angle was 135°. The bistatic ISAR images (135° bistatic angle) for mean incident angles from 10° to 360° with a 10° step are shown in Figures 4.1 to 4.36. The image for each mean incident angle was normalized with respect to its own maximum. Again, the simplified outline of the model aircraft is also shown in these images so that one can identify the scattering centers. The complete 360° image is shown in Figure 4.37.

Note that a metal pylon was used as the target support in this measurement. It has been said that for wide bistatic scattering angle, the metal pylon is not a good target support because its side faces may create strong bistatic scattered fields which will interfere with the desired target bistatic scattered fields. With this concern in mind, a Styrofoam column was also used as the target support for the 135° bistatic scattering measurement. The resulting images are in good agreement with the ones when a metal pylon was used as the target support. However, one should still be

careful when using the metal pylon as the target support for large bistatic angle scattering measurement.

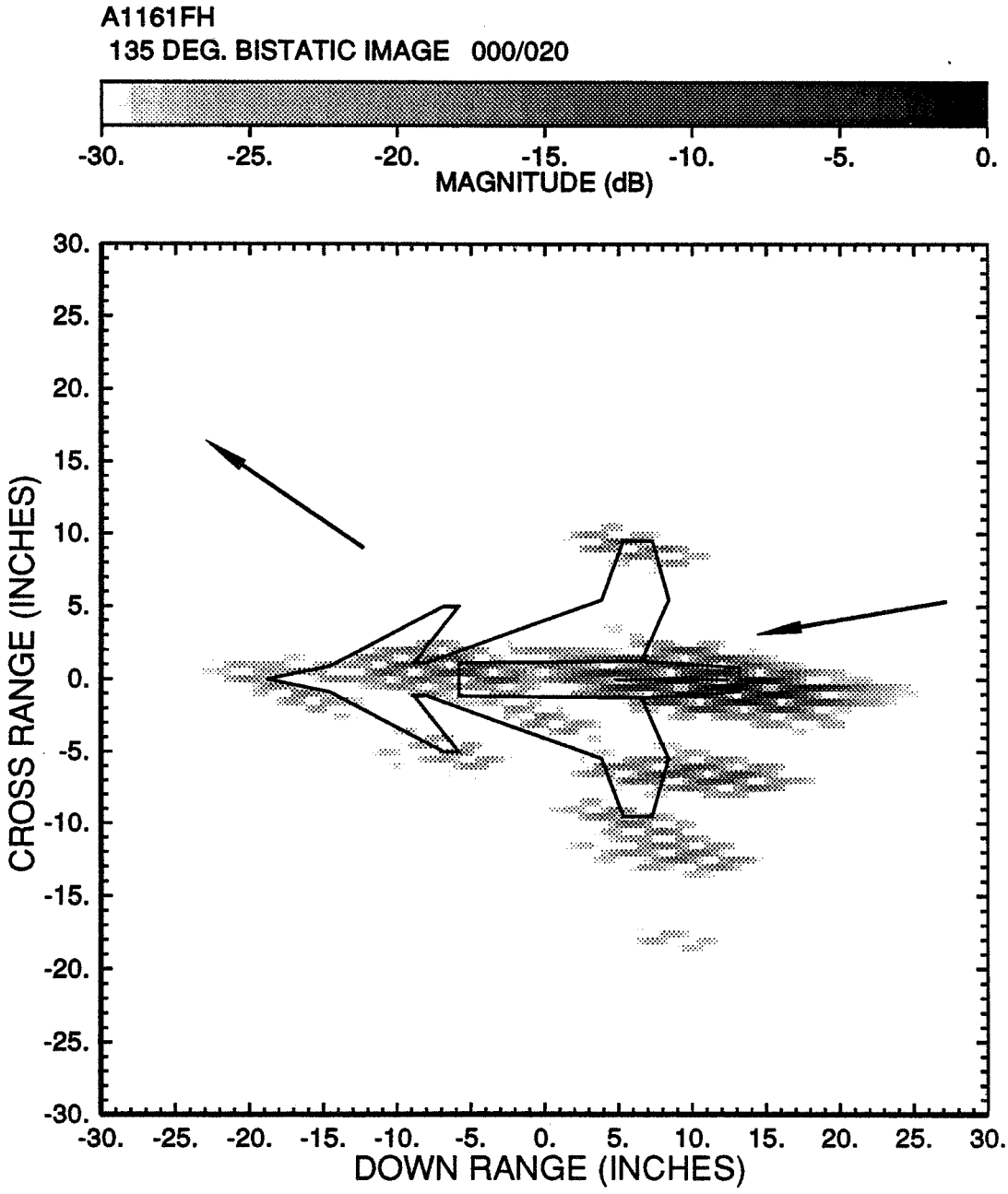

Figure 4.1: Bistatic ISAR image of the model aircraft. (135° bistatic angle, $\theta = 10° \pm 10°$).

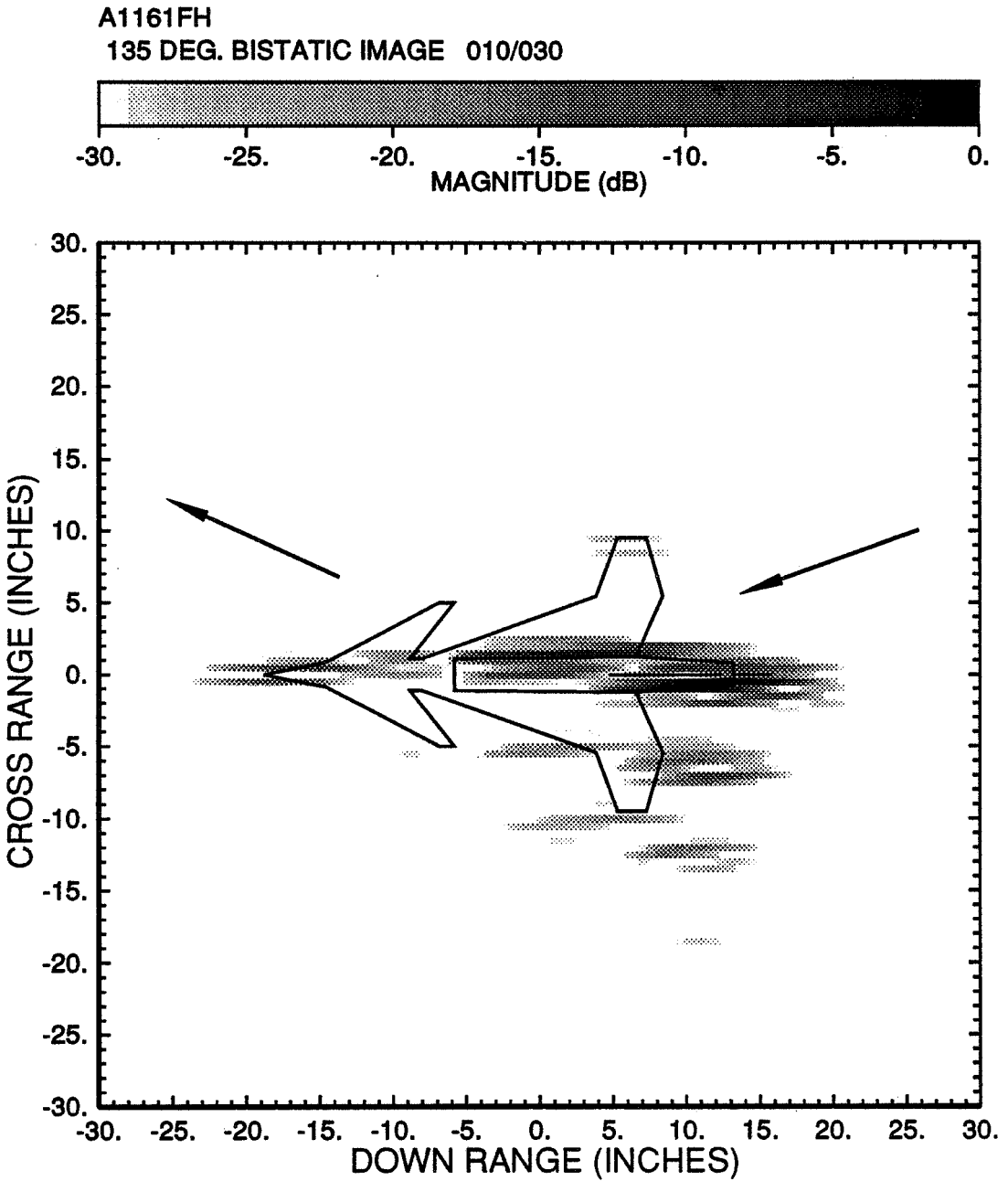

Figure 4.2: Bistatic ISAR image of the model aircraft. (135° bistatic angle, $\theta = 20° \pm 10°$).

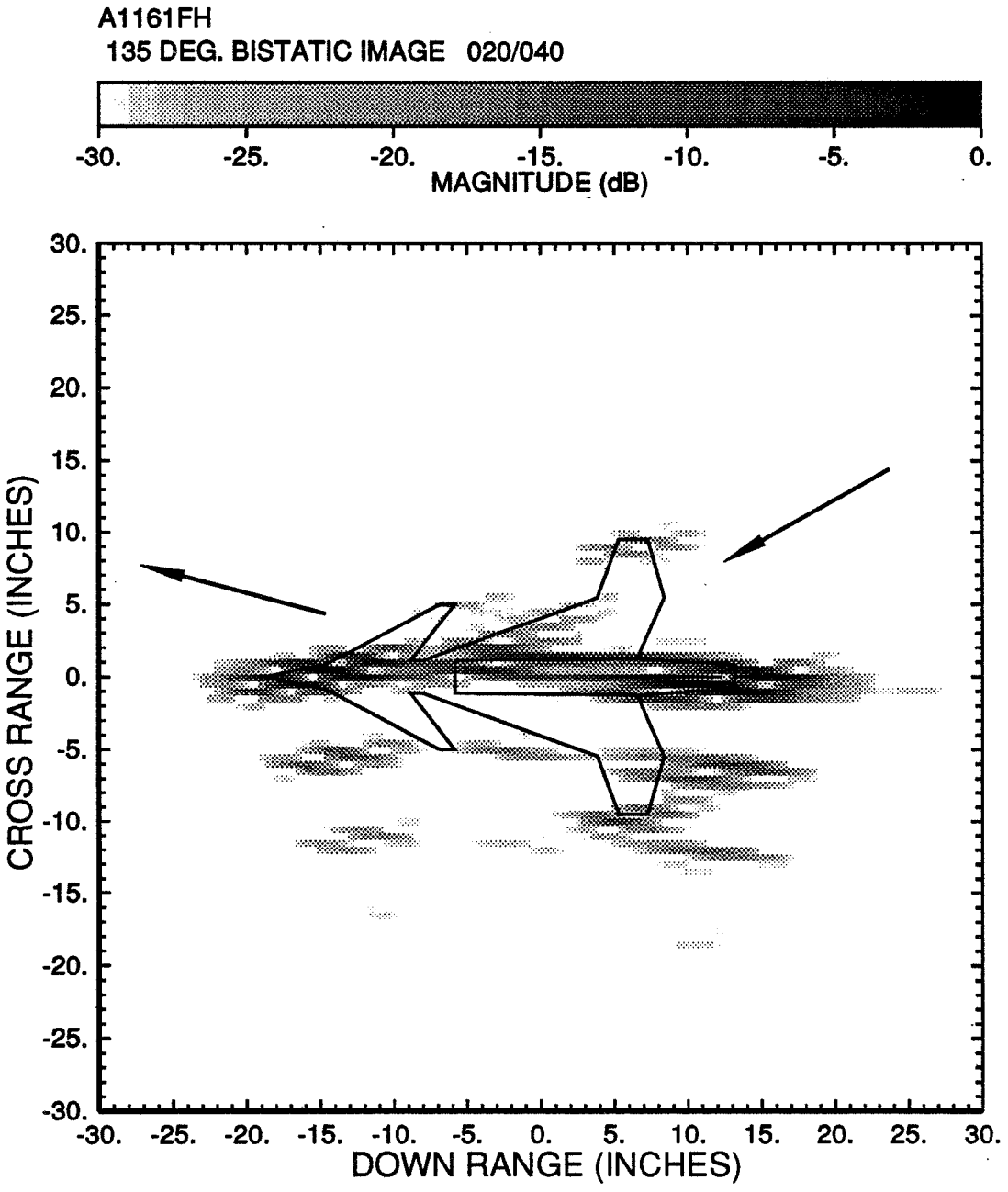

Figure 4.3: Bistatic ISAR image of the model aircraft. (135° bistatic angle, $\theta = 30° \pm 10°$).

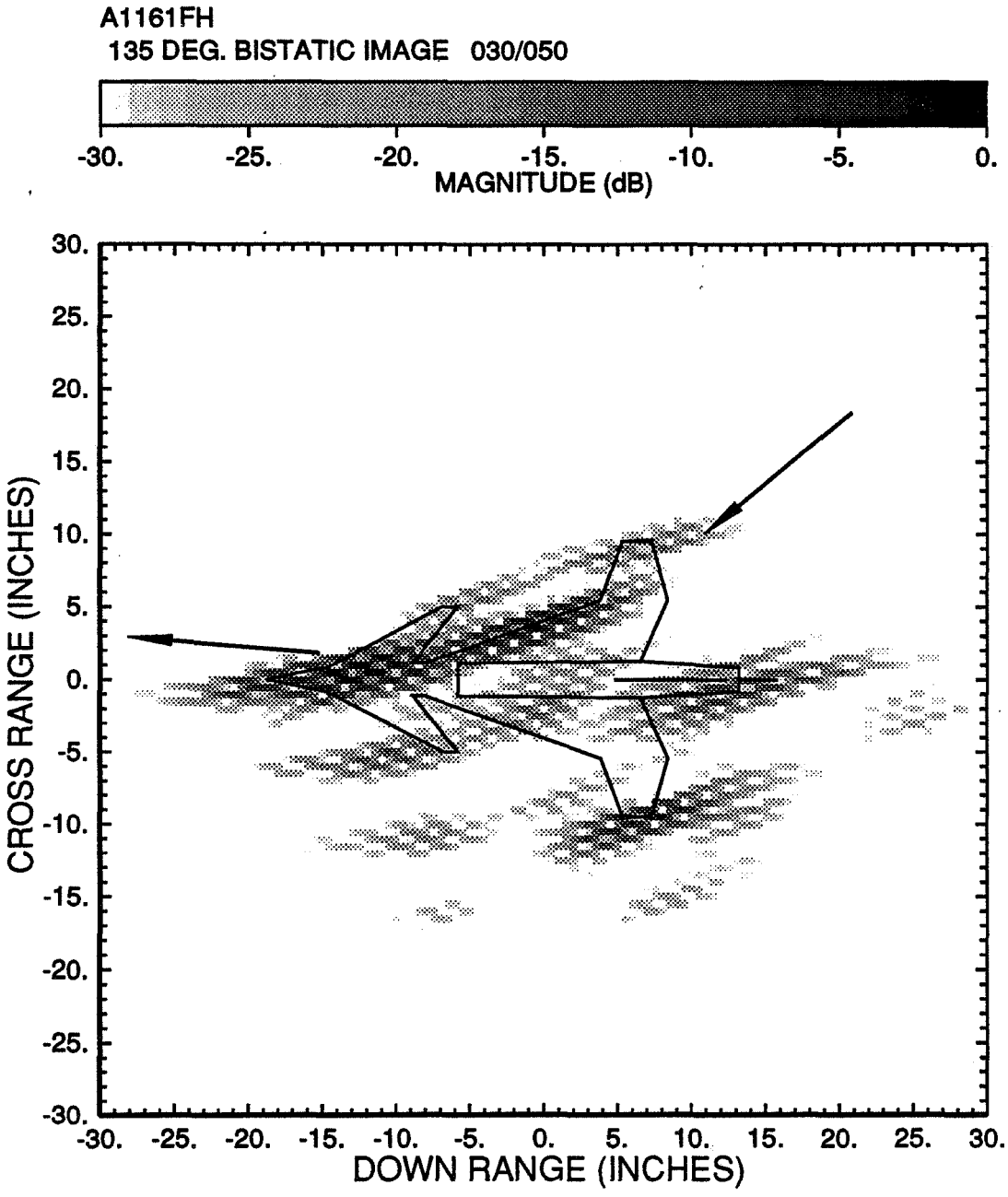

Figure 4.4: Bistatic ISAR image of the model aircraft. (135° bistatic angle, $\theta = 40° \pm 10°$).

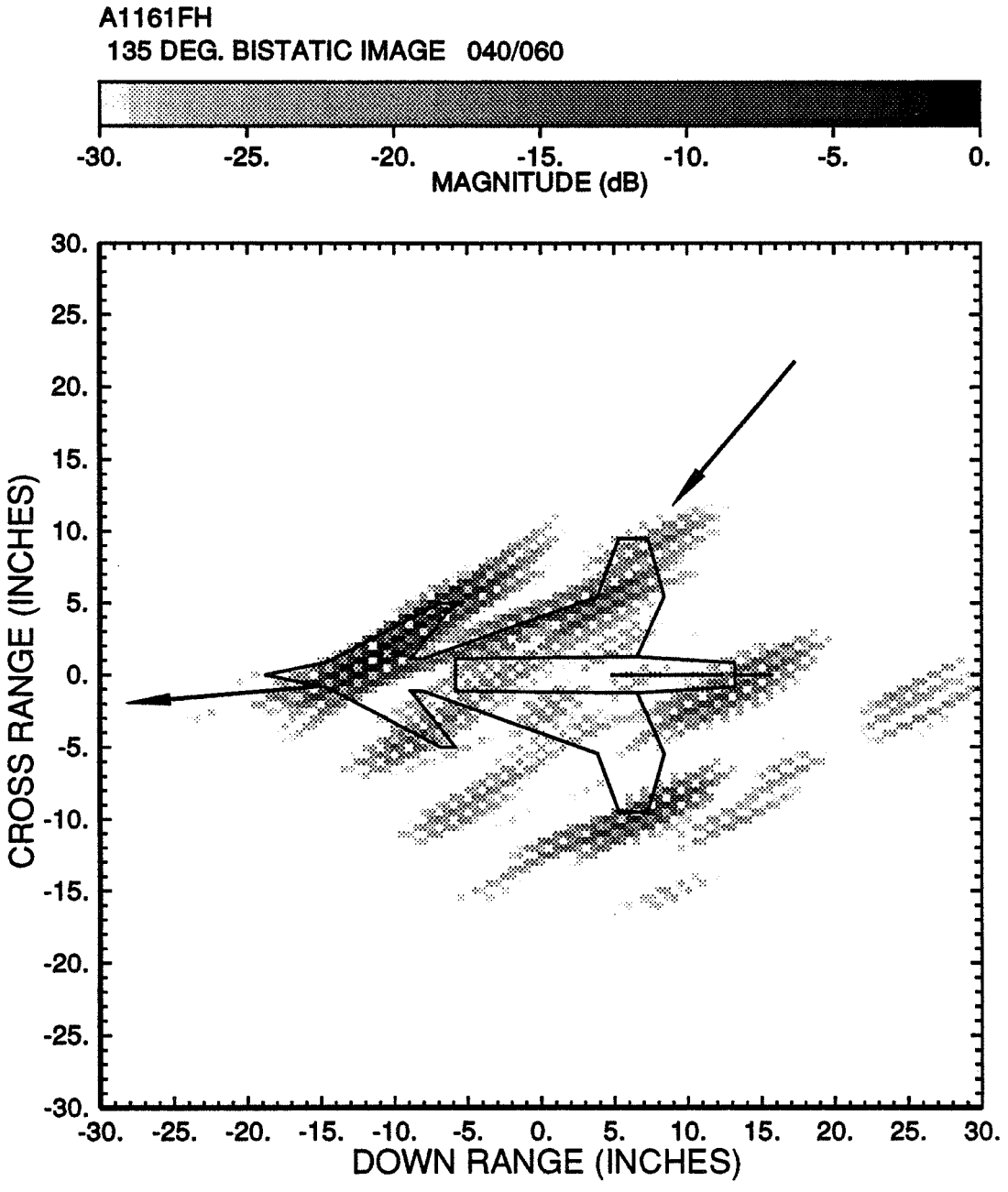

Figure 4.5: Bistatic ISAR image of the model aircraft. (135° bistatic angle, $\theta = 50° \pm 10°$).

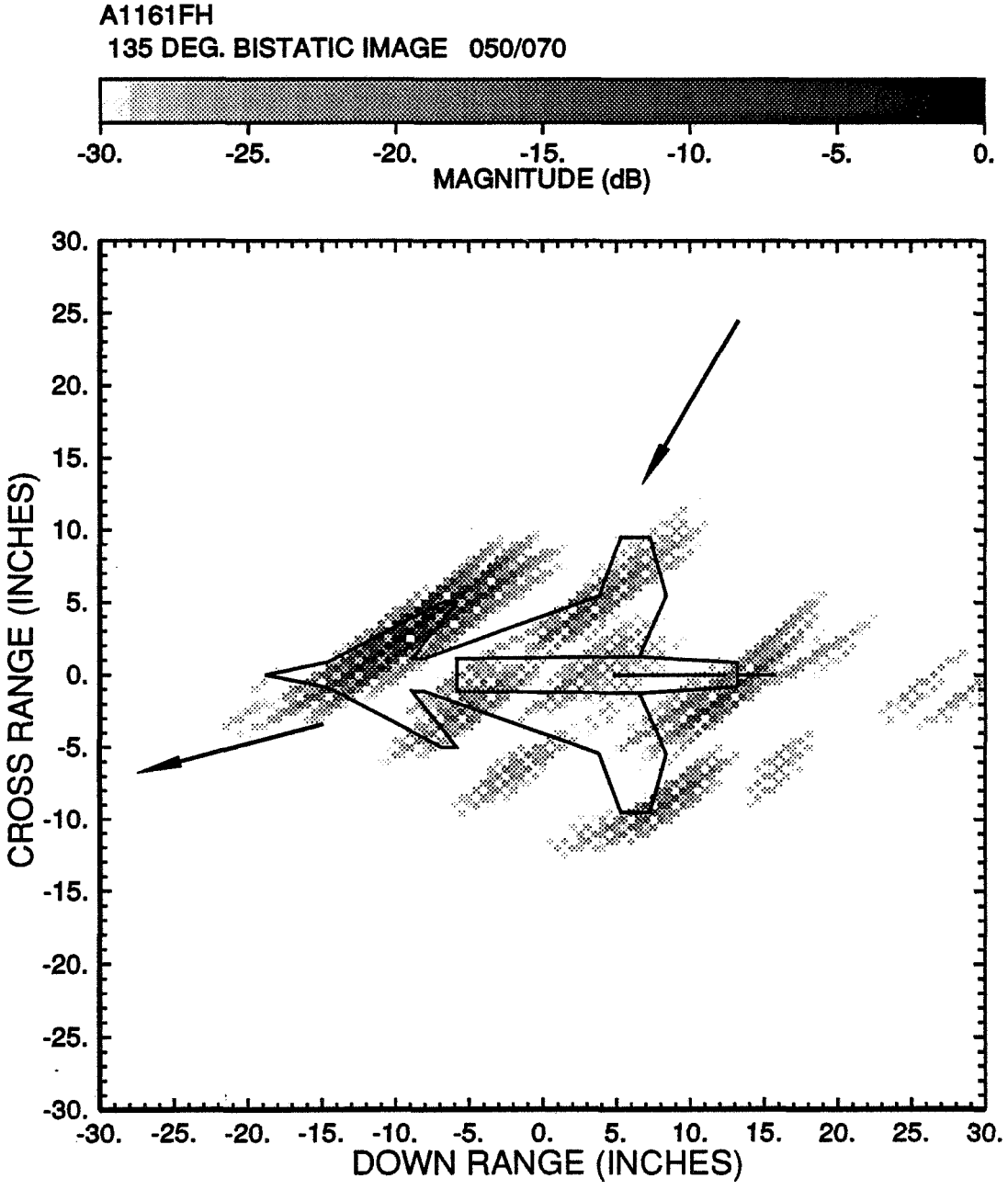

Figure 4.6: Bistatic ISAR image of the model aircraft. (135° bistatic angle, $\theta = 60° \pm 10°$).

C-2

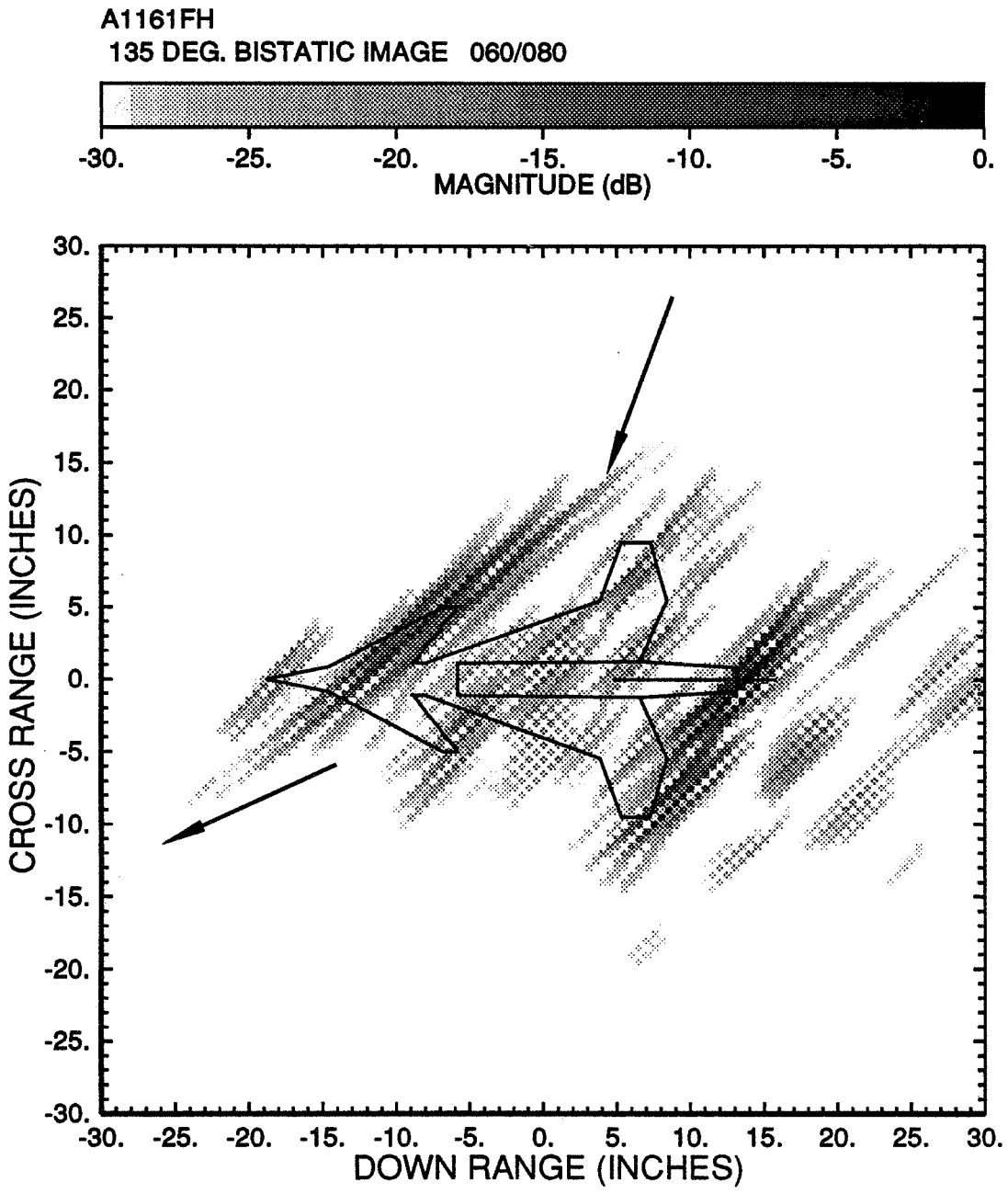

Figure 4.7: Bistatic ISAR image of the model aircraft. (135° bistatic angle, $\theta = 70° \pm 10°$).

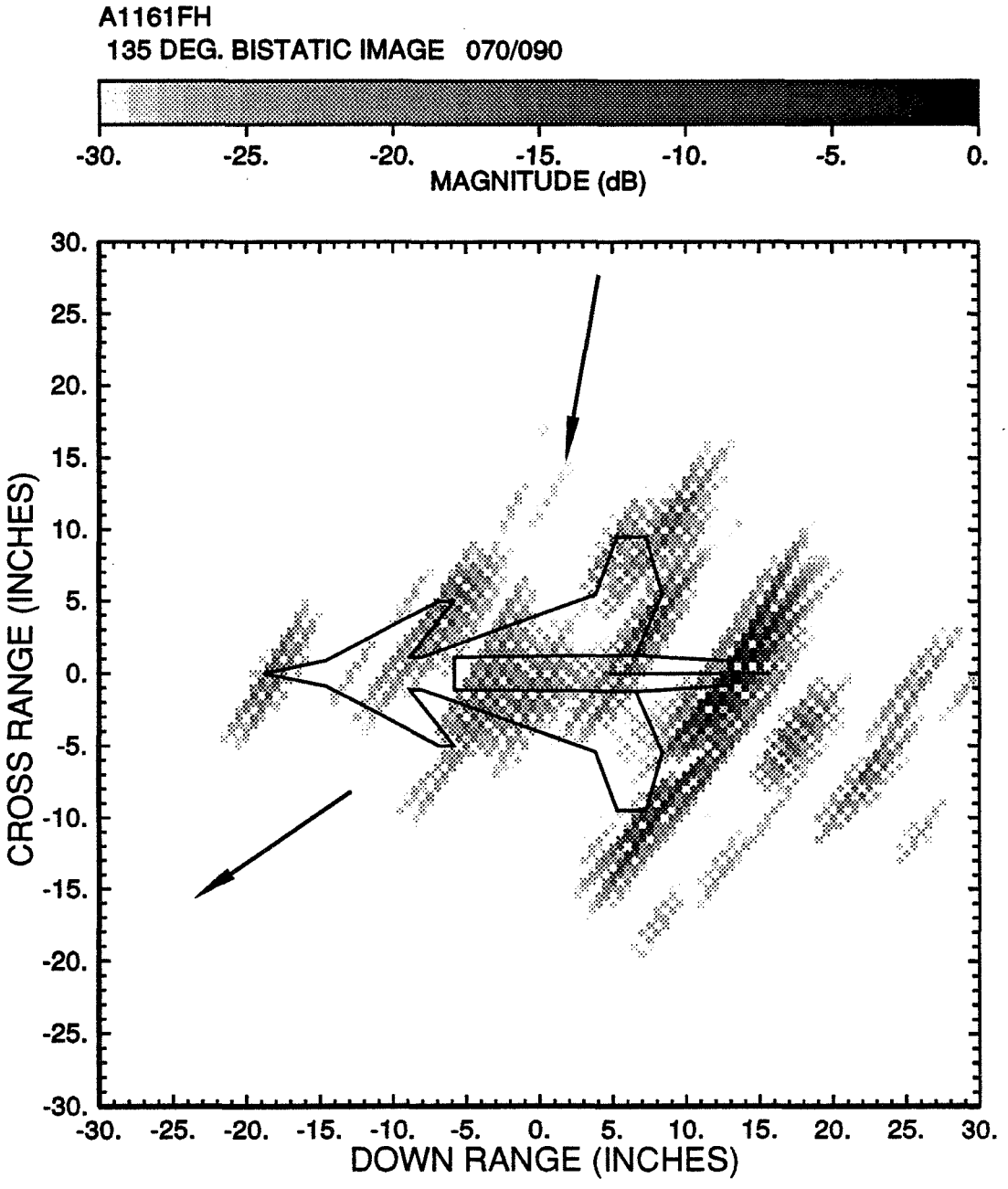

Figure 4.8: Bistatic ISAR image of the model aircraft. (135° bistatic angle, $\theta = 80° \pm 10°$).

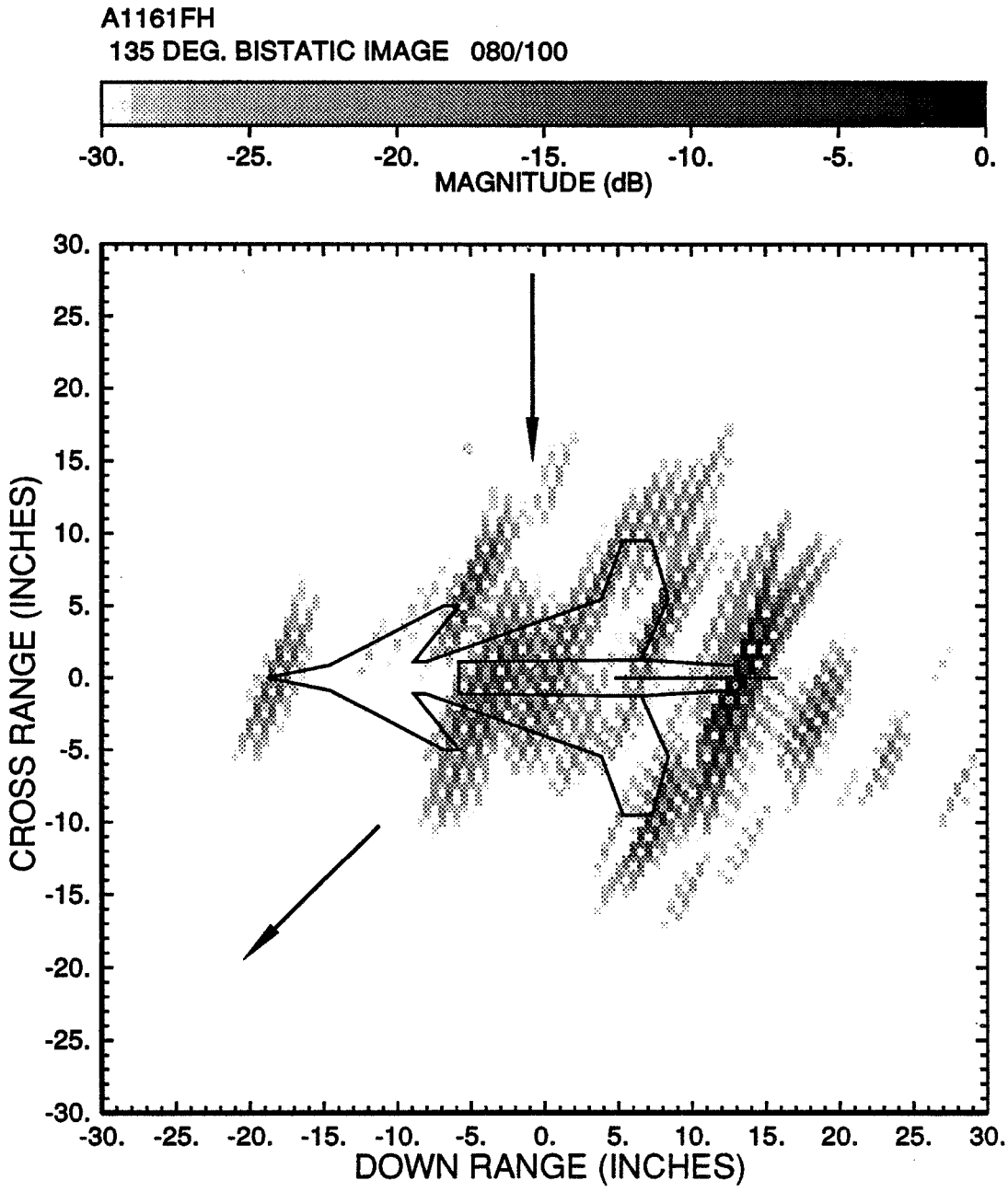

Figure 4.9: Bistatic ISAR image of the model aircraft. (135° bistatic angle, $\theta = 90° \pm 10°$).

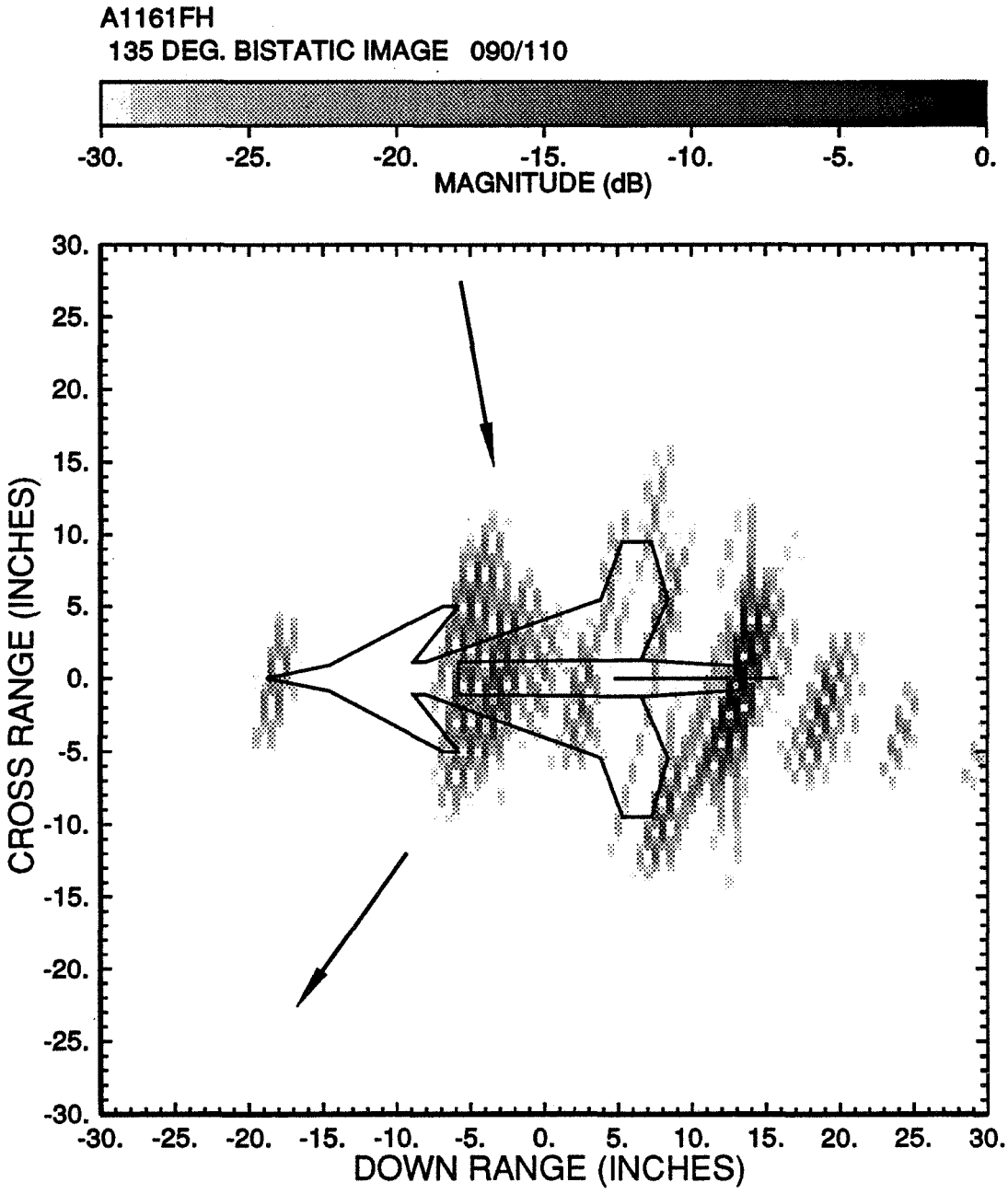

Figure 4.10: Bistatic ISAR image of the model aircraft. (135° bistatic angle, $\theta = 100° \pm 10°$).

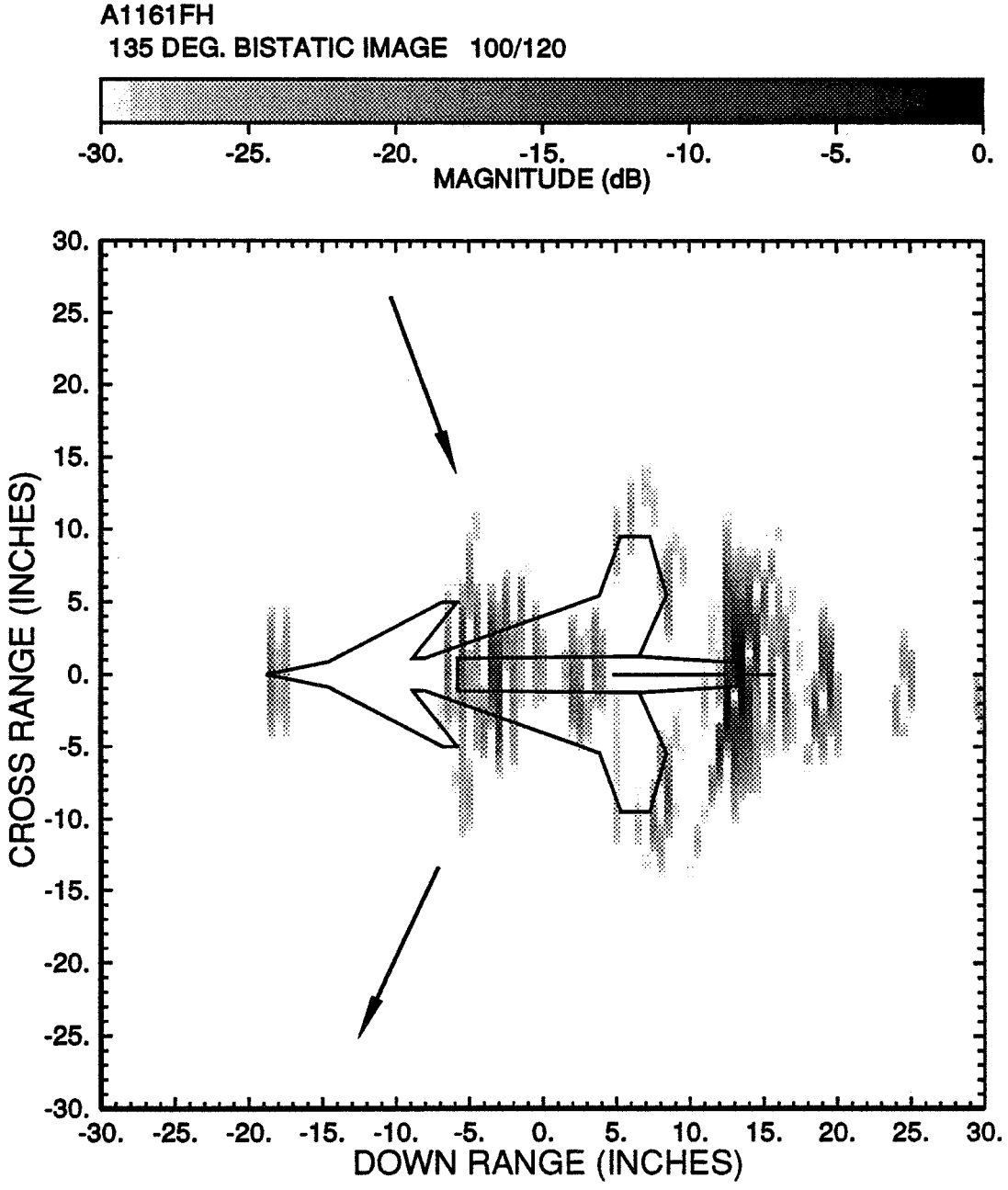

Figure 4.11: Bistatic ISAR image of the model aircraft. (135° bistatic angle, $\theta = 110° \pm 10°$).

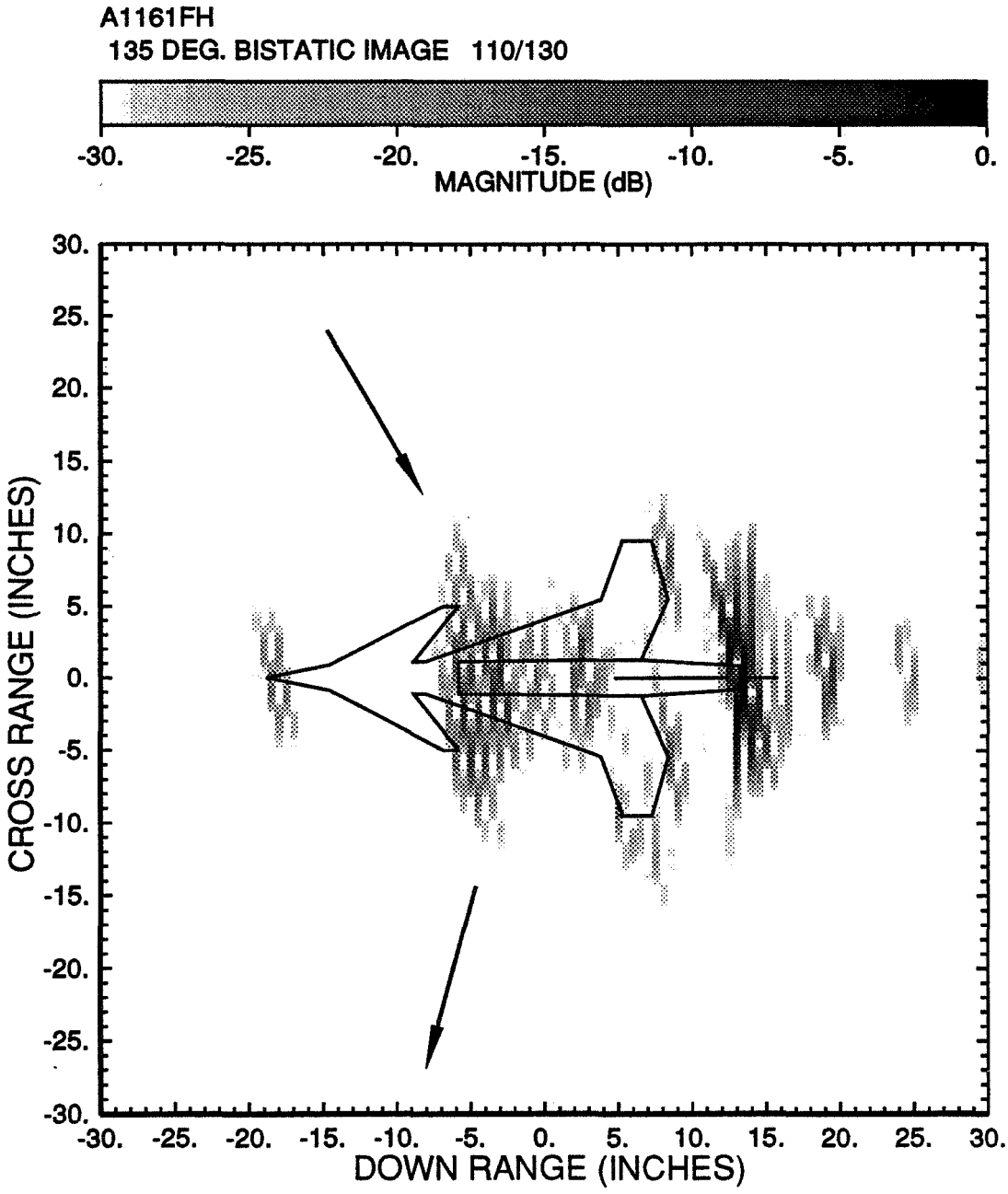

Figure 4.12: Bistatic ISAR image of the model aircraft. (135° bistatic angle, $\theta = 120° \pm 10°$).

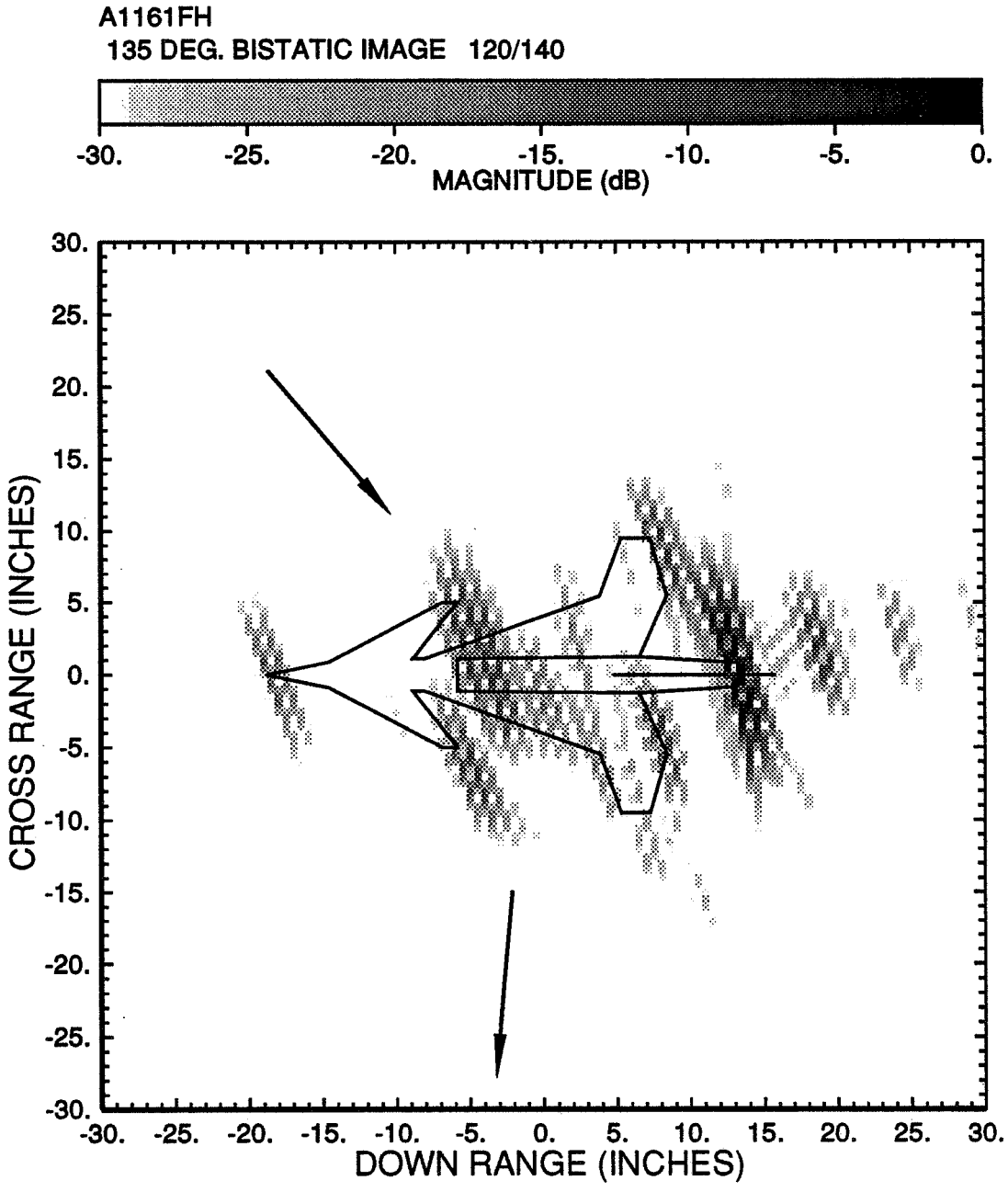

Figure 4.13: Bistatic ISAR image of the model aircraft. (135° bistatic angle, $\theta = 130° \pm 10°$).

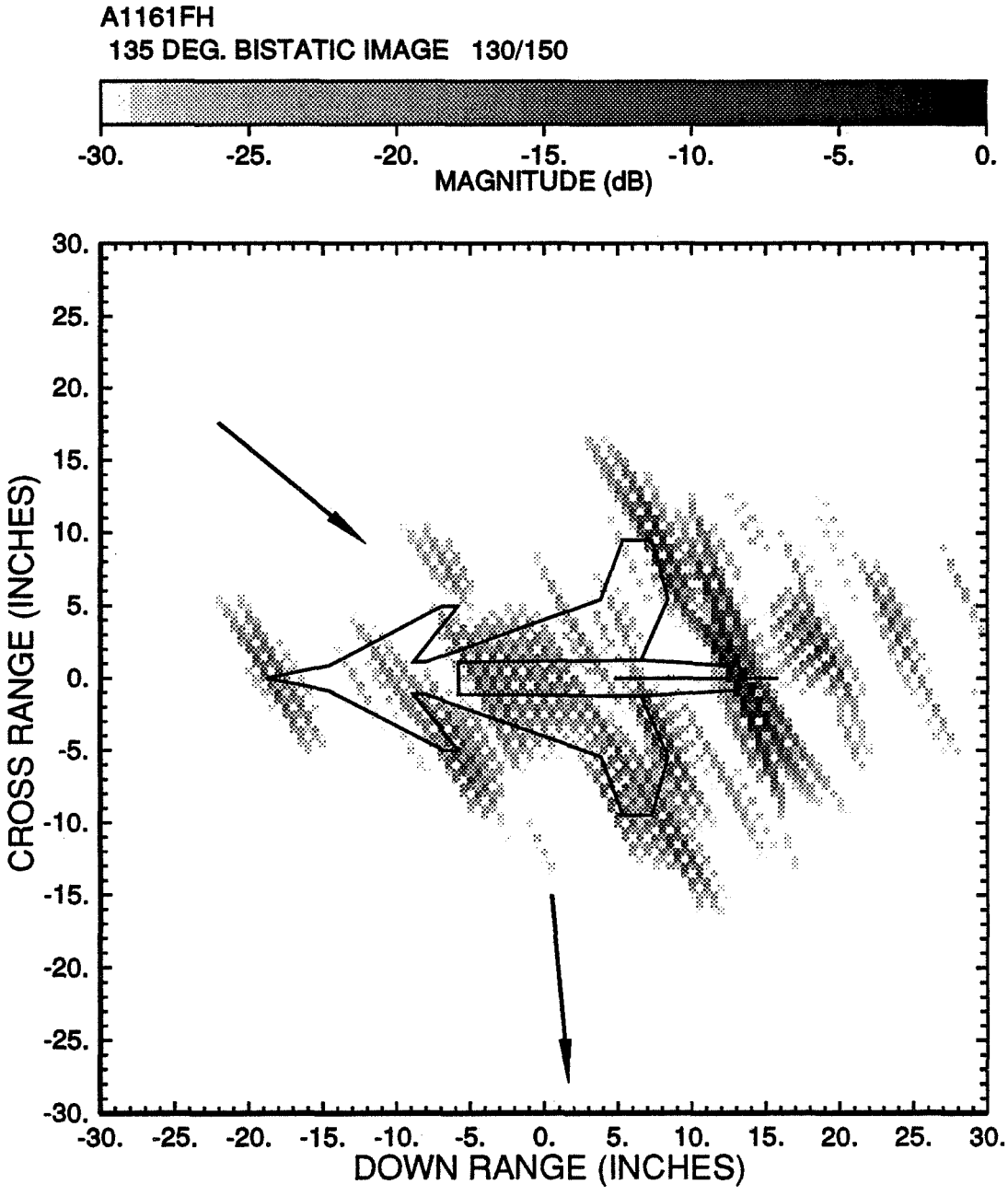

Figure 4.14: Bistatic ISAR image of the model aircraft. (135° bistatic angle, $\theta = 140° \pm 10°$).

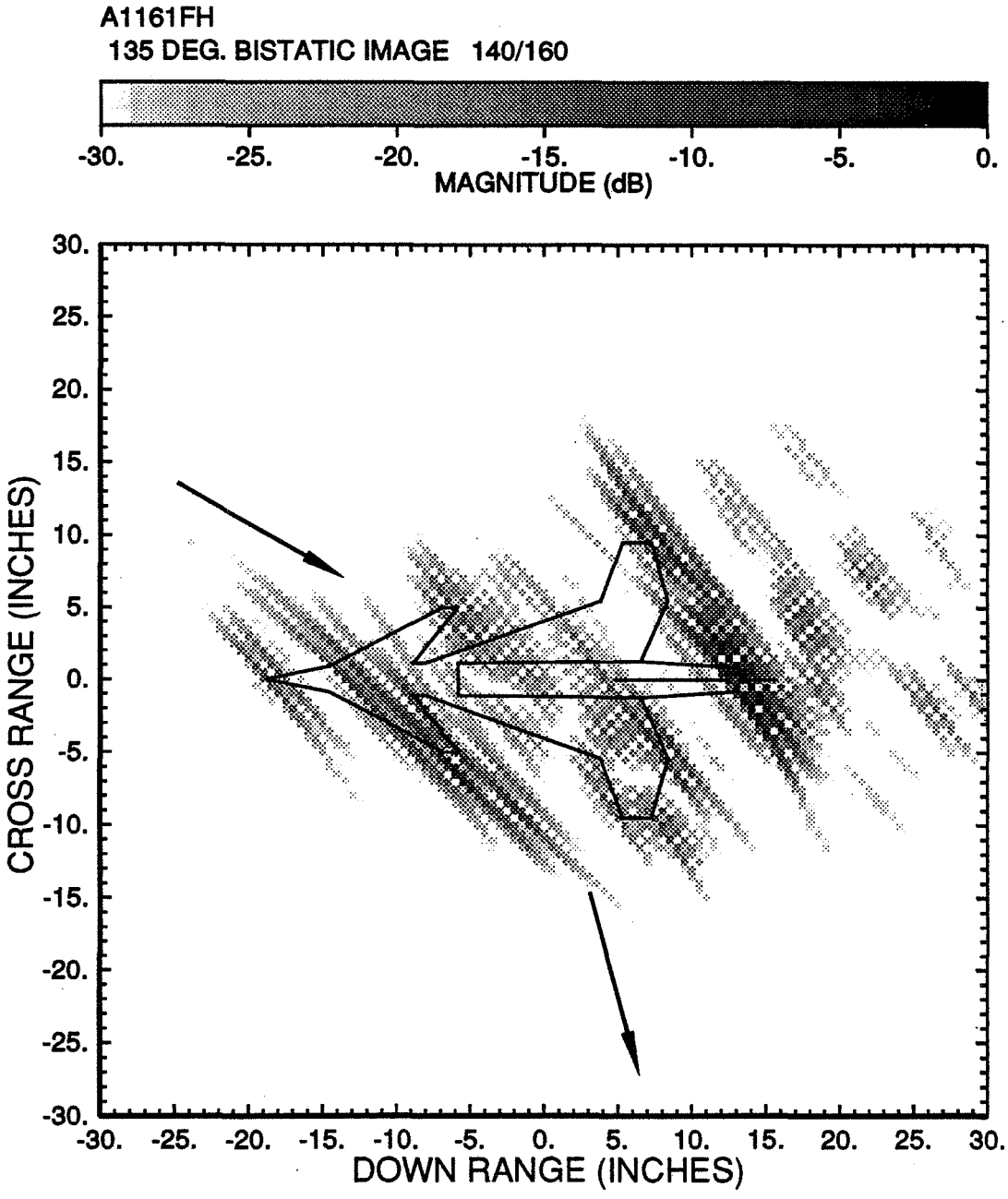

Figure 4.15: Bistatic ISAR image of the model aircraft. (135° bistatic angle, $\theta = 150° \pm 10°$).

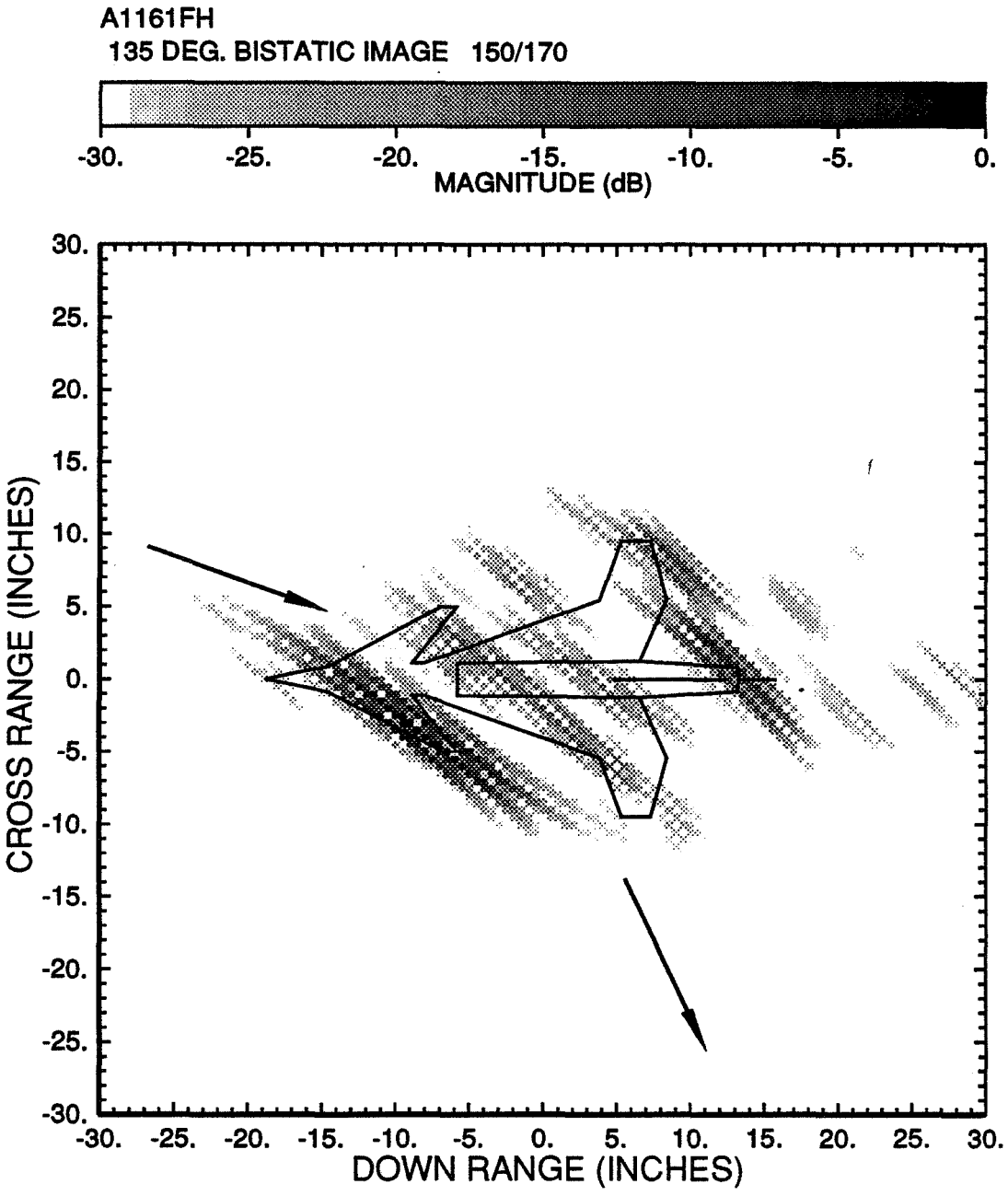

Figure 4.16: Bistatic ISAR image of the model aircraft. (135° bistatic angle, $\theta = 160° \pm 10°$).

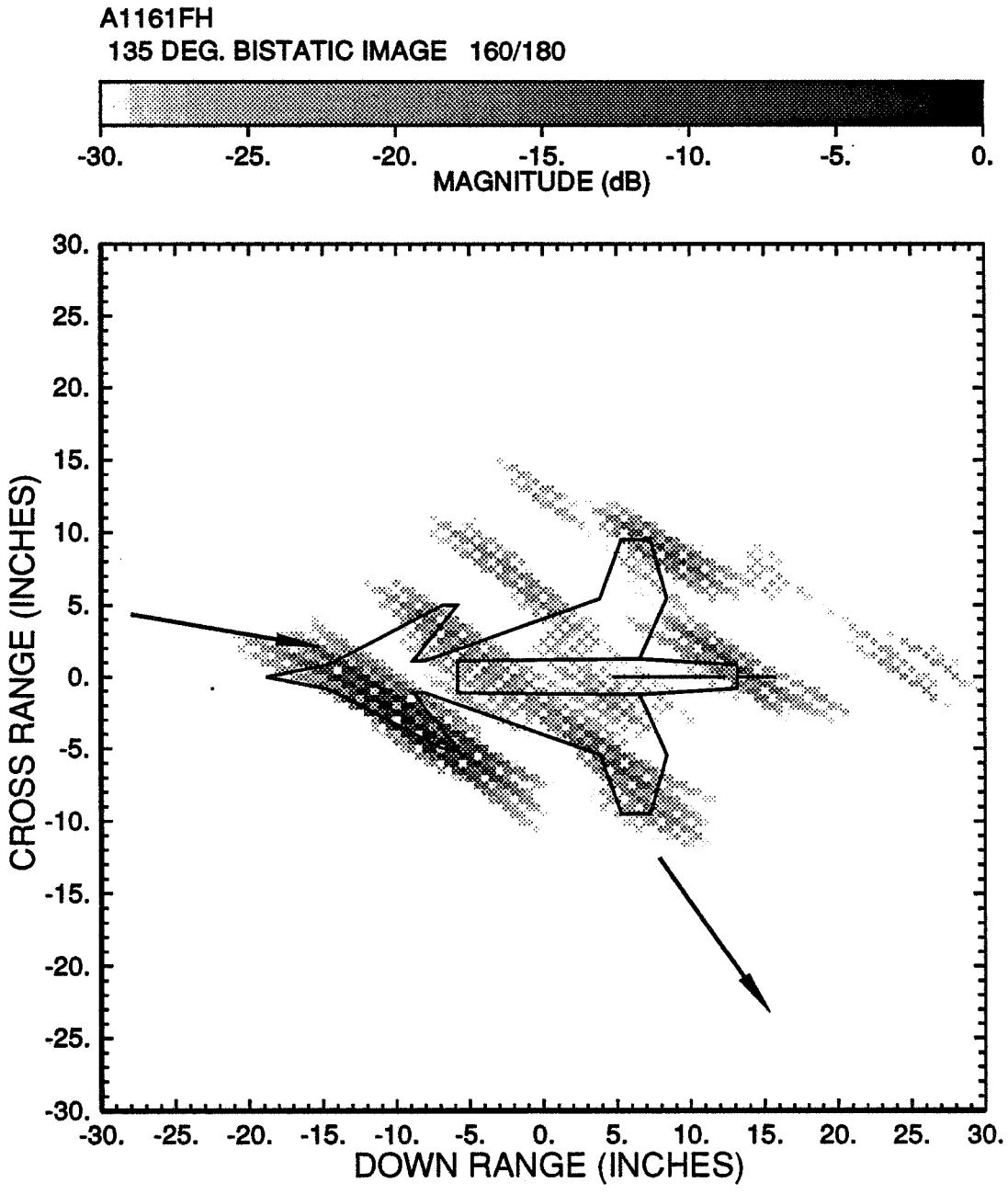

Figure 4.17: Bistatic ISAR image of the model aircraft. (135° bistatic angle, $\theta = 170° \pm 10°$).

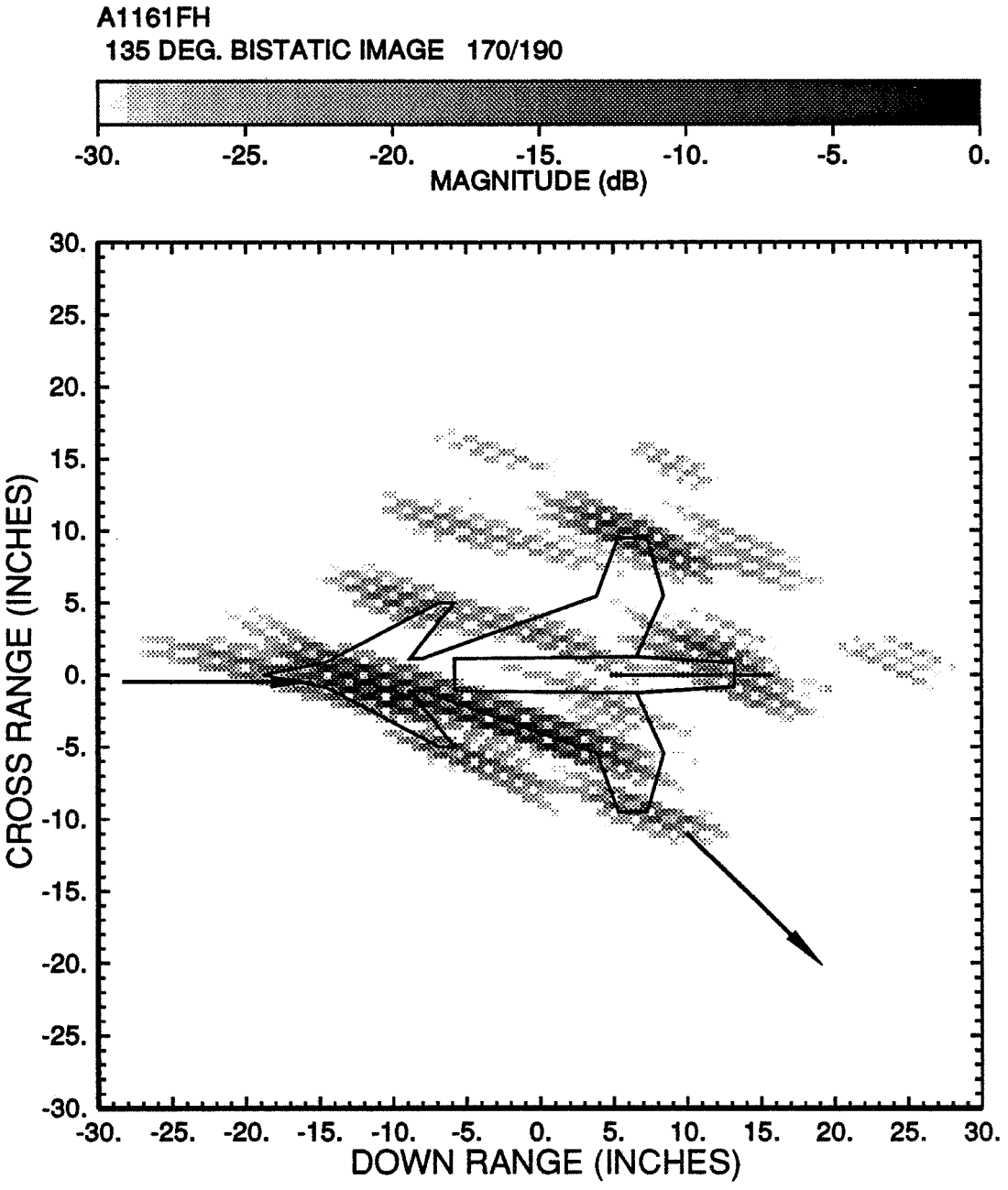

Figure 4.18: Bistatic ISAR image of the model aircraft. (135° bistatic angle, $\theta = 180° \pm 10°$).

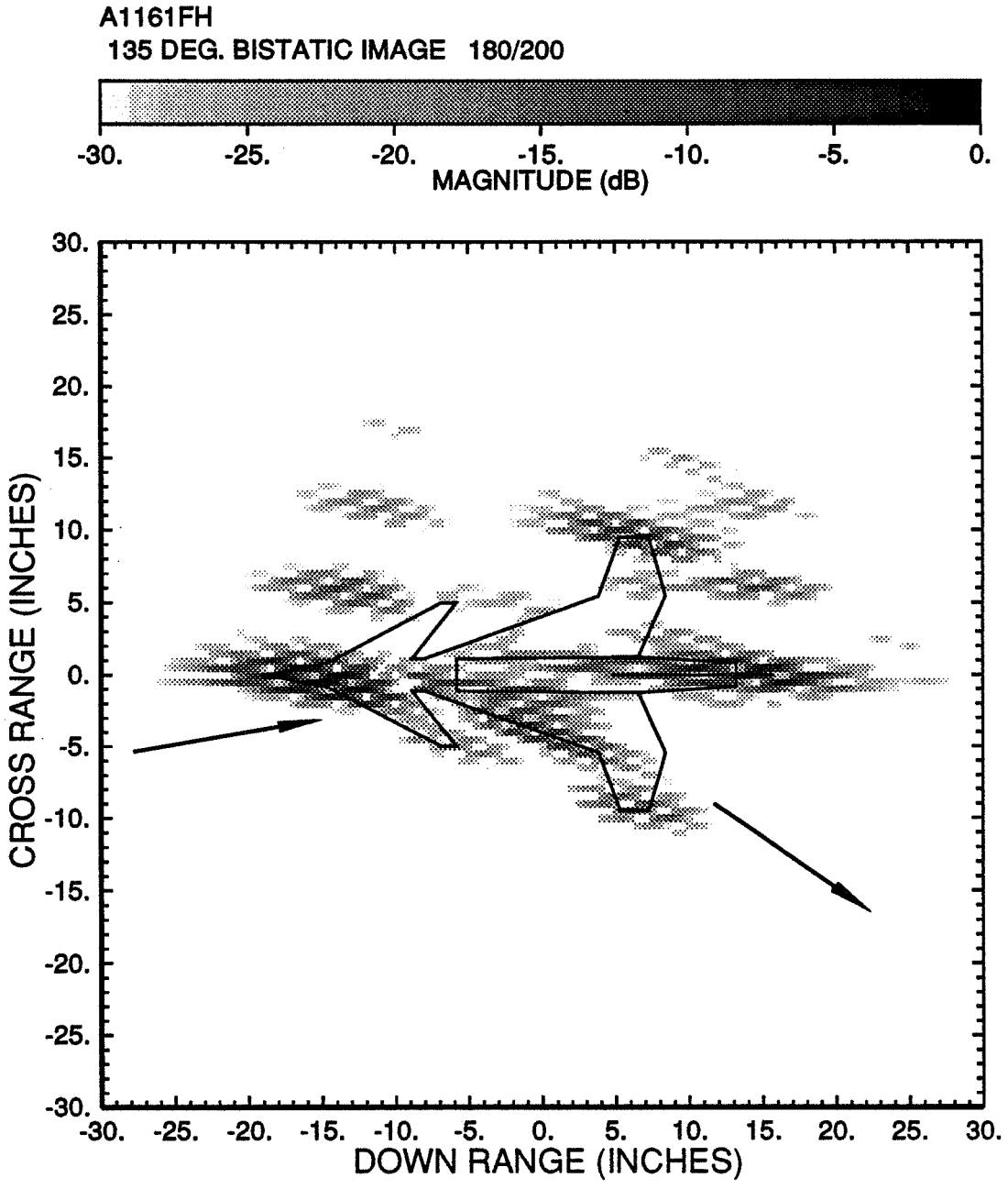

Figure 4.19: Bistatic ISAR image of the model aircraft. (135° bistatic angle, $\theta = 190° \pm 10°$).

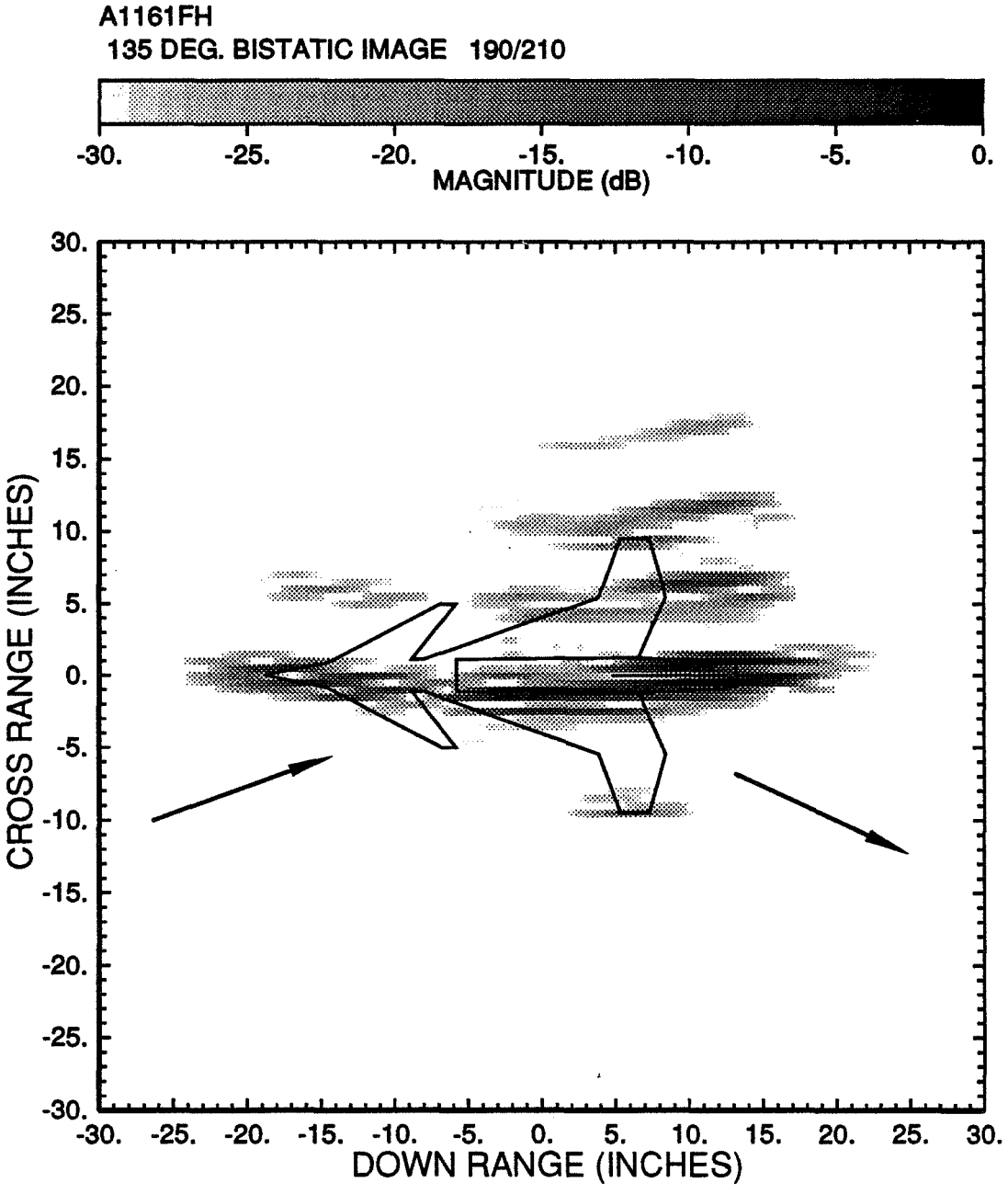

Figure 4.20: Bistatic ISAR image of the model aircraft. (135° bistatic angle, $\theta = 200° \pm 10°$).

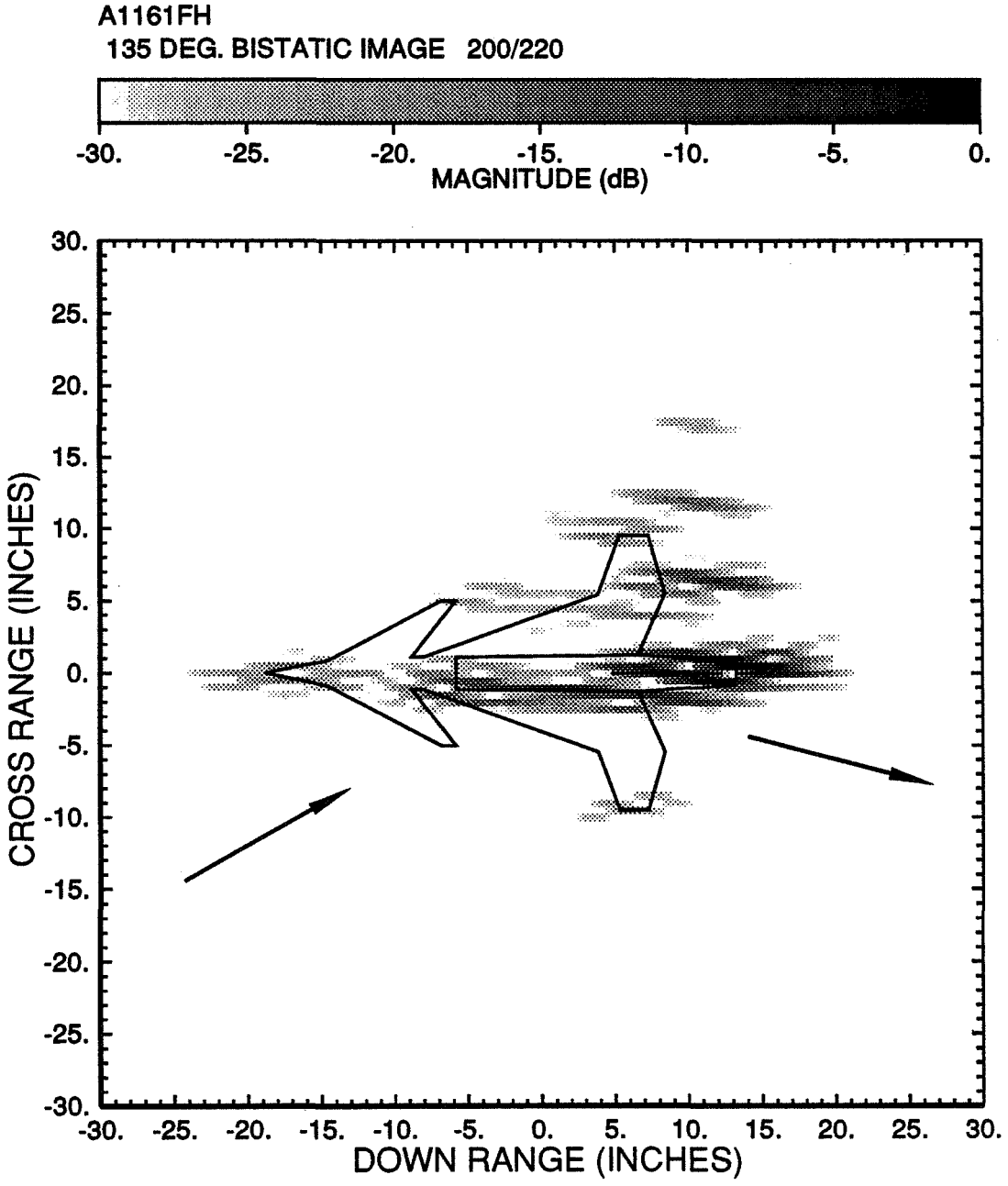

Figure 4.21: Bistatic ISAR image of the model aircraft. (135° bistatic angle, $\theta = 210° \pm 10°$).

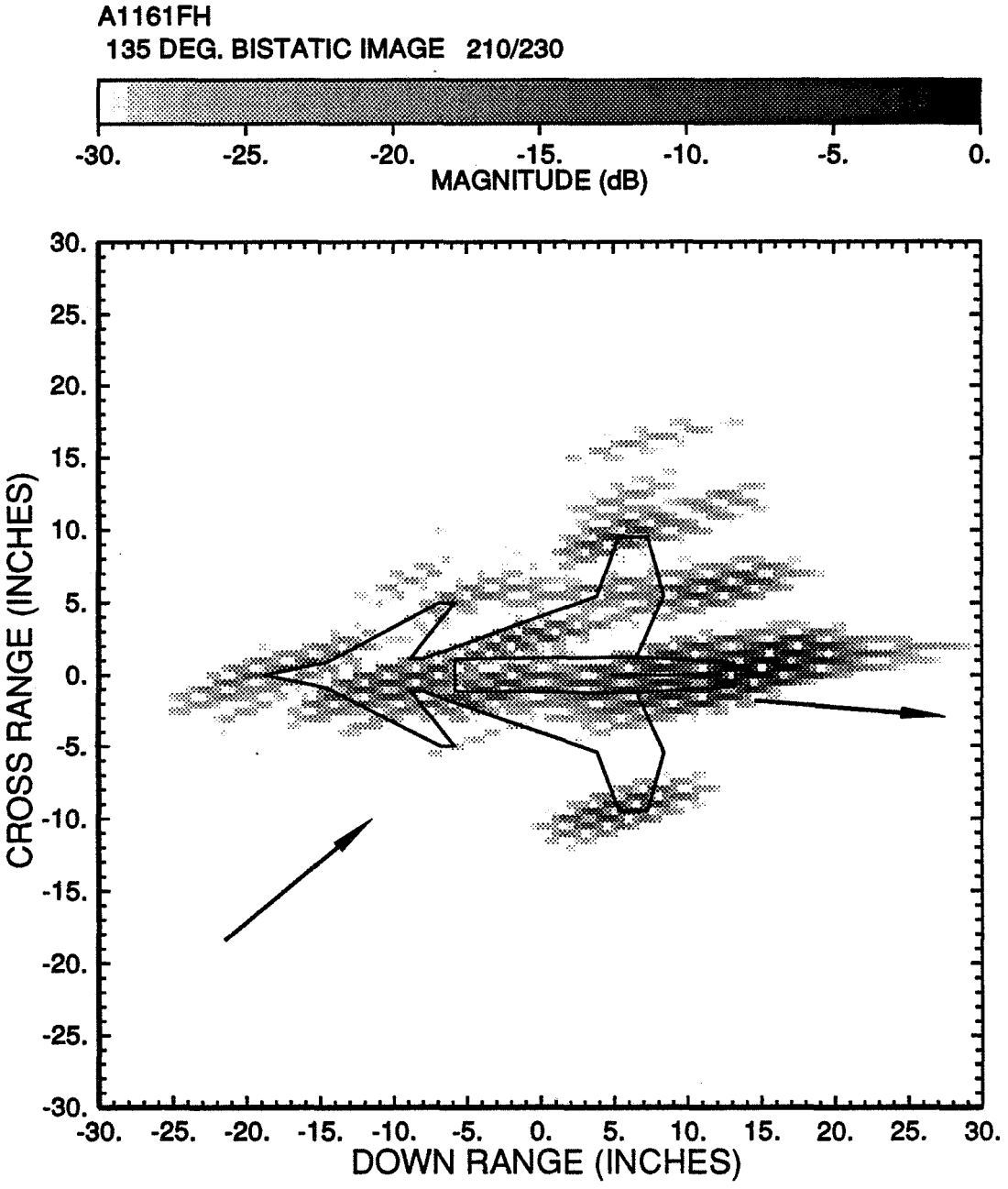

Figure 4.22: Bistatic ISAR image of the model aircraft. (135° bistatic angle, $\theta = 220° \pm 10°$).

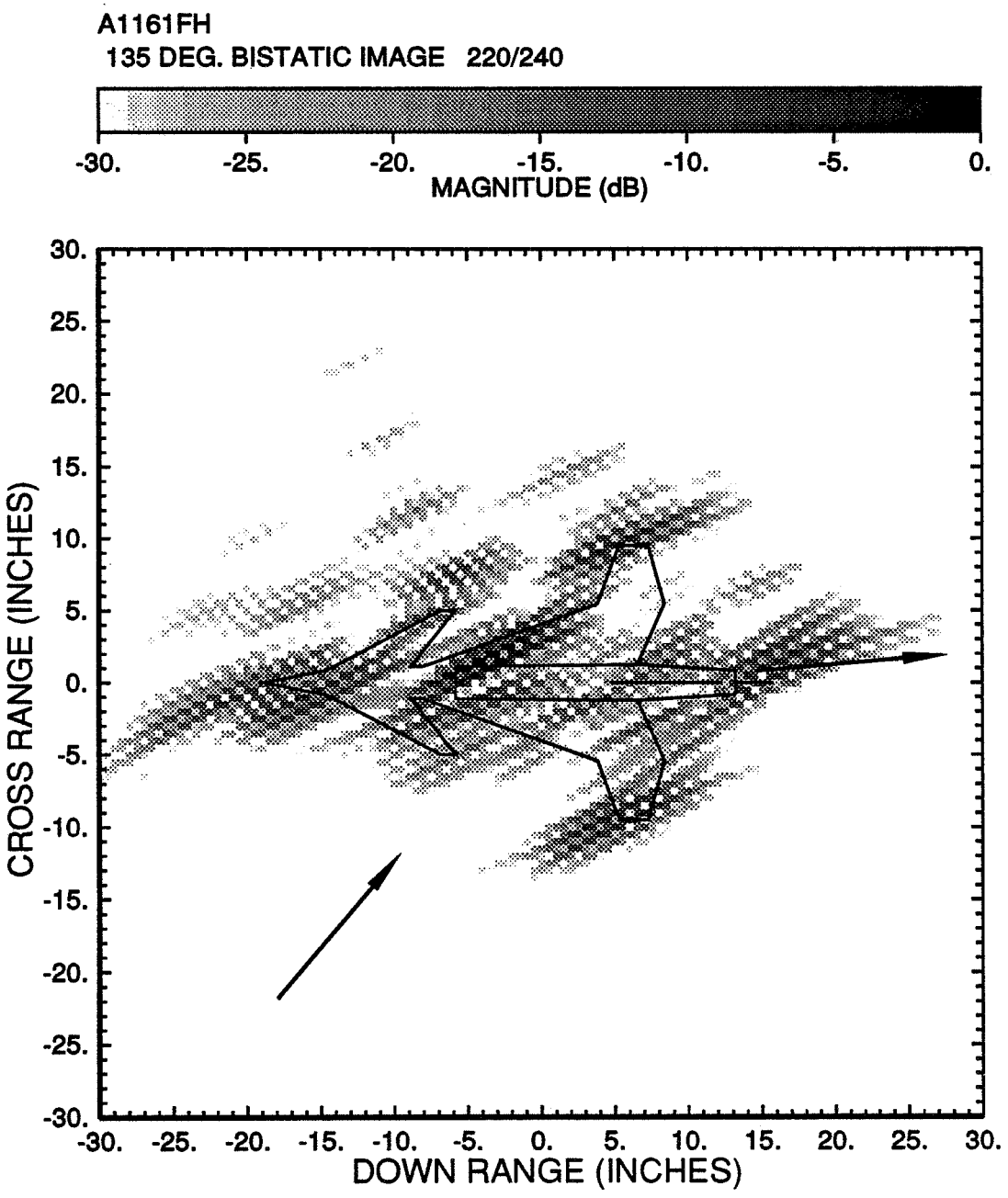

Figure 4.23: Bistatic ISAR image of the model aircraft. (135° bistatic angle, $\theta = 230° \pm 10°$).

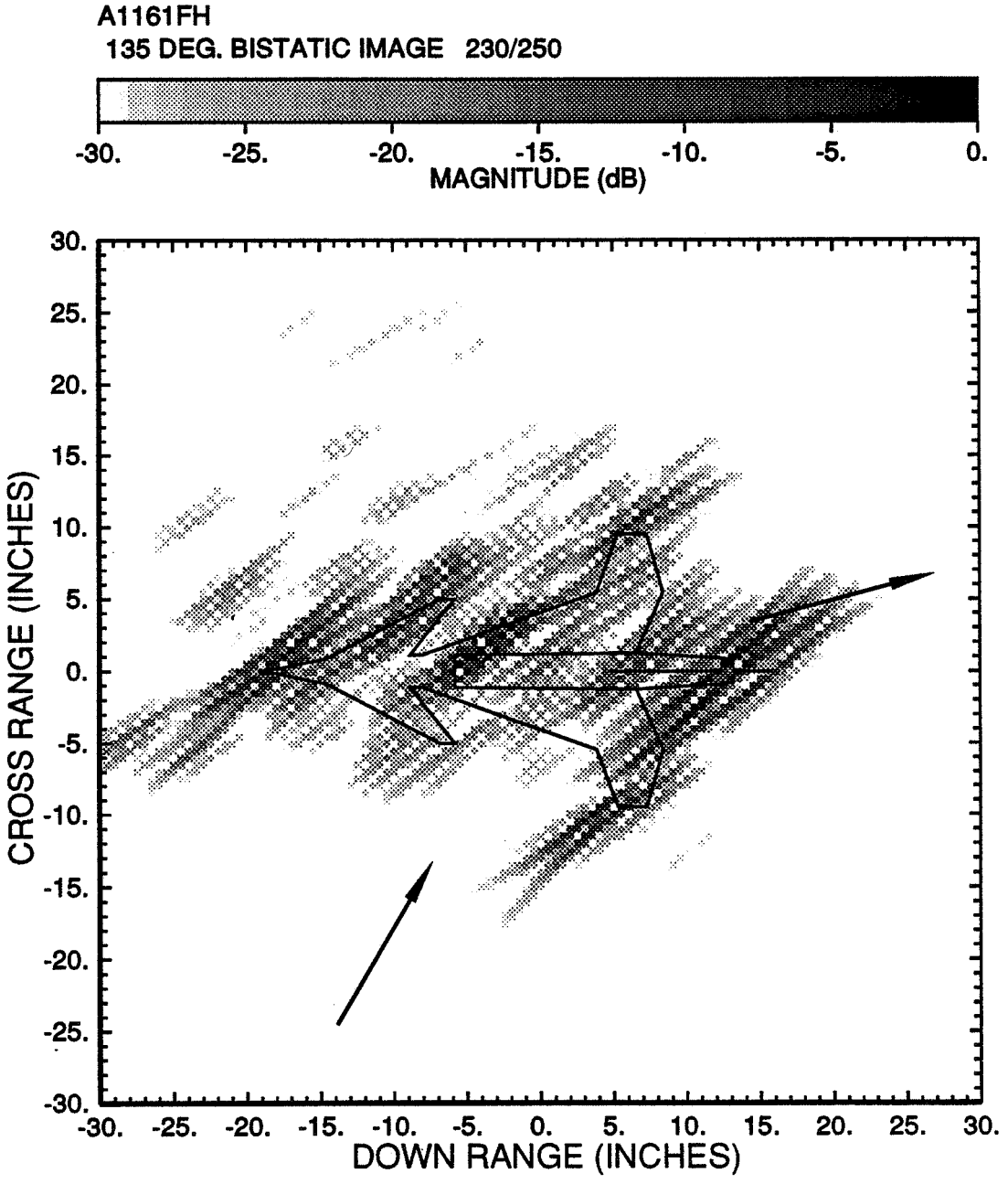

Figure 4.24: Bistatic ISAR image of the model aircraft. (135° bistatic angle, $\theta = 240° \pm 10°$).

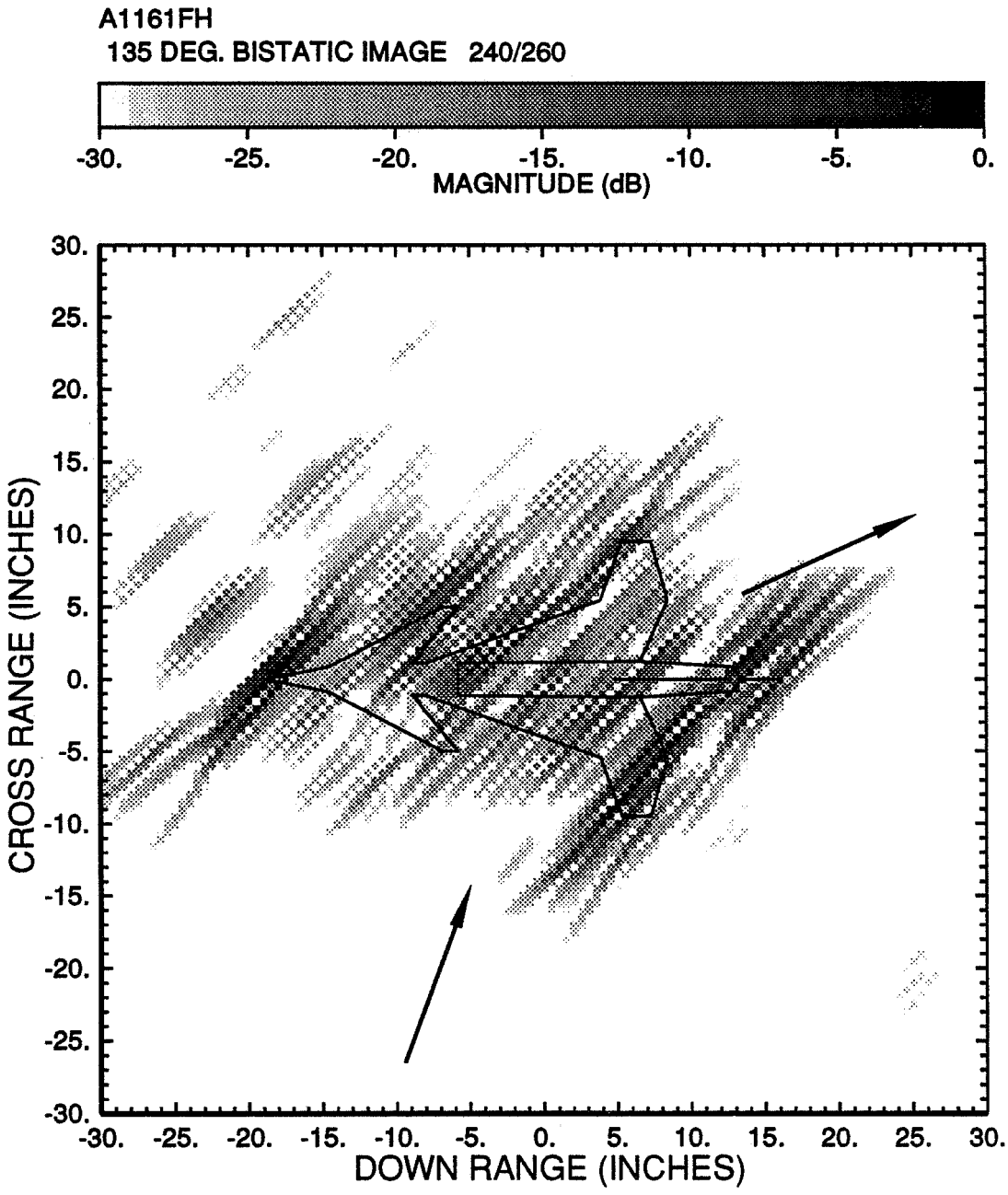

Figure 4.25: Bistatic ISAR image of the model aircraft. (135° bistatic angle, $\theta = 250° \pm 10°$).

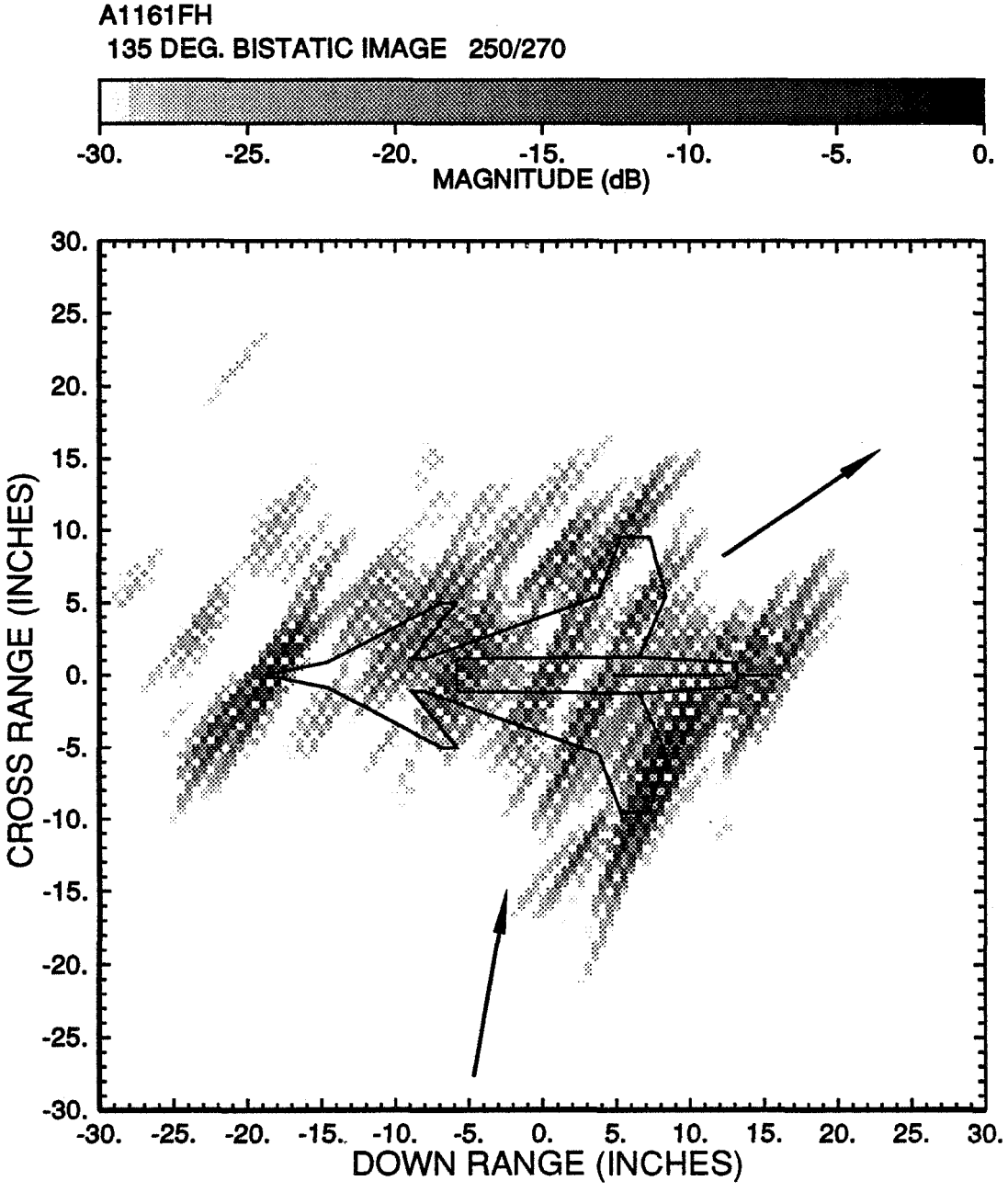

Figure 4.26: Bistatic ISAR image of the model aircraft. (135° bistatic angle, $\theta = 260° \pm 10°$).

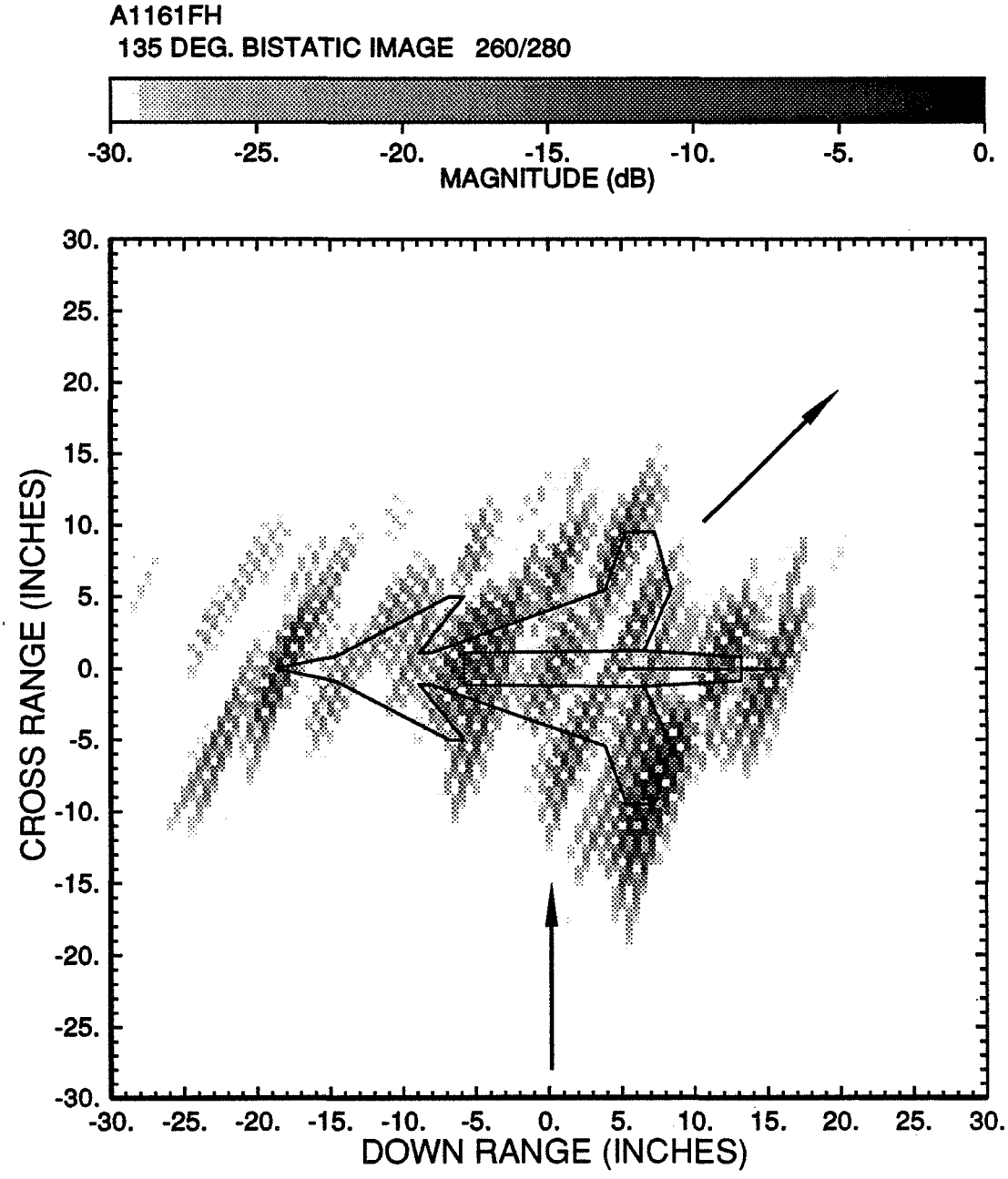

Figure 4.27: Bistatic ISAR image of the model aircraft. (135° bistatic angle, $\theta = 270° \pm 10°$).

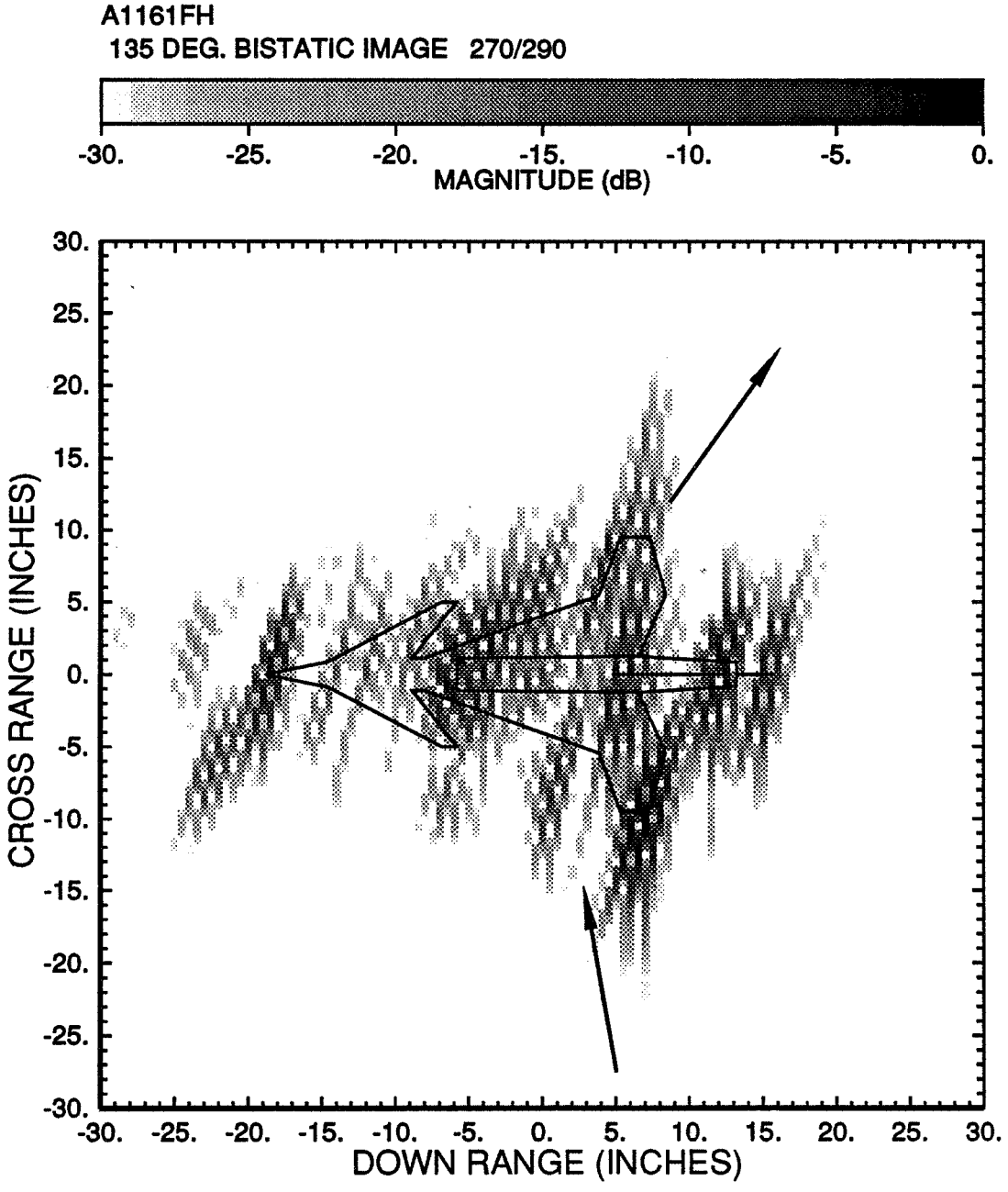

Figure 4.28: Bistatic ISAR image of the model aircraft. (135° bistatic angle, $\theta = 280° \pm 10°$).

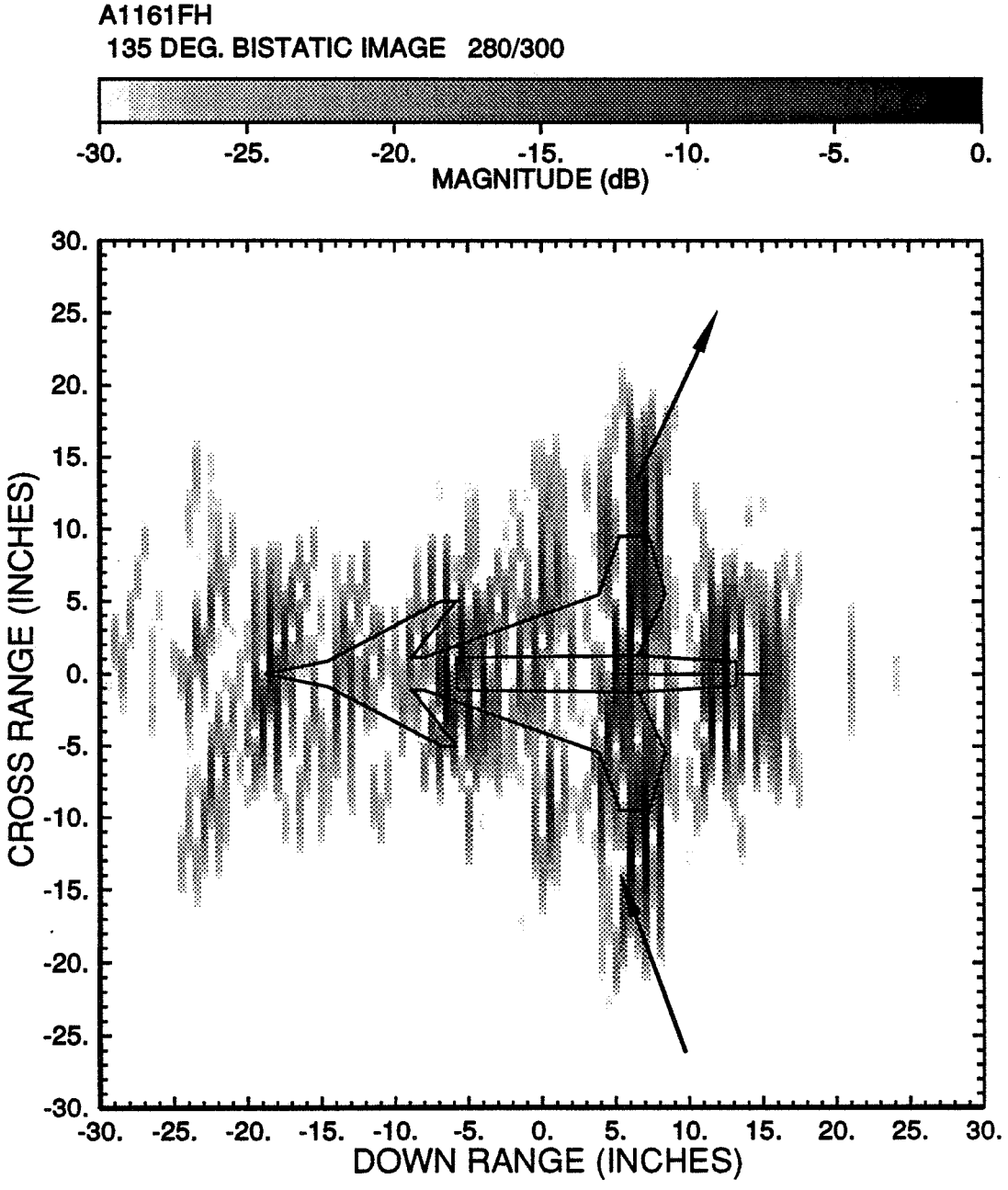

Figure 4.29: Bistatic ISAR image of the model aircraft. (135° bistatic angle, $\theta = 290° \pm 10°$).

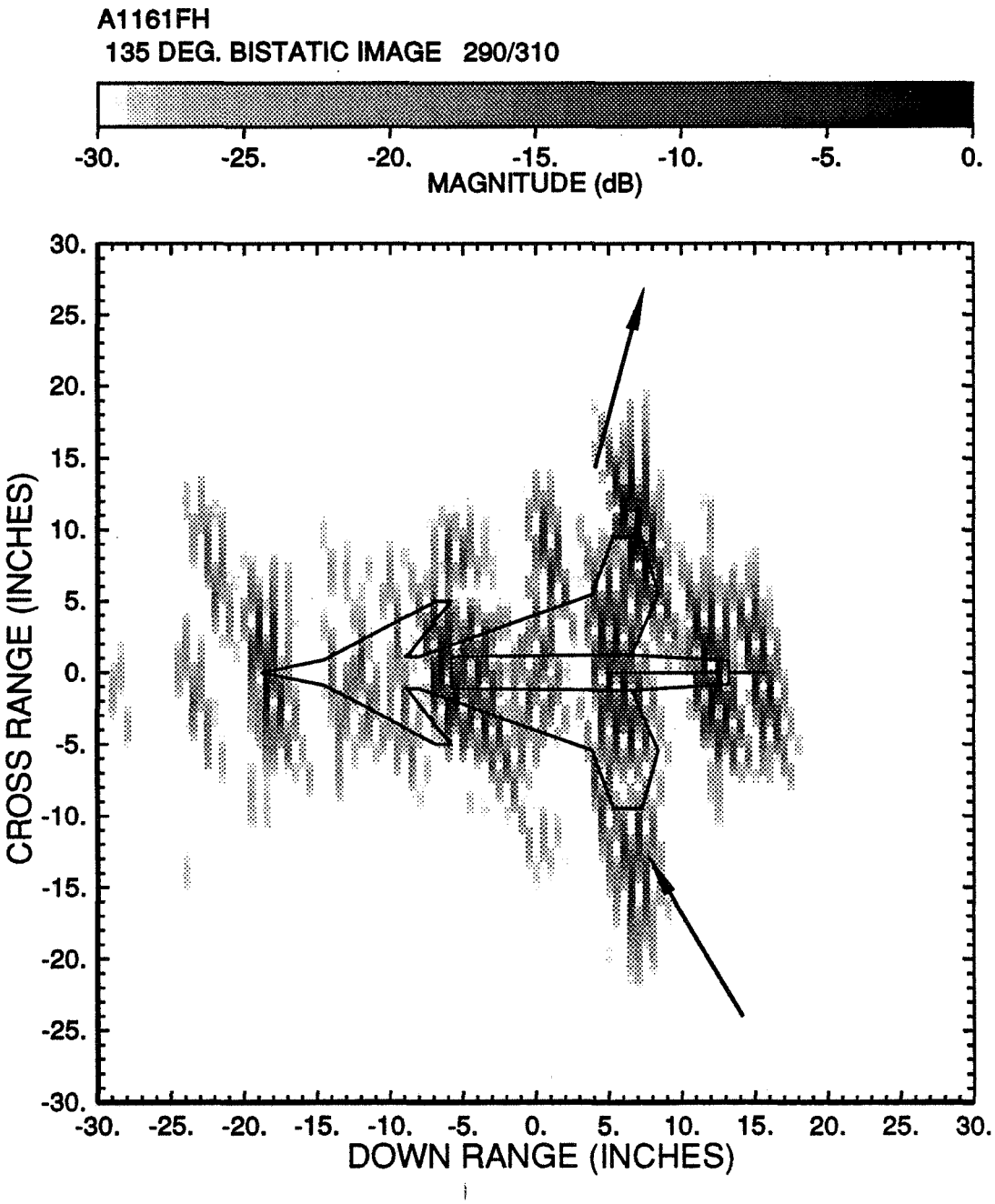

Figure 4.30: Bistatic ISAR image of the model aircraft. (135° bistatic angle, $\theta = 300° \pm 10°$).

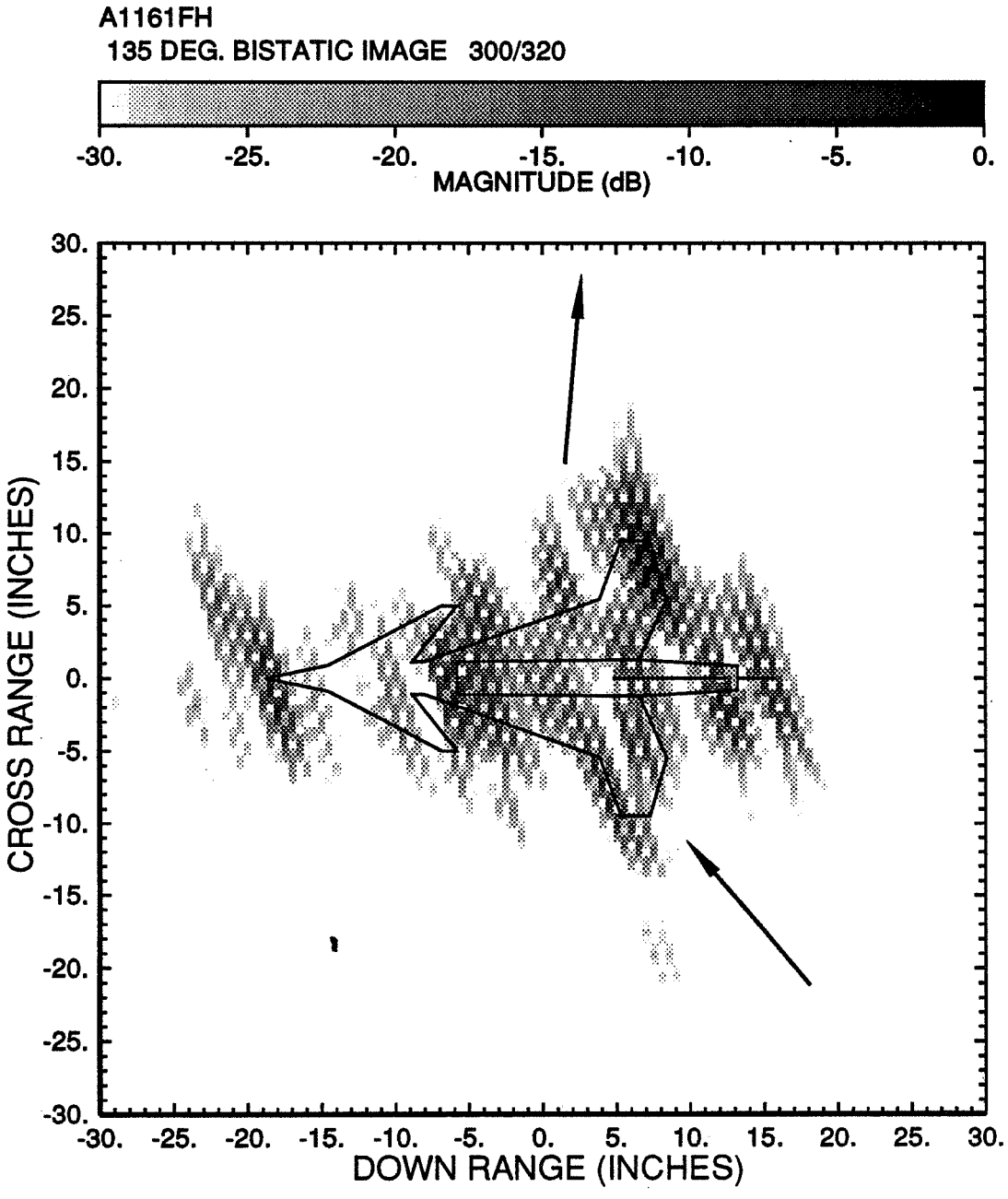

Figure 4.31: Bistatic ISAR image of the model aircraft. (135° bistatic angle, $\theta = 310° \pm 10°$).

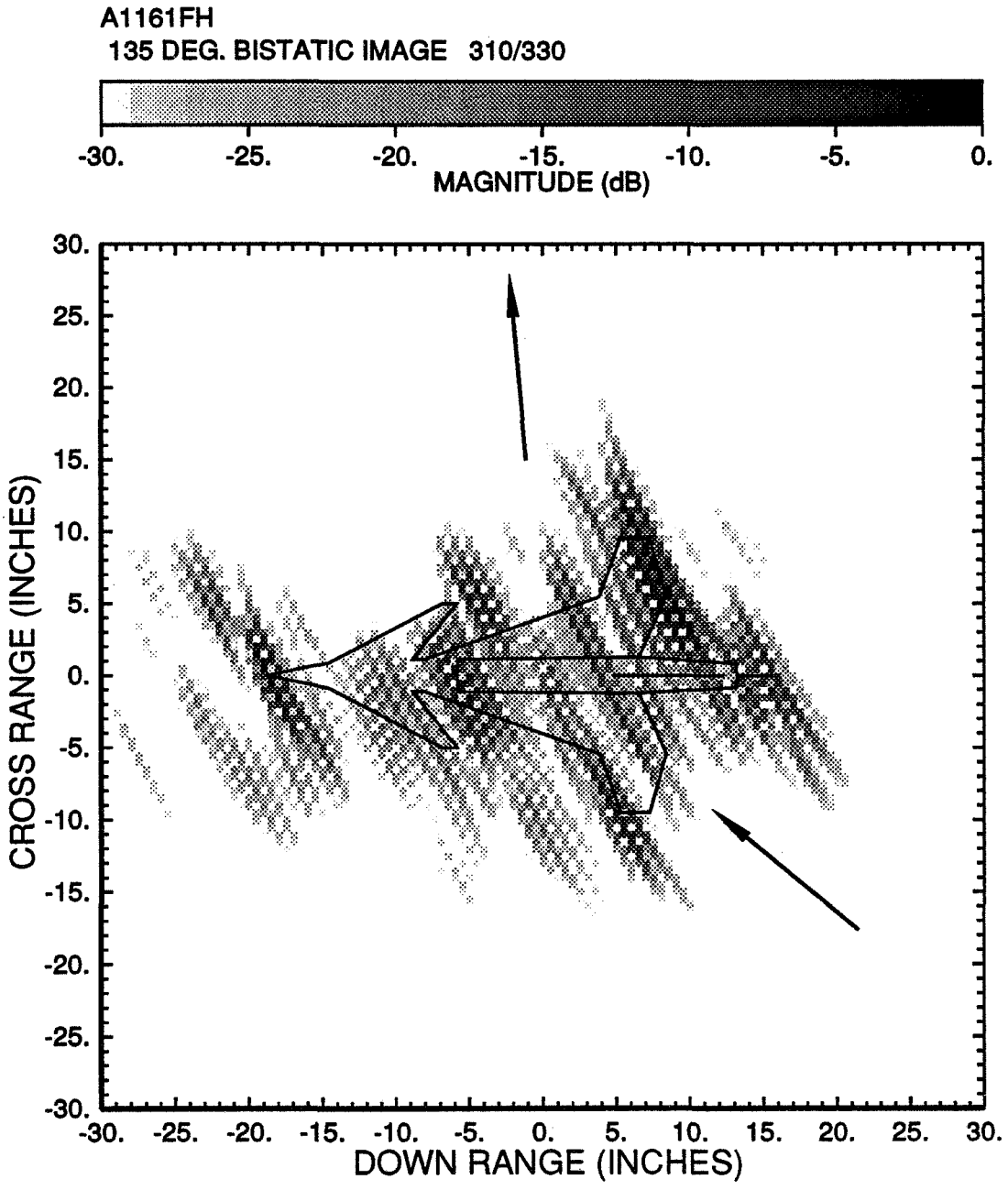

Figure 4.32: Bistatic ISAR image of the model aircraft. (135° bistatic angle, $\theta = 320° \pm 10°$).

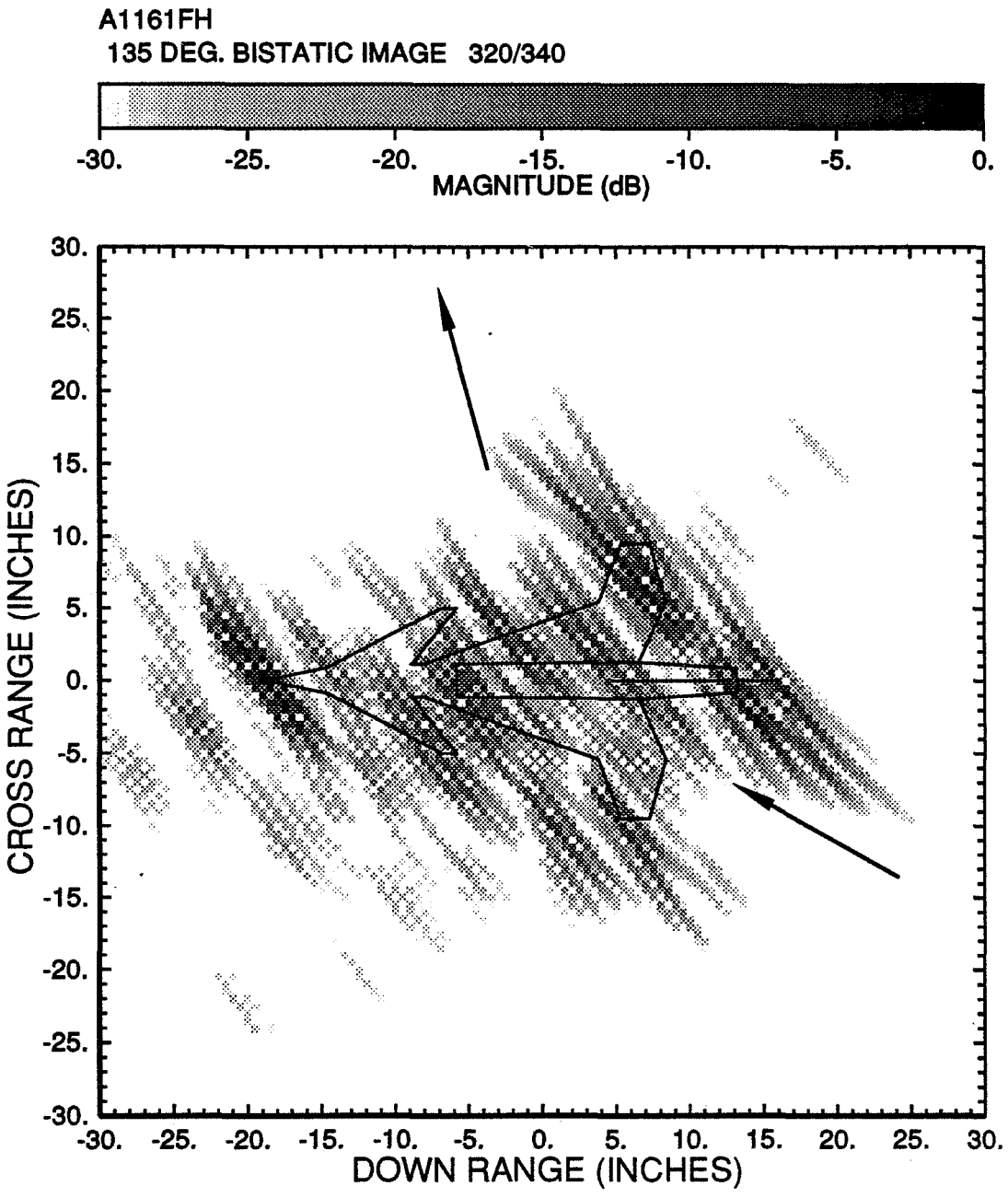

Figure 4.33: Bistatic ISAR image of the model aircraft. (135° bistatic angle, $\theta = 330° \pm 10°$).

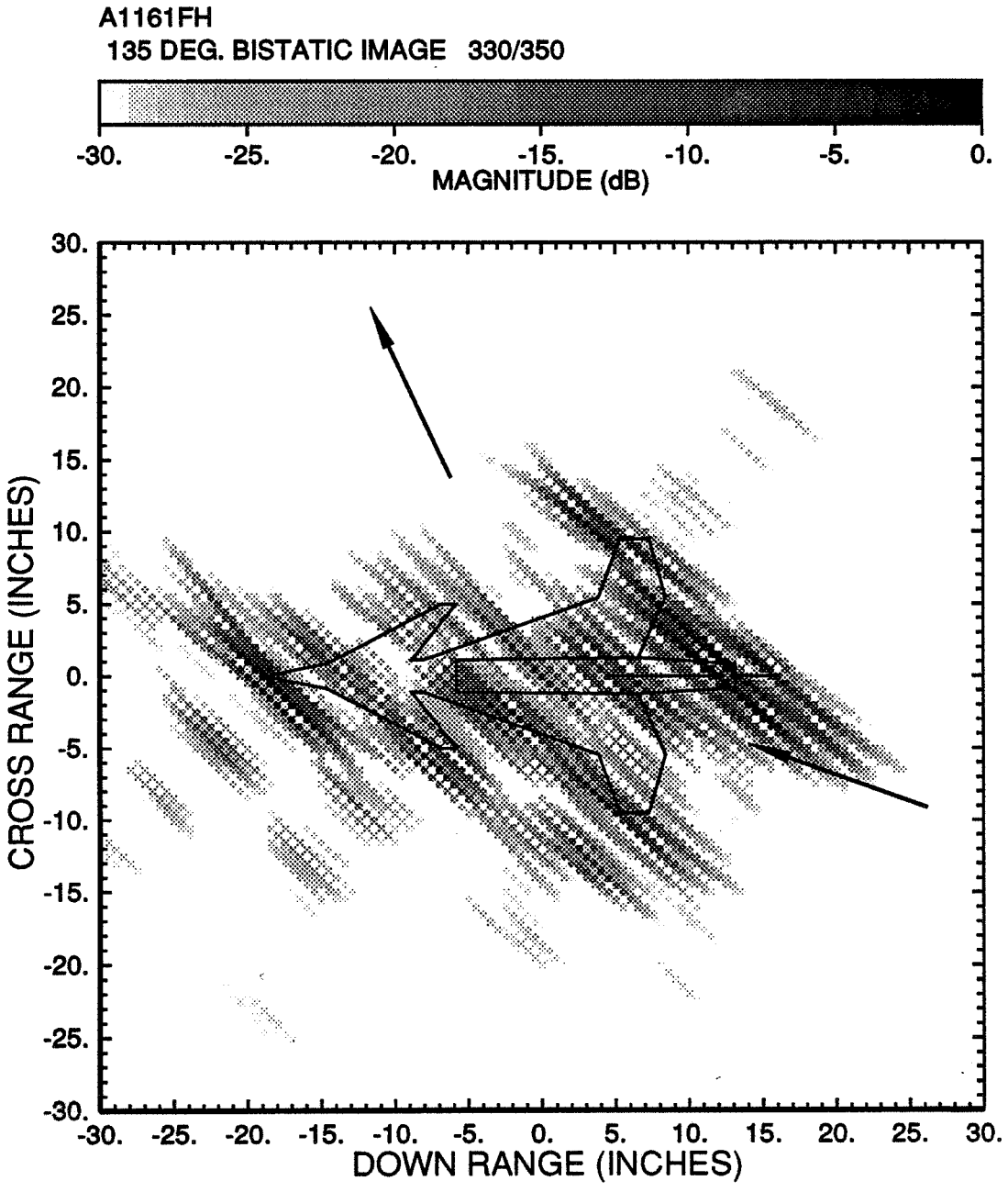

Figure 4.34: Bistatic ISAR image of the model aircraft. (135° bistatic angle, $\theta = 340° \pm 10°$).

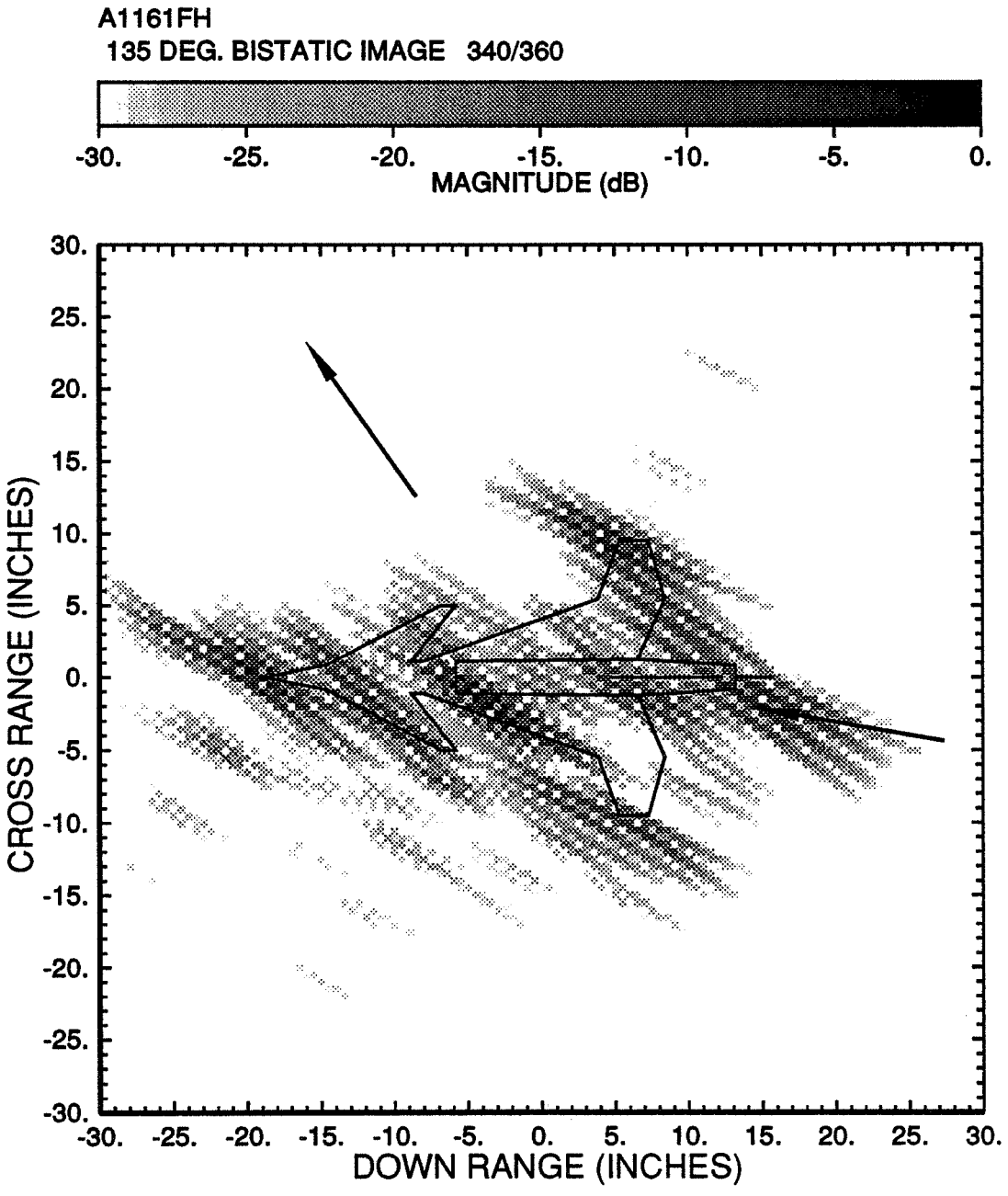

Figure 4.35: Bistatic ISAR image of the model aircraft. (135° bistatic angle, $\theta = 350° \pm 10°$).

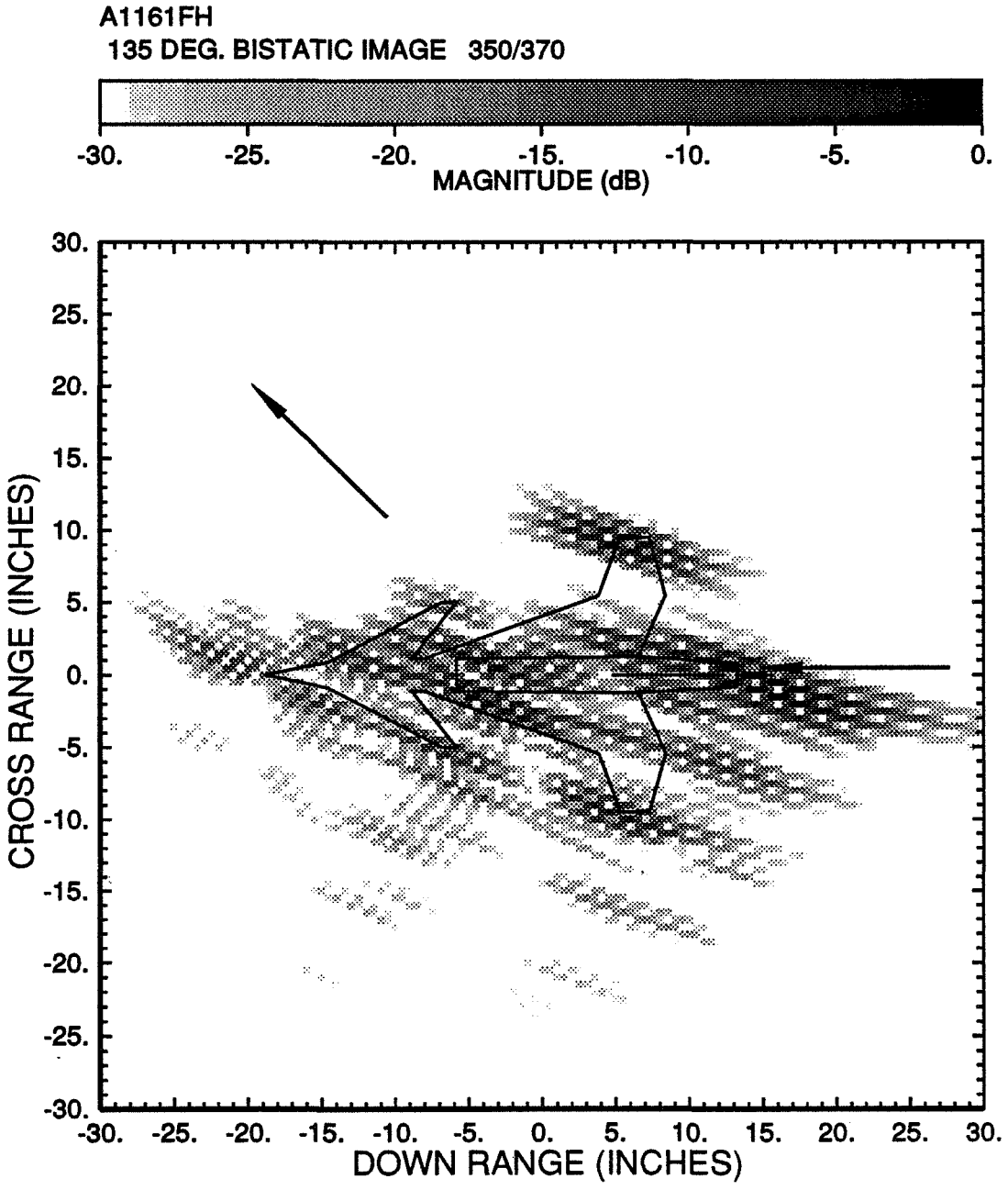

Figure 4.36: Bistatic ISAR image of the model aircraft. (135° bistatic angle, $\theta = 360° \pm 10°$).

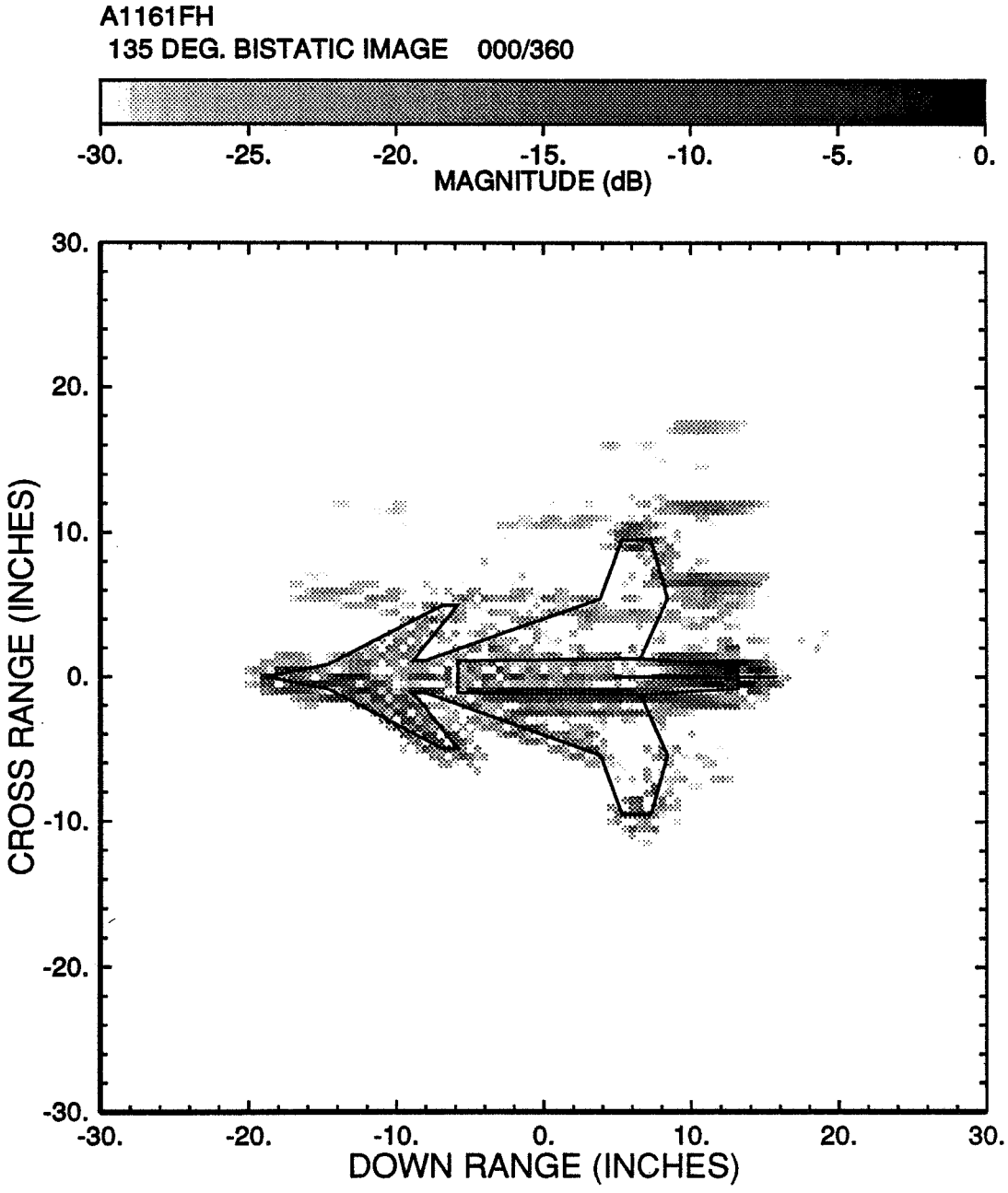

Figure 4.37: Bistatic ISAR image of the model aircraft. (complete 360°).

Chapter 5

Summary

Inverse Synthetic Aperture Radar (ISAR) images for a 32″ long and 19″ wide model aircraft have been documented in this report. Backscattered images and bistatic scattered field images for bistatic angles of 90° and 135° have been presented. Both the backscattered and bistatic scattered fields were measured in the OSU-ESL compact range facility.

For the bistatic measurement in a compact range, the transmitting and receiving antennas can be two compact ranges or one compact range and one horn antenna. Furthermore, the compact range can be either focussed or defocussed and the horn antenna can be either in the near field or in the far field of the target.

The ISAR images were obtained by using the time domain/angular domain data of the scattered fields. This approach can be used for both the backscattered and bistatic scattered cases independent of whether the antenna is in the near or far field of the target. In addition, it is very efficient in computation and real time image can be performed. As a result, it is a very useful diagnostic tool.

Bibliography

[1] D.L. Mensa and K. Vaccaro, "Interpretation of two-dimensional RCS images," in *Proceedings of Antenna Measurement Association Techniques,* September, 1988.

[2] T.H. Lee and W.D. Burnside, "Image processing of bistatic scattered fields obtained in a compact range," in *Proceedings of Antenna Measurement Association Techniques,* October 1989.

[3] T.H. Lee and W.D. Burnside, "A focused image processing procedure using near zone scattered fields obtained in a compact range," *IEEE Trans. Antennas Propagat.,* Vol. 37, No. 12, pp. 1598-1603, December 1989.

[4] G.M. Dural, "Polarimetric ISAR Imaging to Identify Basic Scattering Mechanisms Using Transient Signatures," Technical Report 312884-9, The Ohio State University ElectroScience Laboratory, December, 1988.

[5] W.D. Burnside, T.H. Lee, R. Rojas, R.J. Marhefka and D. Bensman, "Target signature modeling and bistatic scattering measurement studies," Technical Report 721432-2, 721446-2,721447-2, and 721711-3, Sept. 1988-Aug. 1989, The Ohio State University ElectroScience Laboratory, Department of Electrical Engineering, February 1989. Prepared under Grant No. NAG2-542 for National Aeronautics and Space Administration Ames Research Center, Moffett Field, California.

[6] D.L. Mensa, High Resolution Radar Cross-Section Imaging, Artech House, Inc., Norwood, MA, 1991.

722780-3, "Bistatic Image Processing for a 32″ × 19″ Model Aircraft using Scattered Fields Obtained ...", Lee and Burnside, February 1992